



THE HONG KONG  
POLYTECHNIC UNIVERSITY

香港理工大學

Pao Yue-kong Library  
包玉剛圖書館

---

## Copyright Undertaking

This thesis is protected by copyright, with all rights reserved.

**By reading and using the thesis, the reader understands and agrees to the following terms:**

1. The reader will abide by the rules and legal ordinances governing copyright regarding the use of the thesis.
2. The reader will use the thesis for the purpose of research or private study only and not for distribution or further reproduction or any other purpose.
3. The reader agrees to indemnify and hold the University harmless from and against any loss, damage, cost, liability or expenses arising from copyright infringement or unauthorized usage.

### IMPORTANT

If you have reasons to believe that any materials in this thesis are deemed not suitable to be distributed in this form, or a copyright owner having difficulty with the material being included in our database, please contact [lbsys@polyu.edu.hk](mailto:lbsys@polyu.edu.hk) providing details. The Library will look into your claim and consider taking remedial action upon receipt of the written requests.

Pao Yue-kong Library, The Hong Kong Polytechnic University, Hung Hom, Kowloon, Hong Kong

<http://www.lib.polyu.edu.hk>

**LANTHANIDE NEAR-INFRARED  
LUMINESCENCE IN LAYERED  
SEMICONDUCTOR NANOSHEET  
HOSTS**

**LYU YONGXIN**

**MPhil**

**The Hong Kong Polytechnic University  
2020**

**The Hong Kong Polytechnic University**

**Department of Applied Physics**

**Lanthanide Near-Infrared Luminescence  
in Layered Semiconductor Nanosheet Hosts**

**LYU Yongxin**

A thesis submitted in partial fulfillment of the requirements for the  
degree of Master of Philosophy

**August 2019**

# **CERTIFICATE OF ORIGINALITY**

I hereby declare that this thesis is my own work and that, to the best of my knowledge and belief, it reproduces no material previously published or written, nor material that has been accepted for the award of any other degree or diploma, except where due acknowledgement has been made in the text.

\_\_\_\_\_  
(Signed)

LYU Yongxin \_\_\_\_\_(Name of student)

## Abstract

Two-dimensional (2D) transition metal dichalcogenides (TMDs) have been investigated extensively due to their superior properties for constructing next generation opto-electric devices. However, the intrinsic photoluminescence emission is limited by their narrow bandgap, ranging from visible to the edge of near infrared. To further tune the intrinsic properties and enhance device performance of TMDs, several approaches have been adopted such as doping or alloying. Among all the attempted doping elements by theoretical calculations and experimental results, lanthanide elements are among the most promising candidates. Their abundant 4f energy levels render the ability to tune and extend the emission of TMDs host to a wide range of spectrum from ultra-violet to infrared. However, the incorporation of lanthanide ions can be challenging owing to the high melting point of their metal oxide precursors. In our previous works, the synthesis of MoS<sub>2</sub>: Er film and WS<sub>2</sub>: Yb/Er film have been demonstrated through chemical vapor deposition (CVD) and pulsed laser deposition (PLD) approaches, respectively. Both results exhibited efficient near infrared (NIR) emissions from Er<sup>3+</sup> dopants, which is of vital importance in optical communication applications.

In this thesis, the NIR emission of lanthanide Er<sup>3+</sup> ions in MoS<sub>2</sub> single crystals was studied using an ingenious two-step CVD method. Er-doped Mo metal film was first deposited on the substrate as growing seeds, followed by a sulfurization procedure in a conventional CVD furnace. Under high sulfur vapor concentration, the growing seeds evaporated from the metal film were sulfurized and self-assembled into single

crystal islands at the downstream part of the substrate. The morphology and chemical composition of pristine and Er-doped MoS<sub>2</sub> single crystals were compared using optical microscopy, atomic force microscopy (AFM), Raman spectroscopy, and energy dispersive X-Ray spectroscopy (EDX). The Raman spectrum of the Er-doped MoS<sub>2</sub> single crystal slightly shifted to the lower energy compared with their pristine counterparts, due to the distortion induced by the incorporated Er atom on MoS<sub>2</sub> host matrix. The NIR emission of Er dopant was characterized by steady state photoluminescence spectroscopy with an excitation wavelength of 980 nm. The luminescence of MoS<sub>2</sub> single crystal host was successfully extended to the NIR range at 1530 nm, corresponding to the energy transfer between <sup>4</sup>I<sub>13/2</sub> and <sup>4</sup>I<sub>15/2</sub> 4f levels of Er<sup>3+</sup> ions. The broad emission band consisted of two peaks centered at 1529 and 1505 nm, respectively. This energy level splitting phenomena of Er<sup>3+</sup> dopant was induced by the surrounding electric field of host MoS<sub>2</sub> nanosheets. Besides, the concentration dependent curve of the luminescence intensity at 1530 nm was measured. The concentration quenching effect was observed with an optimal Er content of 4 mol%, attributing to the increase of non-radiative decay process between the neighboring dopant atoms favored at high Er concentration. Moreover, the stability of the doped system under different chalcogen source content was investigated using first principle calculations. The structural and electronic properties were simulated and compared for pristine and Er-doped MoS<sub>2</sub> monolayer. The doping energy levels of lanthanide Er<sup>3+</sup> were located with respect to MoS<sub>2</sub> band structure by combining the density of state (DOS) calculation results with the Dieke Diagram (a complete energy level diagram documented for lanthanide 4f levels). The simulated band structure of Er-doped MoS<sub>2</sub> was well consistence with our experimental findings, which provides an in-depth understanding of lanthanide doping in 2D layered semiconducting materials.

This two-step CVD approach to synthesize doped TMDs single crystal offers a new possibility to develop doping strategies for layered atomic thin materials. This method has great potential to be generalized to the synthesis of various 2D TMDs, especially those involving doping or alloying functionalization. The developed Er-doped MoS<sub>2</sub> single crystals are promising in both fundamental research and potential applications in atomically thin NIR photonic and optoelectronic devices.

## List of Publications

1. **Yongxin Lyu**, Zehan Wu, Weng Fu Io and Jianhua Hao\*, "Observation and theoretical analysis of near-infrared luminescence from CVD grown lanthanide Er doped monolayer MoS<sub>2</sub> triangles", *Appl. Phys. Lett.*, 2019, **115**, 153105.
2. Zhibin Yang, Zehan Wu, **Yongxin Lyu**, and Jianhua Hao\*, "Centimeter-scale growth of 2D layered high-mobility bismuth films by pulsed laser deposition", *InfoMat.*, 2019, **1**, 98.
3. Gongxun Bai, **Yongxin Lyu**, Zehan Wu, Shiqing Xu\*, Jianhua Hao\*, "Lanthanide near-infrared emission and energy transfer in layered WS<sub>2</sub>/MoS<sub>2</sub> heterostructure", *Sci. China Mater.*, 2020, **63**, 575-581.
4. Feng Guo, **Yongxin Lyu**, Michal Bartlomiej Jedrzejczyk, Yuqian Zhao, Weng Fu Io, Gongxun Bai, Wenzhuo Wu, and Jianhua Hao\*, "Piezoelectric biaxial strain effects on the optical and photoluminescence spectra of 2D III-VI compound  $\alpha$ -In<sub>2</sub>Se<sub>3</sub> nanosheets", *Appl. Phys. Lett.*, 2020, **116**, 113101.



## Acknowledgements

It has been a long and at times daunting journey for the past two years of my MPhil study. It is truly an enriching experience, not only from the academic aspect but also from the aspect of personality. Now my thesis is at the current stage of completion, I would like to show thankfulness to those who have accompanied me through this special journey.

First and foremost, I would like to express my sincere gratitude to my supervisor, Prof. Jianhua Hao, who gave me the invaluable opportunity to pursue my MPhil study in PolyU. His passion and profound academic insight for scientific research has inspired me in all the times of research and preparing this thesis. I genuinely admire his selfless support and assistance to all of his students in both research study and personal development. Without his patient guidance and continuous support, the accomplishment of my MPhil study would not be achieved.

I would like to extend my appreciation to the all the academic and technical staffs of our department, who provide invaluable assistance to my experimental research and course works. And I would like to give my special thanks to Prof. Jiyan Dai and Dr. ONOFRIO Nicolas for their generous support and care.

My sincere thanks also goes to my dear groupmates Dr. Gongxun Bai, Mr. Zehan Wu, Dr. Wei Xu, Dr. Zhibin Yang, Mr. Shuoguo Yuan, Mr. Man-Chung Wong, Ms. Weng Fu Io, Dr. Ran Ding, Dr. Beining Zheng, Mr. Feng Guo, Mr. Menglin Song, Ms. Sin Yi Pang, Ms. Yuqian Zhao, and Mr. JEDRZEJCZYK Michal Bartlomiej, for

their stimulating suggestions, encouragement and for all the fun we have had in the last two years. And to my dear friends, Mrs. Lejuan Cai, Ms. Lina Chan, Ms. Qin Wang, huge thanks for keeping me company along the way.

I gratefully acknowledge the financial support from Research Grants Council of Hong Kong (RGC GRF No. PolyU 153281/16P).

Finally, my deepest gratitude goes to my beloved family for their unconditional support and endless love throughout those tough moments in my life. I am forever indebted to my parents for their selfless encouragement to explore new directions in life and seek my own destiny. This journey would not have been possible if not for them, and I dedicate this milestone to them.



# Table of Contents

Abstract .....	I
List of Publications .....	IV
Acknowledgements.....	VI
Table of Contents.....	VII
List of Figures.....	XI
List of Tables.....	XV
Chapter 1 Introduction .....	1
1.1    Background of layered semiconductor nanosheets .....	1
1.2    Doping of Two-dimensional layered materials.....	3
1.2.1    Principle of doping .....	3
1.2.2    Possible doping elements .....	5
1.2.3    Doping strategies .....	6
1.2.4    Practical applications of doped 2D semiconductor .....	12
1.3    Luminescence of lanthanide elements.....	12
1.3.1    Basic principles of lanthanide elements.....	12
1.3.2    Application of lanthanides in 2D semiconducting materials .....	16



1.4	Background on atomistic modeling and simulation.....	19
1.5	Significance of research.....	21
1.6	Thesis overview .....	23
Chapter 2 Experimental Techniques and Theoretical Analysis .....		24
2.1	Sample preparation.....	24
2.1.1	Magnetron sputtering.....	24
2.1.2	Chemical vapor deposition.....	26
2.2	Structural characterizations.....	28
2.2.1	X-ray diffraction.....	28
2.2.2	Atomic force microscopy.....	29
2.2.3	Energy dispersive X-ray spectroscopy .....	30
2.3	Optical properties measurements .....	31
2.3.1	Raman spectroscopy .....	32
2.3.2	Steady-state photoluminescence spectroscopy.....	34
2.4	Density functional theory calculations .....	36
2.4.1	Basic principles of density functional theory.....	36
2.4.2	Quantum ESPRESSO .....	37
Chapter 3 Synthesize and Characterization of Pristine MoS <sub>2</sub> Nanosheets.....		39
3.1	Introduction.....	39
3.2	Molten-salt-assisted CVD growth of monolayer MoS <sub>2</sub> .....	40
3.2.1	Experimental details .....	40

---



3.2.2	Key parameters.....	42
3.2.3	Reaction mechanism.....	46
3.2.4	Layer-dependent properties of MoS <sub>2</sub> .....	47
3.3	Two-step metal-precursor-based deposition of MoS <sub>2</sub> .....	51
3.3.1	Experimental details .....	51
3.3.2	In-situ sulfurization.....	53
3.3.3	Gas phase induced transfer.....	54
3.4	Summary .....	55
Chapter 4	Near Infrared Luminescence of Er-Doped MoS <sub>2</sub> Monolayer .....	54
4.1	Introduction.....	54
4.2	Experimental details .....	55
4.3	Comparison of Er-doped and pristine MoS <sub>2</sub> monolayer .....	56
4.3.1	Structural property characterization .....	56
4.3.2	Chemical composition characterization.....	59
4.3.3	Raman characterization.....	60
4.3.4	Optical properties characterization.....	61
4.4	Er <sup>3+</sup> NIR Photoluminescence properties analysis .....	63
4.4.1	NIR PL characterizations .....	63
4.4.2	Energy transfer mechanism.....	65
4.5	Summary .....	67

---



Chapter 5      Density Functional Theory Calculation of Er-doped MoS <sub>2</sub> Monolayer	68
5.1      Introduction.....	68
5.2      Computational details.....	69
5.2.1      Density functional theory details.....	69
5.2.2      Doping procedure .....	70
5.2.3      Simulation analysis.....	70
5.3      Structure properties and energetics .....	72
5.3.1      Crystal structure of pristine and Er-doped MoS <sub>2</sub> monolayer .....	72
5.3.2      Doping energy calculation .....	72
5.4      Electronic properties.....	73
5.4.1      Density of state calculation .....	73
5.4.2      Electronic band structure calculation.....	74
5.5      Summary.....	75
Chapter 6      Conclusion and Future Prospects.....	78
6.1      Conclusion .....	78
6.2      Future prospects .....	80
References .....	82

## List of Figures

Figure 1.1 2D materials family beyond graphene. ....	2
Figure 1.2 a) Existing 2D TMDs compounds with metal and chalcogen elements highlighted in the periodic table. b) Crystal structure of 2D layered MoS <sub>2</sub> . ....	3
Figure 1.3 A table of potential doping elements on MoS <sub>2</sub> by theoretical calculation. ....	5
Figure 1.4 CVT setup of MoS <sub>2</sub> :Nb bulk crystal with a three-zone furnace.....	9
Figure 1.5 a) The schematic presentation for synthesize of Re-doped MoS <sub>2</sub> monolayer. b) SEM image of Re-doped MoS <sub>2</sub> monolayer. Scale bar, 5 μm. ....	10
Figure 1.6 a) Schematic diagram of The CVD setup. b) Lattice structure of WS <sub>2</sub> monolayer with Nb doping on W sites. c) STEM image of prepared Nb doped WS <sub>2</sub> monolayer. Scale bar, 1 nm. ....	11
Figure 1.7 a) Schematics of gas phase reaction of Mn doped MoS <sub>2</sub> . b) graphene and c) traditional substrates used to grow the material. ....	11
Figure 1.8 Radical probability regarding 4f, 5d, 6s orbitals of lanthanide ions.....	13
Figure 1.9 Dieke diagram of electronic transition of trivalent lanthanide ions.....	15
Figure 1.10 Impact of lanthanide doping on emission spectrum range of 2D TMDs. ....	16
Figure 1.11 a) A schematic synthesis process and b) PL emission mechanism. c) The up-conversion and d) Down-conversion emission of Er-doped MoS <sub>2</sub> thin film.....	18

Figure 1.12 a) Experimental setup of quasi-closed crucible CVD system. b) Temperature profile of Er-doped MoS <sub>2</sub> film growth. c) A schematic of the synthesis process.....	19
Figure 1.13 a) Preparation of Yb/Er co-doped WSe <sub>2</sub> thin film by PLD. b) optical image of Yb/Er doped WSe <sub>2</sub> . Scale bar, 100 μm. PL spectrum of Yb/Er doped WSe <sub>2</sub> at c) 800 and d) 1550 nm. ....	19
Figure 1.14 Multi-scale view of computational materials. .....	20
Figure 2.1 Schematic illustration of magnetron sputtering system. ....	25
Figure 2.2 Setup of the magnetron sputtering system. ....	26
Figure 2.3 Schematic diagram of the homemade CVD system. ....	27
Figure 2.4 Basic X-ray diffractometer setup.....	28
Figure 2.5 Block diagram of atomic force microscopy. ....	30
Figure 2.6 Schematic principle of energy dispersive X-ray spectroscopy.....	31
Figure 2.7 Fundamental principles of Raman and Rayleigh scattering. ....	32
Figure 2.8 Schematic illustration of the confocal Raman system. ....	33
Figure 2.9 Photography of the PL spectrometer in our laboratory.....	35
Figure 2.10 Equipment configuration of the FLS900 spectrometer. ....	36
Figure 3.1 CVD setup for the growth of MoS <sub>2</sub> single crystal. ....	41
Figure 3.2 Growing temperature profile of the deposition process.....	42
Figure 3.3 Optical image of MoS <sub>2</sub> flakes obtained under different reaction temperatures: a) 650°C, b) 700°C, c) 750°C, and d) 800°C. Scale bars, 50 μm.....	43

Figure 3.4 Optical image of MoS <sub>2</sub> samples prepared at 750°C under different growth times: a) 5 min, b) 10 min, c) 15 min, and d) 20 min. Scale bars, 100 μm.....	44
Figure 3.5 Optical image of the MoS <sub>2</sub> flakes obtained at 750°C with different MoO <sub>3</sub> precursor amount: a) 2 mg, b) 5 mg, c) 10 mg, and d) 20 mg. Scale bars, 100 μm. .	45
Figure 3.6 a) and b) Optical image of representative MoS <sub>2</sub> flakes with different layer numbers. Scale bars, 50 μm. ..	47
Figure 3.7 a) Raman spectrum of monolayer to a few layer MoS <sub>2</sub> . b) Peak frequency and peak position separation of MoS <sub>2</sub> with varying layer numbers. ....	49
Figure 3.8 Layer dependent PL spectrum of prepared MoS <sub>2</sub> samples.....	50
Figure 3.9 EDX spectrum of prepared MoS <sub>2</sub> samples.....	51
Figure 3.10 Preparation of Mo metal film precursor by magnetron sputtering. ....	52
Figure 3.11 Setup for the sulfurization of pre-deposited metal film. ....	52
Figure 3.12 Growing temperature and gas flow profile of the deposition process. ..	53
Figure 3.13 a) A schematic of In-situ sulfurization scheme. b) optical microscopy image of the MoS <sub>2</sub> film after sulfurization. Scale bar, 20 μm. ....	54
Figure 3.14 a) A schematic of the gas phase induced transfer scheme. b) Optical microscopy image of the resulting MoS <sub>2</sub> film and triangle domains. Scale bar, 20 μm. ....	55
Figure 4.1 Flow chart of the growth process for Er-doped MoS <sub>2</sub> by the two-step alloy based synthesize method. ....	56

Figure 4.2 Optical images of a) Er-doped MoS <sub>2</sub> and b) pristine MoS <sub>2</sub> grown on Si/SiO <sub>2</sub> substrate. Scale bars, 10 μm. AFM images of c) Er doped MoS <sub>2</sub> and d) pristine MoS <sub>2</sub> single crystals. Scale bars, 1 μm.....	57
Figure 4.3 XRD patterns of undoped and Er-doped MoS <sub>2</sub> . .....	58
Figure 4.4 EDS results of Mo, S and Er elements on prepared Er doped MoS <sub>2</sub> . ....	59
Figure 4.5 XPS results of Er-doped MoS <sub>2</sub> a) Mo 3d, S 2s, and b) Er 4d core levels.	60
Figure 4.6 a) Raman spectrum of undoped and Er-doped MoS <sub>2</sub> monolayer. Raman mapping of the b) E <sub>2g</sub> <sup>1</sup> in-plane mode and c) A <sub>1g</sub> out-of-plane mode on Er-doped MoS <sub>2</sub> monolayer. Scale bars, 2 μm. ....	61
Figure 4.7 a) PL spectrum of undoped and Er-doped MoS <sub>2</sub> monolayer. b) PL mapping of bandgap emission of Er-doped MoS <sub>2</sub> . Scale bar, 2 μm. ....	62
Figure 4.8 a) NIR down-shifting luminescence of Er-doped MoS <sub>2</sub> with different Er <sup>3+</sup> concentration pumped by 980 nm laser. b) Er <sup>3+</sup> concentration dependence on NIR luminescence intensity of Er-doped MoS <sub>2</sub> . ....	64
Figure 4.9 The pump power dependence of PL intensity at 1530 nm emission peak. ....	65
Figure 4.10 PL spectra mapping image of 1530 nm emission peak of nine spots in a line. ....	65
Figure 4.11 Diagram of stark manifold of partial 4f levels of Er <sup>3+</sup> ions.....	66
Figure 5.1 a) Top view and b) side view of Er doped supercell. Blue, yellow and orange balls represent Mo, S, Er atoms, respectively. ....	70
Figure 5.2 Calculated DOS of Er-doped MoS <sub>2</sub> monolayer.....	74

Figure 5.3 Schematic partial energy level diagram of  $\text{Er}^{3+}$  ion doped in 2D  $\text{MoS}_2$ . . 75

## List of Tables

Table 1.1 Cation substitutional doping of MX <sub>2</sub> using various doping strategies.....	7
Table 5.1 Calculated lattice parameters of Er doped MoS <sub>2</sub> monolayer .....	72
Table 5.2 Computed energies of various compounds.....	73

# Chapter 1

## Introduction

### 1.1 Background of layered semiconductor nanosheets

Layered two-dimensional (2D) materials have been extensively investigated over the past few years for both fundamental research and device application.<sup>11</sup> Layered materials, when approaching their physical limits, exhibit fascinating physical properties which are different from their parent three-dimensional materials.<sup>15,81</sup> Their ultimate thickness has opened up a new degree of freedom for material engineering and device fabrication. Graphene, as the most highly studied member of 2D materials, was demonstrated to possess high mobility and thermal conductivity, making it fundamentally and technologically interesting for electronic, electrochemical, optoelectronic and biomedical applications.<sup>100</sup> Nevertheless, the chemical inertness and metallic nature of pristine graphene nanosheet hinder a variety of potential applications, such as catalysis, sensing, energy storage, and light emitting devices. Rapidly following graphene, the development in ultrathin layer fabrication techniques led to the exploration of a wide spectrum of 2D material candidates, including transition metal dichalcogenides (TMDs), black phosphors, MXenes and mono-elemental 2D semiconductors (phosphorene, silicene, germanene) (see Figure 1.1).<sup>13,73</sup>

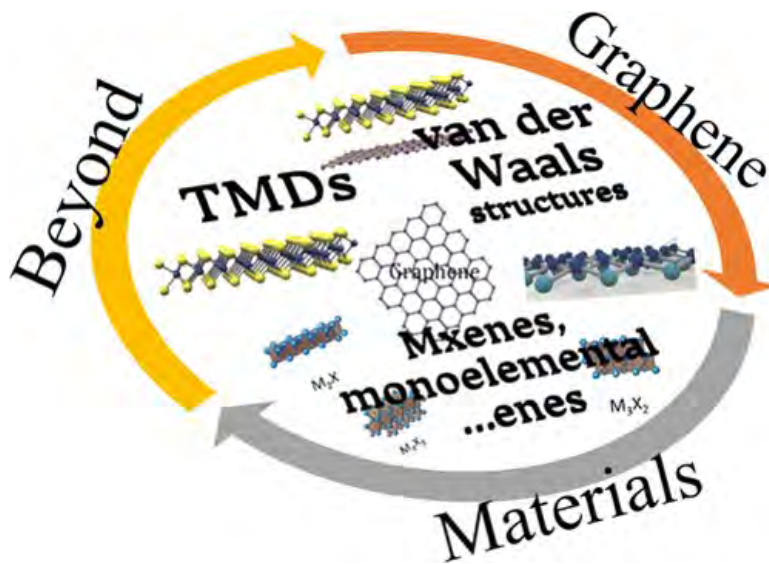


Figure 1.1 2D materials family beyond graphene.

In particular, 2D TMDs have drawn considerable attentions since they combine the ultimate atomically thickness of graphene and exceptional semiconductor properties with a sizable optical bandgap of 1-2 eV.<sup>12,116</sup> TMDs are a group of layered materials coupled by weak van der Waals (vdW) forces with a generalized formula of  $\text{MX}_2$ , as shown in Figure 1.2a. The hexagonally packed layers stacking in the sequence of X-M-X form the structure of TMDs (see Figure 1.2b), where M represents the central transition metal of group 4-10 and X represents the surrounding chalcogen element.<sup>12</sup> Each layer has a typical thickness of 6~7 Å, where the metal and chalcogen atoms are bounded covalently.

Research has demonstrated that the band structure of these 2D TMDs change dramatically as they are thinned to single layer thickness owing to the quantum confinement effect.<sup>23,47</sup>  $\text{MoS}_2$  nanosheets, as the most highly investigated prototype of TMDs material, experience a transition from indirect bandgap semiconductor for bulk crystals to direct bandgap semiconductor for monolayer, resulting in a dramatic increase in the photoluminescence yield. Most atomically thin TMDs have been

observed to possess strong near-infrared absorption and emission properties, making them promising candidates for constructing light emitting devices.<sup>15</sup> Moreover, 2D TMDs materials are also found to have a tunable bandgap by electric field and mechanical strain, which widens the application of atomically thin TMDs for constructing optoelectronic and electric devices.<sup>99</sup>

**(a)**

MX <sub>2</sub> M = Transition metal X = Chalcogen														
H													He	
Li	Be													
Na	Mg	3	4	5	6	7	8	9	10	11	12			
K	Ca	Sc	Ti	V	Cr	Mn	Fe	Co	Ni	Cu	Zn	Ga	Ge	As
Rb	Sr	Y	Zr	Nb	Mo	Tc	Ru	Rh	Pd	Ag	Cd	In	Sn	Te
Cs	Ba	La-Lu	Hf	Ta	W	Re	Os	Ir	Pt	Au	Hg	Tl	Pb	Bi
Fr	Ra	Ac-Lr	Rf	Db	Sg	Bh	Hs	Mt	Ds	Rg	Cn	Uut	Fl	Uup
													Lv	Uus
														Uuo

**(b)**

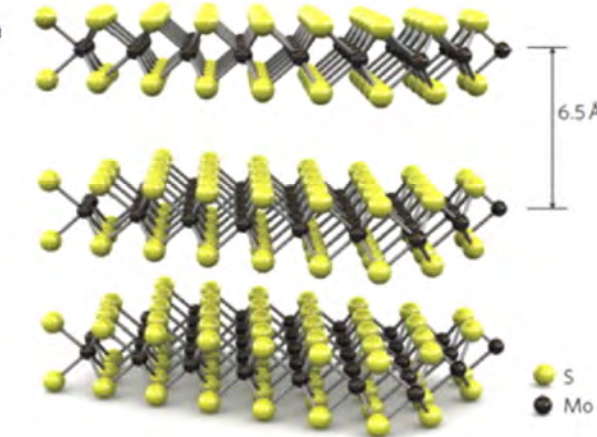


Figure 1.2 a) Existing 2D TMDs compounds with metal and chalcogen elements highlighted in the periodic table. b) Crystal structure of 2D layered MoS<sub>2</sub>.

## 1.2 Doping of Two-dimensional layered materials

### 1.2.1 Principle of doping

Despite the significant promise of 2D layered semiconducting materials for electronic applications, a single 2D layered material cannot satisfy all the functional performance and basic properties requirement in applications of practical technology.<sup>73</sup> Much effort has been devoted to exploring the true potential of these 2D layered materials to realize enhanced device performance and reliability. For example, the ultrathin nature of these materials renders the ability to stack various 2D building blocks in desired sequence to create novel hybrid architectures.<sup>14,29,101</sup> Besides, the electronic property of a 2D semiconducting material can be tuned by introducing strain, applying external stress, surface adsorption, or through doping engineering.<sup>36,56,77</sup> As one of the most attracted investigations in semiconducting device technology, doping engineering offers the tuning of semiconducting properties by incorporating suitable dopants with appropriate concentration and chemical environment of host matrix.<sup>89</sup> The study on controlled doping of 2D layered semiconductors is critical to correct and enhance the device performance for next generation electronic applications.

Current strategies employed to achieve the doping engineering of 2D layered semiconductors are mainly devoted to TMDs materials. In practical applications, the mobility of 2D TMD is incomparable to that of graphene, making it unsuitable to be used as a transparent electrode.<sup>107</sup> Therefore, the fabrication of TMDs-based devices requires doping engineering and functionalization of pristine TMDs to take advantage of their superior characteristics and pursue ultimate performance. Up to now, the primary strategies employed to realize the controlled doping of TMDs include substitutional doping, charge transfer doping, intercalation doping, and electrostatic field effect doping.<sup>9,28</sup> The doping strategies mentioned in this chapter are mainly based on substitutional doping of  $\text{MX}_2$  on M or X sites. In the following subsections,

both the theoretical and experimental aspects of doping will be introduced by taking atomically thin MoS<sub>2</sub> as an example.

### 1.2.2 Possible doping elements

In a typical MX<sub>2</sub> crystal lattice, non-metal dopants tend to replace the anionic atoms at the outer layers, while the favorable position of foreign metal dopants depend on their radii.<sup>64,73</sup> For light dopants with smaller radii, such as Na, Li and K, cation interstitials doping is preferred owing to the length limitation of ionic bonds. While for heavy metals with larger radii, like the transition metal atoms, substitutional doping in cation sites is thermodynamically preferred.

Potential substitutional dopants on monolayer MoS <sub>2</sub>														
H								B	C	N	O	F		
	Sc	Ti	V	Cr	Mn	Fe	Co	Ni			P		Cl	
	Y	Zr	Nb		Tc	Ru	Rh	Pd	Ag	Cd		As	Se	Br
				Re					Au				I	

■ Transition metal elements      ■ Non-metal elements

Figure 1.3 A table of potential doping elements on MoS<sub>2</sub> by theoretical calculation.

To investigate the effect of substitutional doping on MX<sub>2</sub> host lattice, theoretical calculations have been demonstrated based on first-principle calculations and density functional theory.<sup>67,108,110</sup> The thermal stability of doping was evaluated in terms of formation energy of substitutional doping and the resulting electronic band structure. In Figure 1.3, a library of possible doping elements on MoS<sub>2</sub> monolayer is summarized from previous reported first principle calculations. A wide range of

possible substitutional dopants, ranging from transition metal to non-metal elements, have been predicted for MoS<sub>2</sub> monolayer.<sup>67,108,110</sup> Cation substitutional doping by transition metal (Y, Zr, Nb, Ru, Rh, Pd, Ag, Cd, Re) and anion substitutional doping by non-metal elements (N, P, As, F, Cl, Br, I) have been studied systematically by calculating the formation energy and the electronic structures of the doped monolayer MoS<sub>2</sub>.<sup>22</sup> The study on doping formation energy implied that cation doping is preferred in the presence of Mo vacancies, while the anion doping, conversely, highly depends on the concentration of S vacancies. Yue et al. investigated the electronic, structural and magnetic properties of single layer MoS<sub>2</sub> incorporated with a variety of non-metal atoms (H, B, C, N, O, F) on S sites and metal atoms (V, Cr, Mn, Fe, Co, Ni) on Mo sites.<sup>108</sup> The calculated electronic density of state revealed that whether the foreign dopant act as donors or acceptors is determined by the valence electrons configurations of the dopant element, which is consistent with the experiment findings. The use of those computational power on ab-initio study has greatly advanced the screening of effective dopants and the designing of 2D materials functionalization.

### 1.2.3 Doping strategies

In practical experiments, the doping of 2D TMDs by replacing cationic and anionic atoms has been investigated extensively using a variety of approaches. In the X-M-X host matrix, substitutional doping of the encapsulating anion atoms can be conveniently achieved since the chalcogenides are exposed to the outer surface. Apart from in-situ doping during the synthesize of the TMDs host, experiments have been demonstrated to realize the anion doping in post-treatment process, such as laser and plasma treatment.<sup>5,40,53</sup> In contrast, the metal atoms are generally screen by the outer chalcogen layer, which screens the incorporation of foreign dopants in the post-

treatment. Therefore, it is the usual case to incorporate cation dopants by optimizing reaction conditions or precursor composition during the in-situ growth of TMDs host. A summary of cation substitutional doping realized so far by experiment with the respective doping type and doping strategy is presented in Table 1.1.

Table 1.1 Cation substitutional doping of  $\text{MX}_2$  using various doping strategies

<b><math>\text{MX}_2</math></b>	<b>Dopant type</b>	<b>Doping strategy</b>	<b>Morphology</b>	<b>Ref</b>
$\text{MoS}_2$	Nb	Mechanical exfoliation	Nanosheets	86,87
$\text{MoS}_2$	Nb	Sulfurization	Thin film	45
$\text{WSe}_2$	Ni	Mechanical exfoliation	Nanosheets	32
$\text{MoS}_2$	Re	Mechanical exfoliation	Nanosheets	50
$\text{MoS}_2$	Re	Liquid reaction	Nanoparticle	105
$\text{MoS}_2$	Re	Direct CVD	Single crystal	111
$\text{MoS}_2$	Er	Sulfurization	Thin film	8
$\text{WS}_2$	Nb	Direct CVD	Single crystal	28
$\text{WSe}_2$	Yb/Er	PLD	Thin film	7
$\text{MoS}_2$	Mn	Direct CVD	Single crystal	112
$\text{MoS}_2$	Fe	Mechanical exfoliation	Nanosheets	97
$\text{MoS}_2$	Mn	Hydrothermal reaction	Nanosheets	88

MoS <sub>2</sub>	W	Direct CVD	Single crystal	3
WS <sub>2</sub>	Cu	Sulfurization	Thin film	<sup>103</sup>

Most of the TMDs layers with high crystallinity and uniform morphology are synthesized using vapor phase deposition methods. Basically, the fabrication scheme can be divided into two types: top-down and bottom-up route. The top-down method involves the most primary approach to obtain 2D materials, which is mechanical exfoliation of thin layers using Scotch tape from their bulk crystals. The doping of cation atoms is performed in the synthesize process of parent 3D crystal, which is in most cases the chemical vapor transport (CVT) method.<sup>86,87</sup> The schematic setup for the growth of Nb-doped MoS<sub>2</sub> crystal is presented in Figure 1.4. A sealed ampoule containing the elemental precursors (Mo, S, Nb) and a small amount of transporting agent (I<sub>2</sub>) was vacuumed and calcinated in a three-temperature-zone furnace. The precursors diffused through the temperature gradients, and high quality Nb-doped MoS<sub>2</sub> were crystalized at the growth end. Using the similar top-down method, the substitutional doping of Re and Fe atoms on exfoliated MoS<sub>2</sub> nanosheets have also been demonstrated.<sup>50,97</sup> Although the mechanical exfoliation yields 2D nanosheets with the highest crystal quality, it is obviously not an ideal method for large scale production of 2D materials.

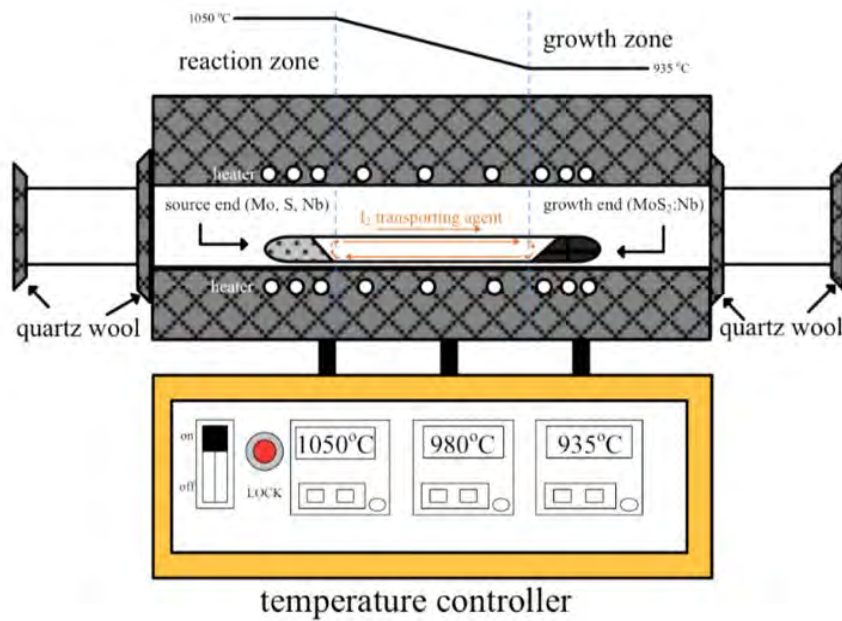


Figure 1.4 CVT setup of MoS<sub>2</sub>:Nb bulk crystal with a three-zone furnace.

To fabricate large-scale 2D TMDs in thin film or single crystal form, bottom-up approaches such as direct CVD has been an effective way of cation in-situ doping. This method can be refined to control the domain size and layer number of the host material, and it can be easily adapted for incorporation of foreign dopants during the synthesis. Promising source materials candidates to supply dopant atoms during the CVD growth include pure metal elements, metal oxides, sulphides, tellurides, halides and metal salts.

Substitutional doping of MoS<sub>2</sub> monolayer by Re atoms has been demonstrated successfully using metal oxide as reacting precursor.<sup>111</sup> A schematic setup of the three-zone furnace for Re doping is presented in Figure 1.5a. The Rhenium oxide (ReO<sub>3</sub>) precursor was heated close to its decomposition temperature to supply the foreign dopant in vapor phase. As shown in Figure 1.5b, the growth yielded high quality Re-doped MoS<sub>2</sub> triangular domains.

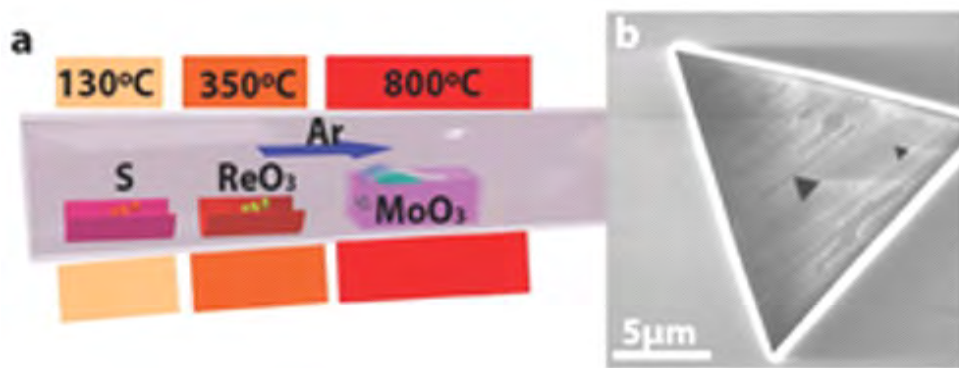


Figure 1.5 a) The schematic presentation for synthesize of Re-doped  $\text{MoS}_2$  monolayer. b) SEM image of Re-doped  $\text{MoS}_2$  monolayer. Scale bar, 5  $\mu\text{m}$ .

On the other hand, for dopant types whose oxide compounds have extremely high melting point, melt salts with low decomposition temperature can be a promising candidate as source material. In 2016, Gao et al. demonstrated the incorporation of Nb on W sites of  $\text{WS}_2$  host with monolayer thickness.<sup>28</sup> The inclusion of Nb was achieved by direct vapor phase deposition from the powder precursors: tungsten trioxide ( $\text{WO}_3$ ), niobium chloride ( $\text{NbCl}_5$ ) and elemental sulfur (see Figure 1.6a). The identification of Nb position in monolayer  $\text{WS}_2$  was performed by scanning transmission electron microscopy (STEM) as exhibited in Figure 1.6c. In another study, the incorporation of Mn atoms at Mo sites was performed using a salt precursor dimanganese decacarbonyl ( $(\text{Mn}_2(\text{CO})_{10})$ ) via vapor phase deposition technique (see Figure 1.7).<sup>112</sup> It was demonstrated that the influence of growing substrate on the ease of Mn doping was significant. The inert substrates, such as graphene, permit the substitutional doping of Mn with a detectable content. The reactive substrates, such as  $\text{SiO}_2$  and sapphire, terminate the in-situ Mn incorporation, and the host  $\text{MoS}_2$  layers tend to be more prone to defects.

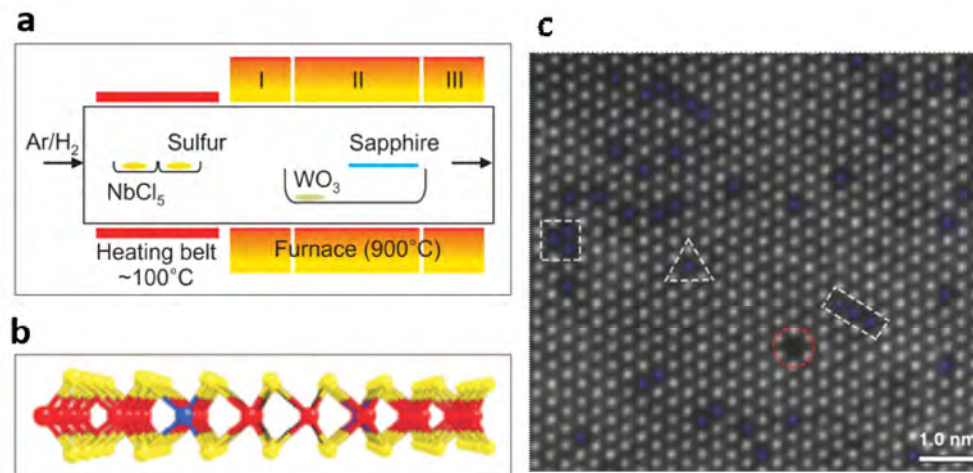


Figure 1.6 a) Schematic diagram of The CVD setup. b) Lattice structure of WS<sub>2</sub> monolayer with Nb doping on W sites. c) STEM image of prepared Nb doped WS<sub>2</sub> monolayer. Scale bar, 1 nm.

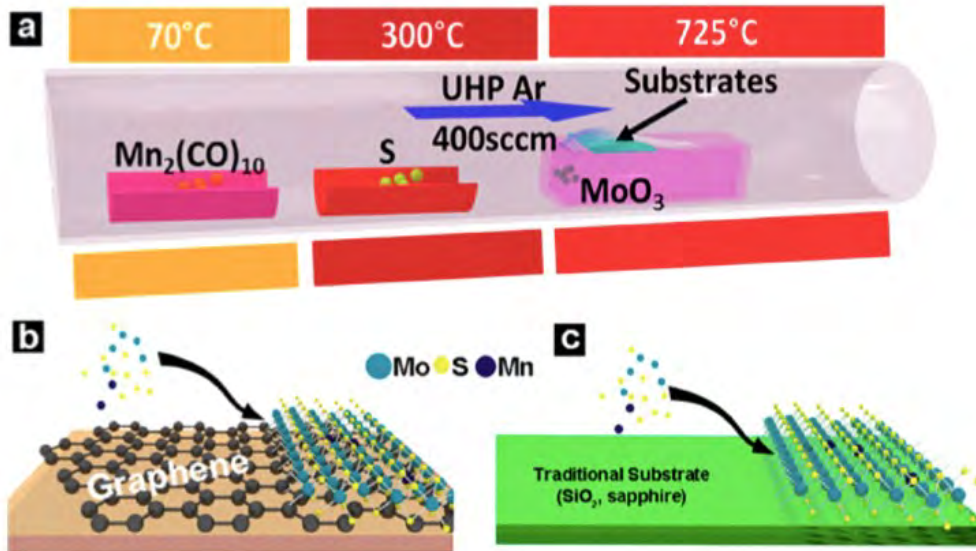


Figure 1.7 a) Schematics of gas phase reaction of Mn doped MoS<sub>2</sub>. b) graphene and c) traditional substrates used to grow the material.

Apart from vapor phase deposition method, a variety of other doping strategies have been investigated.<sup>104</sup> Lasker et.al<sup>145</sup> demonstrated the doping of Nb atoms in MoS<sub>2</sub> thin film by diffusion of Nb atoms in a multilayer Mo/Nb/Mo structure during

sulfurization process. Tan et al. successfully synthesized Mn-doped MoS<sub>2</sub> in the form of nanosheets via supercritical hydrothermal reaction.<sup>88</sup> Besides, Re dopant was incorporated into MoS<sub>2</sub> nanoparticles using a liquid based reaction method.<sup>105</sup>

#### 1.2.4 Practical applications of doped 2D semiconductor

The investigation of doping engineering by careful selection of dopants, optimization of doping concentration and doping strategies yield promising properties to be applied in device fabrication. A wide range of devices have been demonstrated, including field effect transistors (FET), photosensors, energy harvesting devices, diodes and transistors, semiconductor integrated circuits, etc.<sup>16,111</sup> For example, the in-situ doping of Nb induced the alteration of semiconducting behavior of MoS<sub>2</sub> from intrinsic n-type to p-type.<sup>45</sup> Novel magnetic properties were introduced to monolayer MoS<sub>2</sub> by incorporating of foreign atoms such as Fe, Mn, Cu, Co.<sup>49,83,112</sup> The performance of hydrogen evolution reaction (HER) catalytic activities of 2D TMDs has been significantly improved via the incorporation of various dopants (e.g., Fe, Co, Ni) on metal sites.<sup>57,95</sup> Besides, the integration of doped 2D TMDs with other 2D layered materials is promising for constructing next-generation functional devices such as energy storage, sensing, communication, memory, etc.

### 1.3 Luminescence of lanthanide elements

#### 1.3.1 Basic principles of lanthanide elements

Lanthanide elements consist of 15 chemical species located at the bottom of the periodic table. They are highly recognized for their versatile applications, including lighting, lasing, electronic display, anticounterfeiting, biological labeling, and imaging.<sup>6,76</sup>

Lanthanide elements possess a unique electronic configuration of  $[Xe]6s^25d^14f^n$ , where the integer n denotes the occupation of 4f orbital, with n ranging from 0 (La) to 14 (Lu) depending on their atomic number. Basically, the luminescence properties of lanthanide elements involve the electronic transitions between their 4f and 5d orbitals.<sup>55</sup> The radical probability distribution of the valence electrons in lanthanide ions can be derived from theoretical wave function calculations of many-body system. As depicted in Figure 1.8, the underlying 4f electrons are shielded by 6s and 5d electrons in the outer shell, which results in the insensitivity of 4f orbitals to their chemical environment.

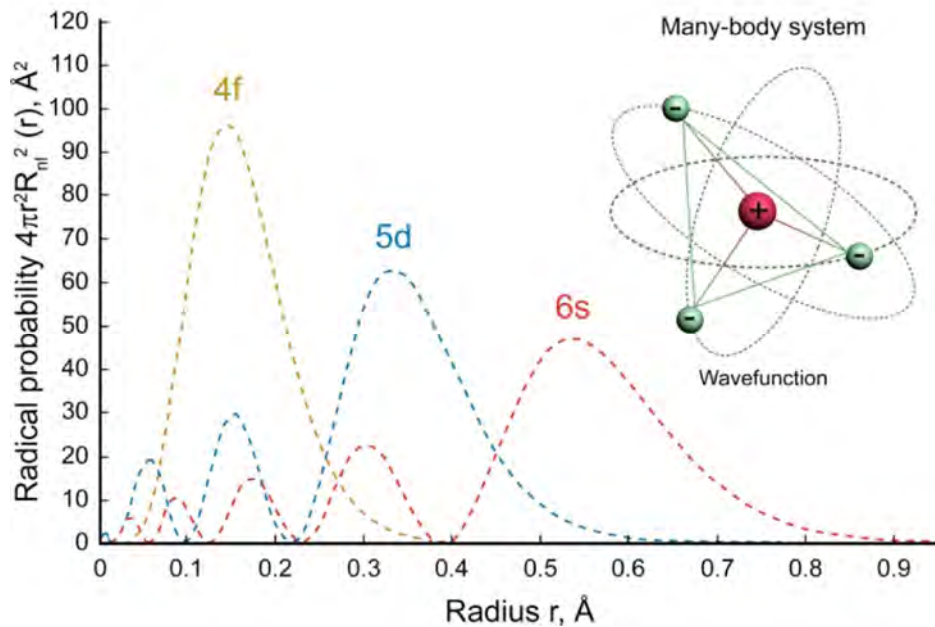


Figure 1.8 Radical probability regarding 4f, 5d, 6s orbitals of lanthanide ions.

Base on the description about energy levels in lanthanide elements above, the major optical transitions in lanthanide-based materials can be classified into three kinds of mechanism: the intra-configurational electronic transition between 4f orbitals,

the inter-configurational electronic transition between 4f and 5d orbitals, and the inter-configurational charge transfer electronic transition.<sup>54</sup>

The 4f-4f electronic transitions are always associated with sharp peaks owing to the weak dynamic effect of the crystal field on 4f electrons. The emission wavelength of a particular f-f transition of a particular lanthanide ion is independent of the host matrix, though their peak intensity may vary. In contrast, the absorption and emission spectra of 4f-5d transitions always consist of a broad band contributing to the strong phonon coupling effect. And the position of 4f-5d emission peak is strongly dependent on their chemical environment. As an example, Eu<sup>2+</sup> ion can be compiled to over 300 kinds of host materials exhibiting a wide spectrum of emission colors ranging from ultra-violet (UV) to infrared (IR).<sup>24</sup> This property has been utilized in tuning emission properties of lanthanide-based phosphors. Charge transfer electronic transition is of vital importance in the absorption mechanisms of many lanthanide doped phosphors, especially Eu<sup>3+</sup> red phosphors.<sup>21</sup> The absorption is done through electronic transitions between the particularly filled or empty lanthanides and the highest occupied energy level of the ligand.

As a summary to electronic transitions in lanthanide-based phosphor materials, the absorption is generally realized by intense transitions including 4f-5d transitions and charge transfer transitions, exhibiting wide bands. Emission of light is done through 4f-4f intra-configurational transitions and 4f-5d inter-configurational transitions, giving emission spectrum with sharp peaks and wide bands, respectively. Figure 1.9 is the Dieke diagram of electronic diagram of lanthanide ions in LaF lattices. This diagram is a standard in lanthanide luminescence since these energy levels also apply to other host matrices due to the unique nature of shelled 4f orbital electrons.<sup>72</sup>

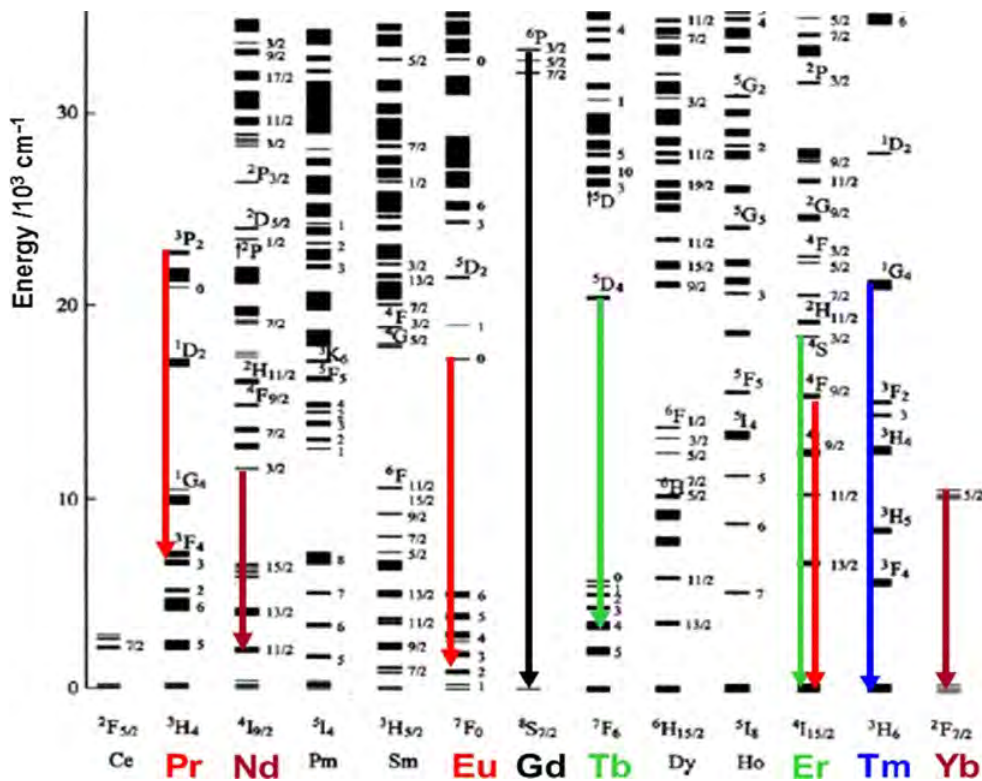


Figure 1.9 Dieke diagram of electronic transition of trivalent lanthanide ions.

Up to now, the lanthanide ions has been used to functionalize and tune the luminescence of wide range of phosphor materials, including glasses, bulk crystals, powders, thin films and nanoparticles.<sup>19,27,102</sup> Compared with phosphor materials based on organic dye or transition metal dopants, lanthanide doped phosphors possess many advantages.<sup>34,115</sup> First, lanthanide ions exhibit a wide emission range from UV to NIR spectrum with excellent quantum efficiency. Besides, lanthanide ions can be compiled to a wide range of host materials due to their high acceptance of coordination numbers. better photostability and outstanding color performance regarding high spatial resolution and color purity. Moreover, these phosphors offer wide optical tunability characteristic in the form of emission wavelength and lifetime.

### 1.3.2 Application of lanthanides in 2D semiconducting materials

Recently, tremendous interest has been devoted to the development of novel optical 2D layered semiconductors through lanthanide doping owing to the precise control over the characteristics of optical emission at single particle levels.

In terms of luminescence, the range of 2D TMDs intrinsic emission spectra is limited from visible to the edge of near infrared.<sup>79,92</sup> Lanthanide ions possess abundant 4f energy levels to absorb and emit photons of a wide spectral range, making them promising candidates for investigations into extending the luminescence of 2D TMDs semiconductors. As depicted in Figure 1.10, the emission range of pristine TMDs nanosheets can be modified and extended to ultraviolet (UV) to near infrared (NIR) spectral range by introducing of lanthanide ions into TMDs lattices.<sup>8</sup>

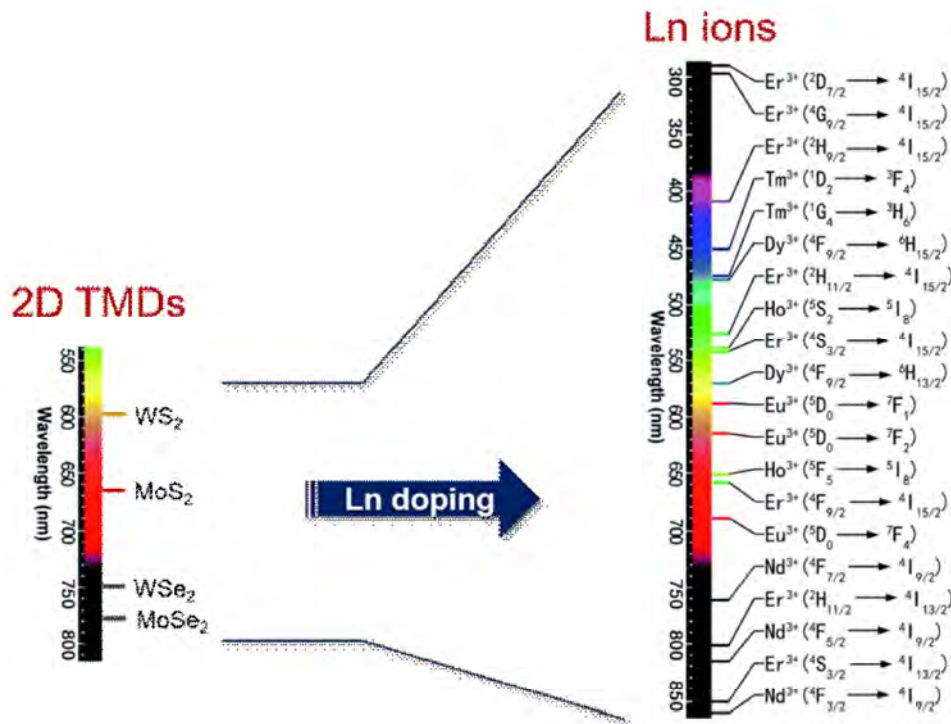


Figure 1.10 Impact of lanthanide doping on emission spectrum range of 2D TMDs.

So far, although the doping engineering of 2D TMDs has been demonstrated with a variety of transition metal elements, introduction of elements with distinct valence and atomic configurations, like the lanthanides, remains challenging.<sup>73</sup> Although the in-situ dopant incorporation has been widely demonstrated using vapor phase deposition approach, candidates for lanthanide source materials during vapor phase deposition growth can be hard to control. The pure lanthanide metals are highly unstable in atmosphere, while the lanthanide oxides require extremely high temperature to evaporate (over 1100°C) and their vapor pressure is too low to supply the lanthanide source.

In our previous work, incorporation of Er<sup>3+</sup> ions into 2D MoS<sub>2</sub> was realized for the first time using a pre-deposition route to deliver metal precursors<sup>8</sup>. A schematic diagram of synthesis process is illustrated by Figure 1.11a. Er-doped MoS<sub>2</sub> thin film was fabricated by sulfurization of stoichiometric Er-doped Mo metal film which was sputtered onto a Si/SiO<sub>2</sub> substrate in advance. The employ of mixed metal precursor has simplified the conventional chemical vapor deposition process by avoiding the complexed control of precursor stoichiometry and interrelated growth parameters. This two-step CVD method holds great promise for growing 2D TMDs thin films in wafer scale, and was also used in other investigations.<sup>45,48</sup> The emission of the host MoS<sub>2</sub> nanosheet has been effectively extended from visible to NIR spectrum. As presented in Figure 1.11b, both up-conversion at 800 nm and down-conversion emission at 1550 nm of Er<sup>3+</sup> ions have been observed under the excitation of a continuous wave diode laser of 980 nm.

In another study, large scale Er-doped MoS<sub>2</sub> film was demonstrated with a quasi-closed crucible CVD method.<sup>106</sup> The incorporation of lanthanide Er was realized

by using  $\text{ErCl}_3 \cdot 6\text{H}_2\text{O}$  as doping precursor. In addition to the function as source material, the evaporated  $\text{ErCl}_3$  also plays a crucial role as assistant agent for the long-distance transmission of  $\text{MoO}_{3-x}$ . As shown in Figure 1.12,  $\text{MoS}_2$  domains absorb on the substrate placed inside the crucible and continue to merge into large-scale monolayer film. The quasi-closed crucible setup slows the rate of sulfurization by reducing the concentration of precursors around the substrate.

In a separate work, ytterbium- and erbium-doped  $\text{WSe}_2$  thin film has been prepared by a fast one-step pulsed laser deposition (PLD) process.<sup>7</sup> As is shown in Figure 1.13, the synthesized thin film exhibit wafer scale, high crystallinity, and high textured feature. Under the excitation of 980 nm laser, the NIR emission at 1550 nm is promoted by the incorporation of  $\text{Yb}^{3+}$  compared with the  $\text{Er}^{3+}$  doped samples.

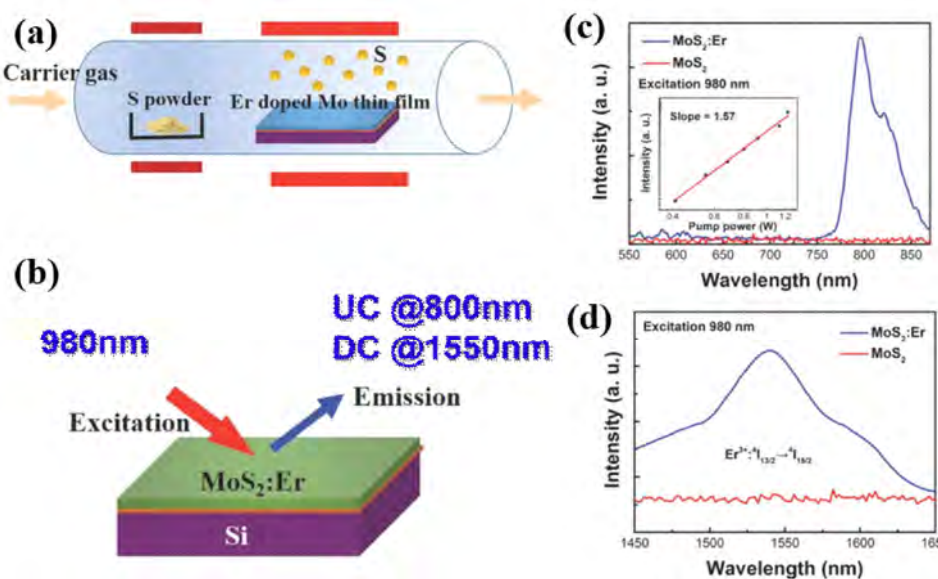


Figure 1.11 a) A schematic synthesis process and b) PL emission mechanism. c) The up-conversion and d) Down-conversion emission of Er-doped  $\text{MoS}_2$  thin film.

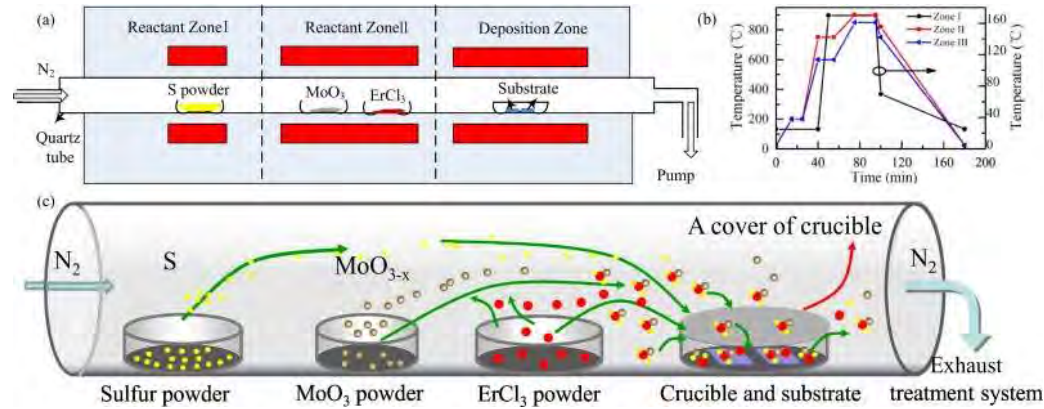


Figure 1.12 a) Experimental setup of quasi-closed crucible CVD system. b) Temperature profile of Er-doped MoS<sub>2</sub> film growth. c) A schematic of the synthesis process.

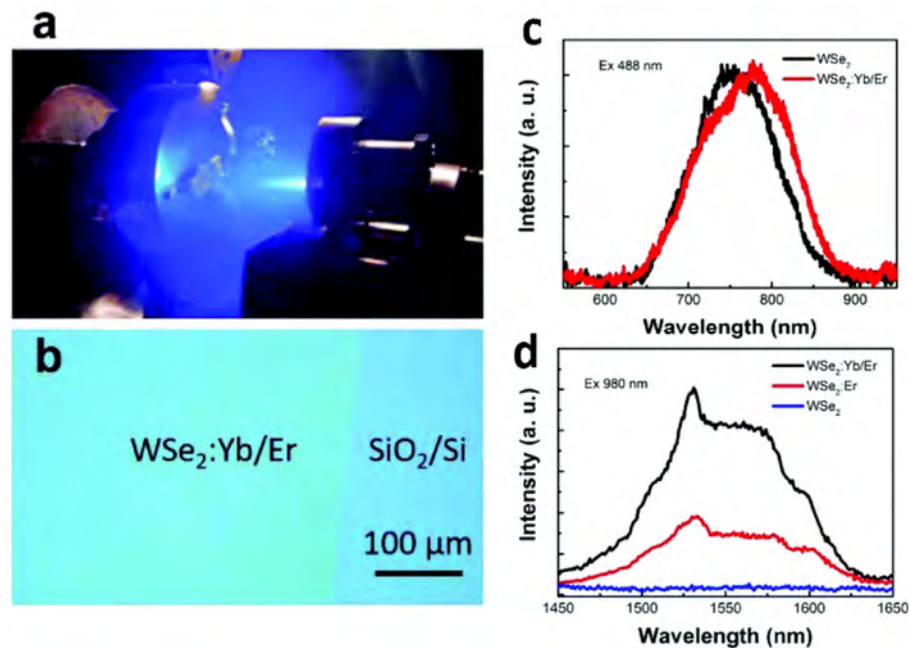


Figure 1.13 a) Preparation of Yb/Er co-doped WSe<sub>2</sub> thin film by PLD. b) optical image of Yb/Er doped WSe<sub>2</sub>. Scale bar, 100 μm. PL spectrum of Yb/Er doped WSe<sub>2</sub> at c) 800 and d) 1550 nm.

## 1.4 Background on atomistic modeling and simulation

Scientific modeling and simulations have been used long to understand complex physical phenomena. In recent years, the rapid advance of computational power renders the emergence of new theoretical and numerical methods to better analyze the physical system.<sup>20</sup> Depending on the view point of scale, a material can be a continuum medium, structural element, mesoscale particles, atoms, or a collection of electrons and nucleus. The choice of simulation method relies on the compromise between the simulation scale and the desired accuracy as presented in Figure 1.14.<sup>2</sup> The combination of multi-scale modeling of computational materials also provides us more possibilities to predict failures in material engineering.

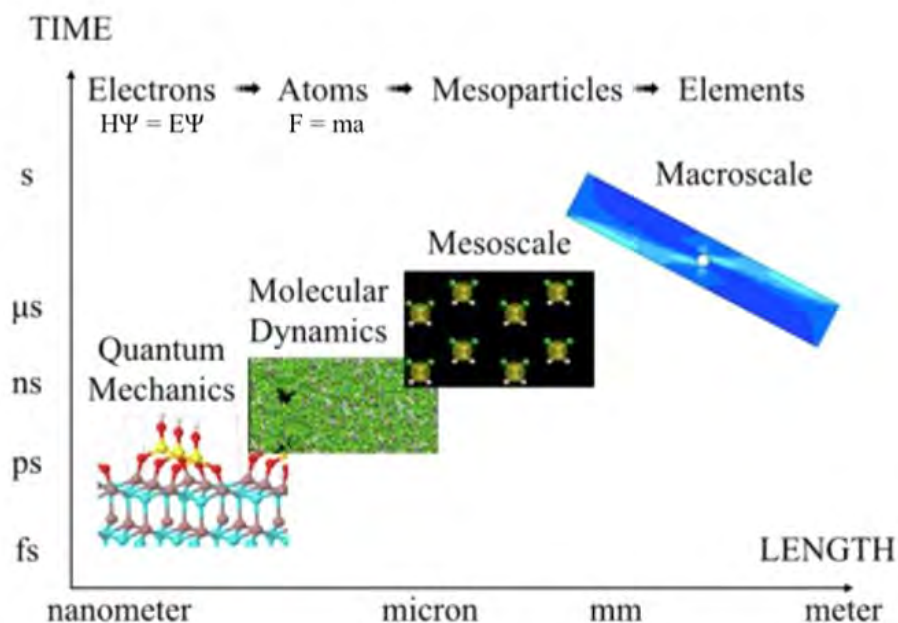


Figure 1.14 Multi-scale view of computational materials.

The modeling and simulation method can be divided into three categories regarding the length scale: “continuum”, “molecular” and “quantum” mechanical methods. The “continuum” modeling approach mainly deals with the infinitely

divisible matters with no internal structures.<sup>66</sup> As an example, the finite elements method (FEM) can be utilized to approximate the analytical solutions for problems in macroscale structural engineering such as structural analysis, fluid flow and heat transfer.<sup>35,65</sup> In a smaller length scale, the “molecular” modeling resolves ultrathin structural engineering in molecules and atoms level.<sup>10</sup> The molecular dynamics enable simulations of millions of atoms with up to microsecond timescale. The empirical representation is used to calculate the interaction between atoms described by a set of simple equations, which depend on the atomic coordinates and interatomic separation.<sup>42,62</sup> The parameters in those functions need to be tuned to appropriate values by minimizing stress and force on the computed structures, or the incorporation of the experimental data. Besides, the incorporation of atomistic models in macroscale simulations is of vital importance since the atomic simulation provides fundamental perspectives and therefore a mean to predict important parameters to be used in continuum models. The “quantum” mechanical method (also called first principle or *ab initio* calculation) explicitly resolves electrons in the fundamental view of chemical bonding.<sup>84</sup> It allows us to perform reliable numerical simulations without parameters tuning by dealing with the electronic wavefunction in Schrodinger equation.<sup>1,43</sup> Depending on different levels of theory, the quantum mechanical method consists of the Hartree-Fock methods, post Hartree-Fock methods and density functional theory (DFT) methods.

## 1.5 Significance of research

Atomically thin semiconductors have attracted remarkable interest in the area of theoretical physics and material science owing to their fascinating properties emerged at 2D limit. Much research effort has been demonstrated on the modulation and

functionalization of their intrinsic properties to satisfy the growing demand of the community. Due to the presence of a relatively narrow bandgap, the primary luminescence of 2D TMDs is limited from visible to the edge of NIR spectral range, which hinders a wide variety of attractive applications such as light emitting devices. So far, the tuning of bandgap emission of 2D TMDs is restricted by controlling the layer number, excitons and applying external strain. Therefore, it is crucial to find an effective approach to the precisely modulate and extend the luminescence of 2D TMDs. In particular, the ability of lanthanide ions to induce luminescence features has long been utilized in traditional semiconducting hosts by introducing extra energy levels into their bandgap.<sup>18,70</sup> The introduce of lanthanides into the new family of 2D TMDs semiconductor is promising for functionalize their emission properties. A striking example is the NIR emission on large scale MoS<sub>2</sub> film incorporated with Er dopants demonstrated by our group. The observation of down-conversion at 1550 nm is vital for optical fiber communication and photonic electronics as it matches well with the minimum loss window of silica optical fiber. After that, the Yb/Er co-doped WSe<sub>2</sub> film was fabricated by PLD approach, with a further enhanced NIR luminescence contributing to the large absorption cross-section of Yb dopant.

Based on our previous works on the luminescence properties of lanthanide ions in 2D semiconducting materials, the NIR emission from Er<sup>3+</sup> ions have been successfully demonstrated in both MoS<sub>2</sub> and WSe<sub>2</sub> host matrix. However, only polycrystalline ultra-thin films with unpredictable defects was obtained, which limits further study of the doped semiconductor system and optoelectronic device fabrication. Further optimization of growing conditions and parameters is necessary for improvement of crystal quality and homogeneity. Besides, many intriguing luminescence features of the obtained material, such as concentration quenching effect,

still await further investigation. In the aspects of theoretical modeling and simulations, various transition metal dopant species on 2D semiconductor system have been demonstrated. However, the development on the simulation of lanthanide element doped TMDs is still in their early stage. The mechanism of the interaction of lanthanide impurity states and the host bandgap is still unclear. Hence, it is intriguing to put effort in both experimental and theoretical investigations of lanthanide doped 2D TMDs.

## 1.6 Thesis overview

The thesis chapters are organized as follows:

**Chapter 1:** Introduction. In this chapter, the physical properties and applications of layered semiconducting materials, especially 2D TMDs, are first introduced. Then, the doping of 2D materials including doping principle, potential dopant species, doping strategies and applications are illustrated briefly. Following that, the luminescence of lanthanide elements and their application into 2D materials was introduced. Then, some background knowledge on materials modeling and simulation are presented. At last, the significance of this research is presented to clarify the motivation and objective of this thesis, and the framework of this thesis is described as a guidance for reading.

**Chapter 2:** Experimental techniques and theoretical analysis. This chapter first introduces the synthesize techniques employed to prepare the 2D layered materials in this work. After that, the equipment used for characterization of prepared samples are presented, including structural characterization and optical properties measurements. Lastly, the computational simulation details using density functional theory are described.

**Chapter 3:** Synthesize and characterization of pristine MoS<sub>2</sub> nanosheets. This chapter demonstrated the growth of 2D MoS<sub>2</sub> layers using molten-salt-assisted CVD method and two-step metal-precursor-based deposition method, respectively. The growing mechanism, structural and chemical composition characterization was investigated.

**Chapter 4:** Near infrared luminescence of Er-doped MoS<sub>2</sub> monolayer. In this chapter, Er-doped MoS<sub>2</sub> monolayer was prepared by the two-step deposition method. The comparison of structural, chemical composition, Raman, PL properties are demonstrated on doped and pristine MoS<sub>2</sub> monolayers. Finally, the NIR luminescence properties and energy transfer mechanism of Er<sup>3+</sup> dopant is investigated.

**Chapter 5:** Density functional theory calculation of Er-doped MoS<sub>2</sub> monolayer. This chapter demonstrates the theoretical calculations of the structural properties and energetics of pristine and Er-doped MoS<sub>2</sub> monolayer, as well as their electronic properties. The energy level diagram of Er-doped MoS<sub>2</sub> are predicted.

**Chapter 6:** Conclusion and future prospect. The results in this thesis are summarized in this chapter. Potential future works of NIR luminescence of 2D layered semiconductor are suggested.

## Chapter 2

# Experimental Techniques and Theoretical Analysis

This chapter demonstrates the techniques employed in this research including experimental and theoretical analysis. 2D MoS<sub>2</sub> nanosheets were prepared using magnetron sputtering and chemical vapor deposition (CVD). The structure and chemical compositions of the fabricated samples were characterized by X-ray diffraction (XRD), atomic force microscopy (AFM) and Energy dispersive X-ray spectroscopy (EDS). The optical properties were studied using Raman spectroscopy and steady-state photoluminescence (PL) spectroscopy. The electronic structure and energy levels were simulated by first principle calculations using the Quantum Espresso (QE) package.

### 2.1 Sample preparation

#### 2.1.1 Magnetron sputtering

Magnetron sputtering is a physical vapor deposition (PVD) approach for deposition of thin film using a sputtering “target” as source material.<sup>37</sup> Conductive materials can be sputtered by using direct current (DC) power supply and insulating

materials can be sputtered by radio frequency (RF) power supply. A schematic of the working principle of the magnetron sputtering system is depicted in Figure 2.1.

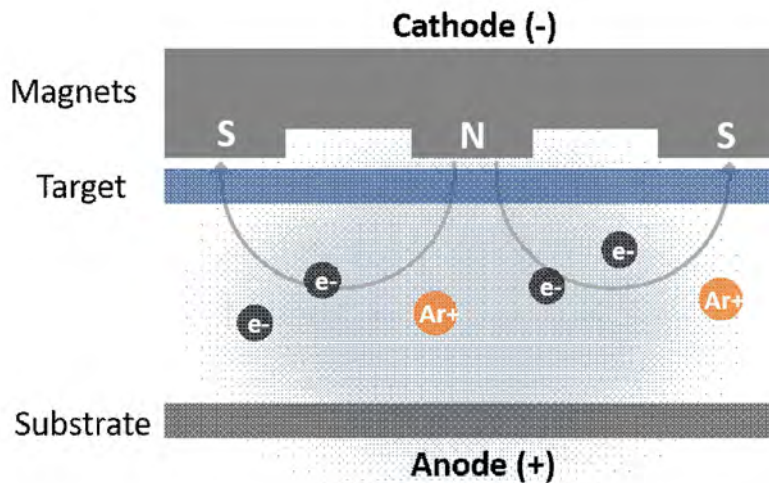


Figure 2.1 Schematic illustration of magnetron sputtering system.

In front of the sputtering target, free electrons are trapped and forced into helical shape around the magnetic lines due to the employment of permanent magnets behind the target. The sputtering process are typically conducted in Argon inert gas atmosphere under low process pressure where the argon atoms can be ionized by those free electrons. The positively charged argon ions generated in the form of a plasma are then accelerated by the electrical potential superimposed on the negatively charged sputtering target. Subsequently, the sputtered material will be continuously ejected from the target by bombardment of Argon ions and deposited on the substrate surface to form dense layers. The presence of a closed magnetic field allows a lower pressure to generate the plasma, which can minimize both energy loss through background gas collisions and gas incorporation in the deposited film.

A schematic of the setup of the magnetron sputtering system used in this thesis is presented in Figure 2.2. The system is designed for sputtering of metallic materials

with a direct current (DC) configuration equipped with three cathodes, allowing for the co-sputtering of different metals. In a typical sputtering process, the high-vacuum chamber is first evacuated to a base pressure of  $10^{-5}$  Torr using a turbo pump assisting with a mechanical pump connected in series. The deposition involves Argon ions as sputtering gas flowing in a rate of 20 sccm while the total vacuum level is regulated to  $\sim 16$  mTorr by controlling the vacuum valve.



Figure 2.2 Setup of the magnetron sputtering system.

### 2.1.2 Chemical vapor deposition

Chemical vapor deposition (CVD) is a widely used deposition method to grow high-quality solid materials on substrate surfaces.<sup>17</sup> Its majority application in the semiconductor industry involves coating of thin films, and also production of high-quality bulk crystals and powders.<sup>46</sup> In the two-dimensional (2D) materials field, CVD is the most common approach to produce atomically thin materials with high crystallinity and scale-up capability. In a typical CVD process, substrates are exposed to the related precursor materials, which will react in atmosphere of protection gas to

produce the desired deposit on the substrate surface. One or more heating zones can be adopted to satisfy the evaporation or decomposition conditions of different precursors, and the desire deposition temperature on the substrate surface.



Figure 2.3 Schematic diagram of the homemade CVD system.

The chemical vapor deposition system used for crystal growth in this thesis is captured in Figure 2.3. To minimize the temperature disturbance between the adjacent heating zones of typical commercial multi-zone furnaces, a homemade two-zone apparatus was used to perform the CVD experiments. The major parts of the reactor system consist of two tubular furnaces controlled by individual temperature controllers to achieve the desired growing temperature profile. Heating zone I is for chalcogenide source supply, while heating zone II is for metal precursor supply and deposition on substrate. A digital mass flow controller is connected to the upstream end of the quartz tube to control the flux of carrier gas. A three-way control valve is used to switch between Ar and Ar/H<sub>2</sub> carrier gas supplied to the reactor. The pressure in the reactor is controlled and monitored by the vacuum pump and gas-pressure meter. The

deposition was conducted in a quartz tube with a diameter of 25 mm and a length of 100 mm. Quartz boats with the volume of 100x17x10 mm are used to place the precursors.

## 2.2 Structural characterizations

### 2.2.1 X-ray diffraction

X-ray diffraction (XRD) is a powerful non-destructive technique used for studying the structural properties of crystalline materials in an atomic and molecular scale. It provides crystal structure, orientation, phase and other structural analysis such as crystallinity, crystal defects, average particle size and tension.

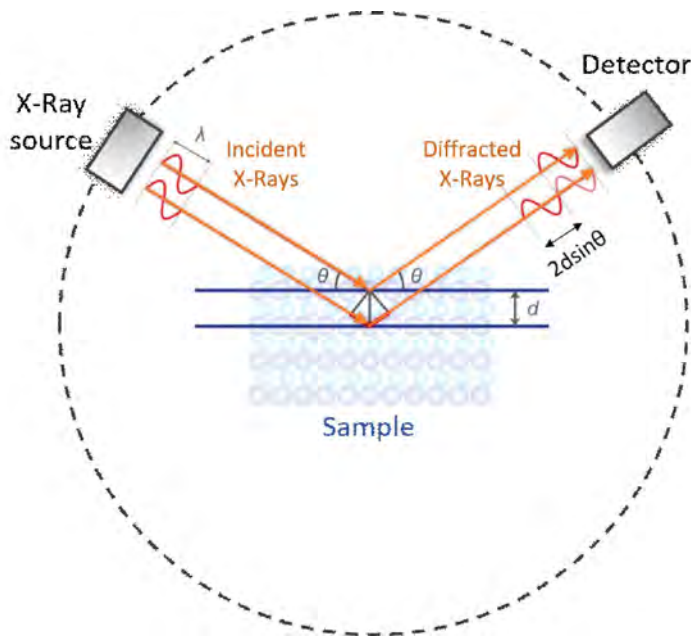


Figure 2.4 Basic X-ray diffractometer setup.

A schematic of the fundamental working principle of X-ray diffractometer is illustrated in Figure 2.4, in which the constructed interference of the incident X-ray by crystal lattice planes are depicted. The incoming monochromatic beam from the X-ray tube is incident on the sample surface with a lattice plane spacing of  $d$ . The waves

scattered by lattice planes of the crystalline sample will superpose constructively when the incident angle  $\theta$  meet the criterion of the Bragg's law:<sup>38</sup>

$$2d \sin \theta = n\lambda \quad (2.1)$$

In those specific directions that the path difference between the scattered X-rays equals to an integral number  $n$  of the wavelength  $\lambda$ , a small portion of the X-ray beam will interfere with each other to produce a diffraction maximum. By comparing the recorded diffraction patterns with standard line patterns, the information on crystal structure, phases, crystal orientations can be determined. In our experiment, the lattice structure of prepared sample was acquired by high resolution X-ray diffractometer (Rigaku, SmartLab 9kW).

### 2.2.2 Atomic force microscopy

Atomic force microscopy (AFM) is a powerful scanning probe technique to study material properties including morphology, surface roughness, size and texture at an atomic resolution. As is demonstrated in Figure 2.5, an AFM system operates by probing the specimen surface using a specially designed sharp tip mounted at the free end of a microscale cantilever.<sup>44</sup> The XYZ scanner with three-axis displacement allows for the probe to scan in lateral directions on sample surface. The vertical distance between the probe and sample surface is controlled by beam deflection technology. The beam generated by the laser diode is focused on back of the probe tip and reflected to a photodiode where the voltage signal is generated by the amplifier circuit. By processing the voltage signal, the z-axis displacement is controlled by the feedback circuit. The vertical displacement and lateral positions are then transmitted

to the computer control system, where the topographical structure of the surface is mapped and recorded.

The AFM operating modes can be divided into three types: contact mode, tapping mode and non-contact mode. In the present work, contact mode has been utilized since it mainly takes advantage of the repulsive force between atoms which is super sensitive to distance, rendering a higher capability of obtaining atomic scale resolution compared with the other modes. In our experiment, Asylum MFP 3D Infinity system was employed to investigate the morphology of prepared samples.

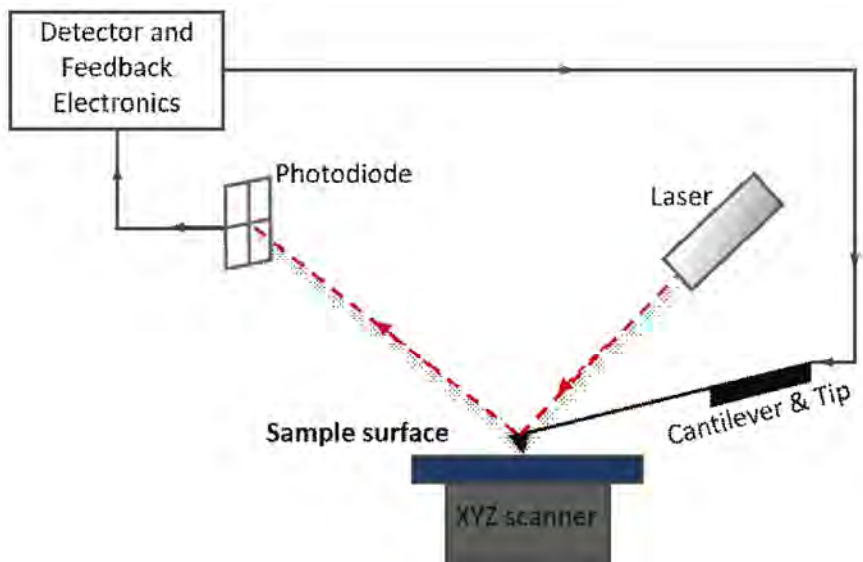


Figure 2.5 Block diagram of atomic force microscopy.

### 2.2.3 Energy dispersive X-ray spectroscopy

Energy dispersive X-ray spectroscopy (EDS) is a powerful analytical technique used for analysis of chemical and elemental composition of a sample. The mechanism of an EDS system is based on interaction between the specimen and the stimulation source for X-ray excitation as depicted in Figure 2.6.<sup>30</sup> The incident stimulation strikes on the sample surface where electrons are initially sitting at their

ground state in discrete energy levels. The external stimulation may excite and eject an electron from the inner shell, leaving behind an electron hole in this energy level. A high energy electron from outer shell tends to fill up the generated electron hole to stabilize the atomic structure. A photon is released simultaneously in the form of X-ray as a compensation for the difference in energy between these two shells. The measured position and intensity of X-ray emission lines are characteristic properties of an element since they depend on the unique atomic structure of individual species.

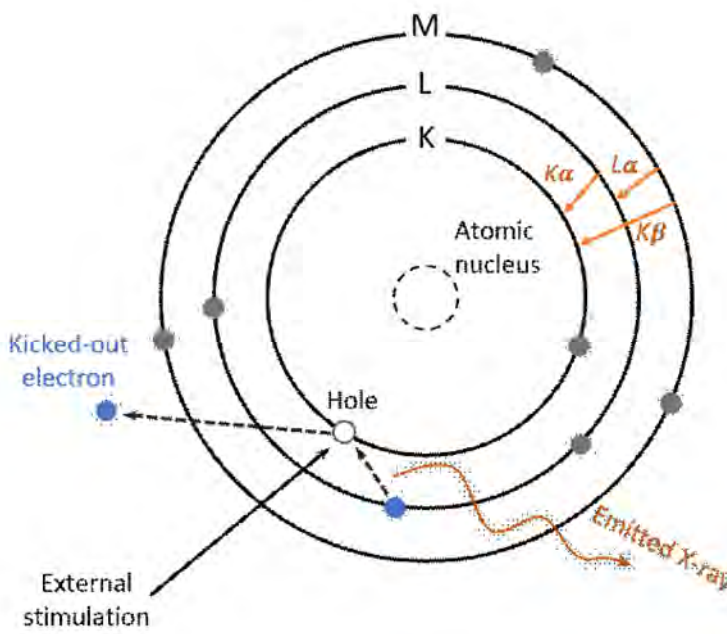


Figure 2.6 Schematic principle of energy dispersive X-ray spectroscopy.

In practical, the external stimulation source typically involves high energy X-ray beam or focused beam of charged particles such as protons or electrons. In our experiment, high energy electron beam implemented in TESCAN VEGA3 scanning electron microscopy (SEM) instrumentation is employed to visualize the surface elemental composition at individual points.

## 2.3 Optical properties measurements

---

### 2.3.1 Raman spectroscopy

Raman spectroscopy is a non-destructive spectroscopy analytical technique used to characterize molecular structure by identifying their vibration modes. Figure 2.7 depicts the basic principle of three types of scattered radiations in relationship with energy states of a target sample.<sup>94</sup>

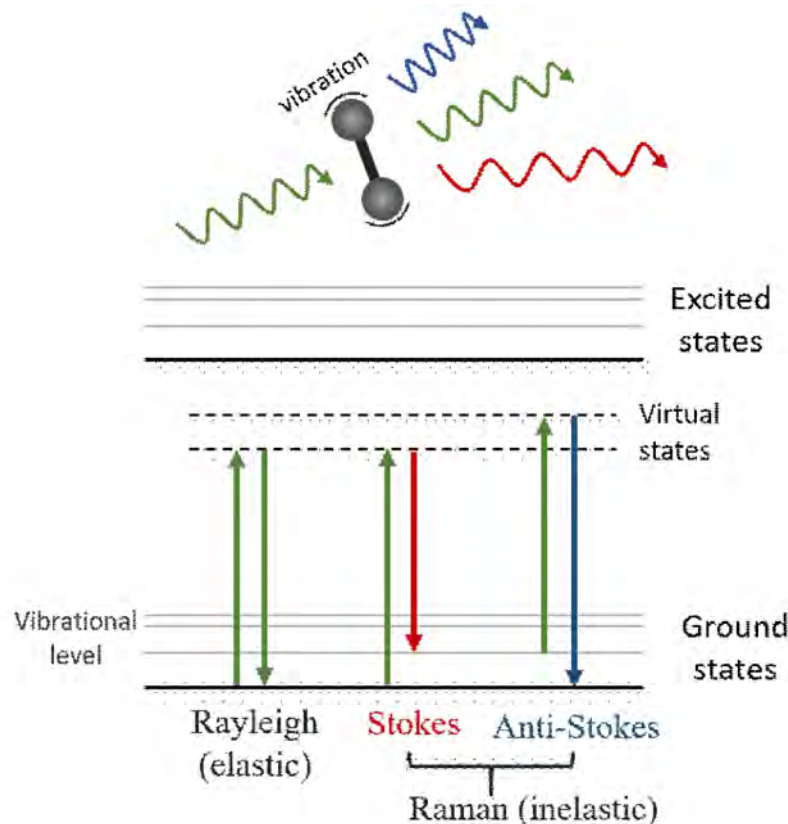


Figure 2.7 Fundamental principles of Raman and Rayleigh scattering.

Under the illumination of high intensity laser source, molecules resting at their ground state will be excited to a virtual energy state for a short period through photon energy absorption and emission.<sup>60</sup> The laser source interacts with the chemical bonds of the target material, resulting in scattered light with different wavelengths. Most of light is scattered at the same wavelength as the incident light, which is called Rayleigh

elastic scattering. On the contrary, a small portion of the scattered light is at different wavelength with the incident light, leaving the sample in different vibrational states after scattering. This is known as the Raman inelastic scattering, which provides information on the structural fingerprint of the characterized molecular. Depending on the initial and final states of the molecular, Raman scattering can be further divided into Stokes scattering and anti-Stokes scattering. Raman measurement is typically based on the Stokes shift owing to its higher chance of occurrence than anti-Stoke shift. The shift in energy contains the unique chemical fingerprint of a particular material, making it a powerful tool for identification of chemical structure and phase.

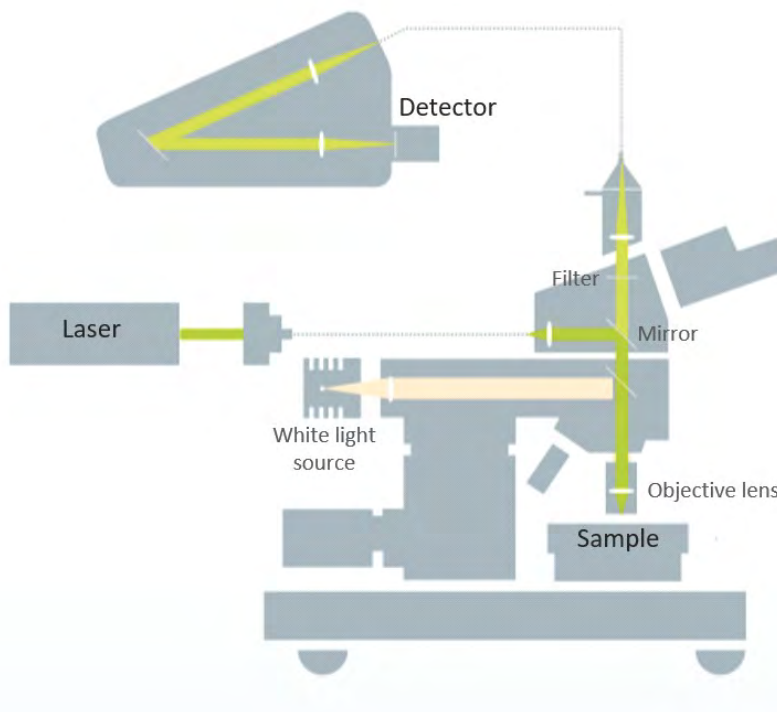


Figure 2.8 Schematic illustration of the confocal Raman system. Reprinted from WITec Raman imaging website.

In our experiment, a high-resolution confocal Raman system (Witec, Alpha300 R) equipped with 532 nm laser excitation has been employed to investigate the crystal

structure of prepared nanosheets. The Raman system is capable of automated large-area mapping on specific positions of sample surface by incorporating a motorized scanning stage. As shown in Figure 2.8, a continuous excitation laser is directed onto sample surface by a series of optical fibers and reflective mirrors. To separate the Raman scattered radiation from the reflected laser signal and elastically scattered Ryleigh signal, the scattered light then passes through a filter before being dispersed onto a highly sensitive charge-coupled-devices (CCD) detector.

### 2.3.2 Steady-state photoluminescence spectroscopy

Photoluminescence (PL) spectroscopy is a non-destructive, non-contact technique used to probe the emission characteristics of any form of materials. When light is illuminated on a sample, electrons in their ground state jump to higher energy levels by absorbing energy from the incident photons. Subsequently, the photo-excited electrons relax to their initial states and release energy in the form of emitted photons. The steady-state PL spectra is recorded by monitoring the distribution of emitted photons as a function of either emission or excitation wavelength. An emission spectrum is obtained by measuring the emission over a desired spectra range using a fixed excitation wavelength. In an excitation spectrum, the emitted radiation at a fixed emission wavelength is monitored while varying the wavelength of excitation light source.

The NIR emission behaviors of our as-prepared two-dimensional nanosheets are recorded by the Edinburgh FLS920 photoluminescence spectrometer as shown in Figure 2.9. Our instrumentation has been configured for a wide range of steady-state PL spectrum measurement from the deep ultraviolet (UV) to the mid-infrared (MIR) with single photon counting technique. The system has been configured into a T-

geometry as presented in Figure 2.10, allowing for the installation of several detectors with software-based selection simultaneously.



Figure 2.9 Photography of the PL spectrometer in our laboratory.

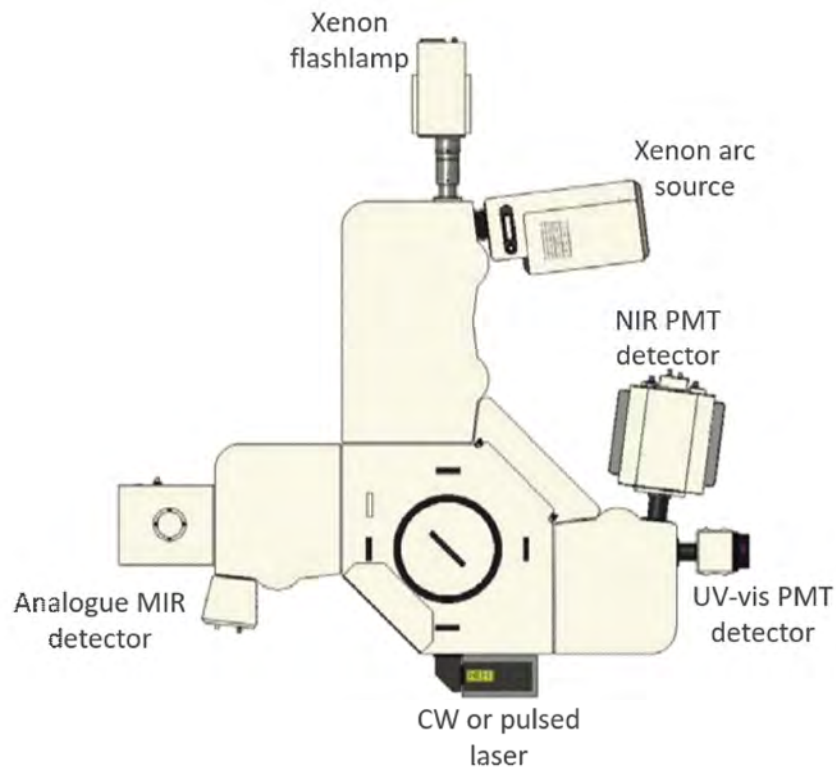


Figure 2.10 Equipment configuration of the FLS900 spectrometer. Reprinted from Edinburgh Instruments Webpage.

The computer-controlled mirrors mounted in the chamber renders rapid selection of excitation and emission paths. The NIR photomultiplier (PMT) detector operating at -80°C covers the wavelength range from 300 to 1700 nm, while the red sensitive PMT detector can respond the photons in the range from 200 to 870 nm at -20°C. The analogue MIR detector mounted at the left emission arm enables photon counting operation up to 5.5  $\mu\text{m}$ . Apart from the pre-equipped Xenon arc lamp which emits tunable radiation from 230 to more than 1000 nm as continuous excitation source, external lasers can be mounted to the input port on the side of the sample chamber in demand of larger excitation power. In our experiment, a high-power diode laser with continuous excitation at 980 nm is mainly used to measure the NIR PL spectrum.

## 2.4 Density functional theory calculations

### 2.4.1 Basic principles of density functional theory

The core of the density functional theory simulation consists of a set of programs, namely the PWscf (Plane-Wave Self-Consistent Field) package. It is basically within the density functional theory (DFT), using the plane waves (PW) basis sets and pseudopotentials to solve the many-body Schrodinger equation:<sup>26</sup>

$$\hat{H}\Psi(r_1, \dots, r_N) = E\Psi(r_1, \dots, r_N) \quad (2.2)$$

where the Hamiltonian working on the many-body wave function equates the energy of the system:

$$\hat{H} = -\frac{1}{2} \sum_i \Delta_i + \sum_i V(r_i) + \sum_{i \neq j} \frac{1}{|r_i - r_j|} \quad (2.3)$$

Basically, the DFT solves this equation by simplifying this many-body wavefunction based on “one-electron” theory, which cast the wavefunction that depends on all the spatial coordinates of the electrons into a group of functions depending on only one electronic coordinate:<sup>71</sup>

$$\Psi(r_1, \dots, r_N) \rightarrow \{\psi_1(r), \psi_2(r), \dots, \psi_N(r)\} \quad (2.4)$$

### 2.4.2 Quantum ESPRESSO

All the structural and electrical properties in this thesis are simulated by Quantum ESPRESSO (QE) package running on the pilot high performance computing (HPC) platform. The QE package is an integrated suite of ab-initio quantum chemistry method for materials modeling and electronic-structure calculations at the nanoscale. It is an Open-Source computer codes distributed by the CNR-IOM DEMOCRITOS National Simulation Center in Trieste of Italy in collaboration with research centers worldwide. The main program of the software is structured for parallelization to run efficiently on HPC hardware.

Approximations on the exchange correlation functionals are modeled with the assumption of uniform electron gas (UEG). The QE package offers a wide range of choices on the exchange correlation functionals, including local density approximation (LDA), generalized gradient approximation (GGA), van-der-Waals functionals and hybrid functionals (B3LYP, PBE0, HSE), etc. All the cell-periodic quantities of the functions are expended in terms of plane waves by Fourier analysis, rendering the efficient transformation between the quantities in real space and reciprocal space. The

basis set includes all the plane waves with kinetic energy below a certain cutoff energy to be set up considering the potentials used in the system. To restrict the number of plane waves used to describe the orbitals, another approximation is made by introduction of the frozen core approximation, or pseudopotentials instead of exact potentials. The type of pseudopotentials implemented in the QE code includes the Norm-conserving pseudopotentials, Ultra-soft pseudopotentials and the Projector Augmented-Wave (PAW) method. Different tasks can be performed by QE including ground state calculations, structural optimization, transition states and minimum energy paths, molecular dynamics, spectroscopic, etc.

# Chapter 3

## Synthesize and Characterization of Pristine MoS<sub>2</sub> Nanosheets

### 3.1 Introduction

Among the two-dimensional (2D) transition metal chalcogenides (TMDs) family, monolayer molybdenum disulfide (MoS<sub>2</sub>) is the most investigated member for its excellent mechanical flexibility, chemical stability and attractive electronic attributes.<sup>98,109</sup> Unlike graphene, atomically thin MoS<sub>2</sub> is a semiconductor material with a tunable bandgap varying with layer number. The bandgap becomes direct ( $E_g \sim 1.8\text{eV}$ ) when the thickness is reduced to single layer limit, making monolayer MoS<sub>2</sub> one of the most promising candidates for optoelectronic and light emitting devices such as photovoltaics, photodetectors and light emitting diodes.<sup>85,93</sup> Moreover, monolayer MoS<sub>2</sub> is extremely attractive to construct next-generation electronic devices since the sheet resistance can be significantly tuned by incident light or applied gate voltage.<sup>113</sup>

Based on these impressive optical and electronic characteristics, there has been growing demand for integration of 2D MoS<sub>2</sub> into existing optoelectronic platforms. Therefore, scalable preparation of high-quality monolayer MoS<sub>2</sub> sample is of vital

importance. So far, the synthesize of atomically thin MoS<sub>2</sub> has been realized by various methods, including mechanical exfoliation, vapor phase deposition, solution-based reactions, etc. Among the fabrication techniques, chemical vapor deposition (CVD) technique shows promising aspects to yield wafer-scale MoS<sub>2</sub> layers with controllable thickness and uniform electronic responses.<sup>69,96</sup> Growth of MoS<sub>2</sub> sheets has been demonstrated by vapor phase reaction of metal oxide with sulfur, sulfurization of pre-deposited Mo precursors (such as metal or metal oxide film), chemical vapor transport and recrystallization of MoS<sub>2</sub> powder, and thermal decomposition of ammonium thiomolybdate (NH<sub>4</sub>)<sub>2</sub>MoS<sub>4</sub>.<sup>33,51,52</sup> This chapter presents the deposition of MoS<sub>2</sub> monolayer by two methods: molten-salt-assisted CVD method and two-step metal-precursor based deposition method.

## 3.2 Molten-salt-assisted CVD growth of monolayer MoS<sub>2</sub>

Among the numerous fabrication techniques available, CVD method has been the most promising one for the controlled synthesize of 2D TMDs. The high melting point of their metal or metal oxide precursors, however, makes it hard difficult to produce high quality, uniform nanosheets for potential applications. Molten-salt-assisted method has been employed to facilitate the growth of ceramic powders at relatively low temperature, and recently this technique was applied for the production of a wide variety of atomically thin TMDs. In this section, the deposition of large area MoS<sub>2</sub> monolayer was demonstrated using the molten-salt-assisted CVD method.

### 3.2.1 Experimental details

The molten salt is incorporated into the growth system by mixing up with the metal precursor. A powder mixture of MoO<sub>3</sub> and NaCl with a mass ratio of 2:1 was

finely grinded first. A schematic diagram of the experimental setup and the growth temperature profile are presented in Figure 3.1 and Figure 3.2, respectively. Note that the growth conditions (e.g. temperature, growth duration, precursor ratio) have been attempted and optimized to yield high-quality MoS<sub>2</sub> sample, and the finalized experimental parameters are presented here as an example. As depicted in Figure 3.1, high purity sulfur powder was placed in a quartz boat heating at 150°C (heating zone I), which is slightly above the melting point of sulfur power. Another quartz boat containing the MoO<sub>3</sub> precursor powder and the growing substrate were placed at the downstream at 750°C (heating zone II). The distance between the source and substrate was typically around 1 cm. The growth temperature of each heating zone was held at their respective target temperature for 10 minutes for the deposition of MoS<sub>2</sub> single crystals. Prior to crystal growth, the quartz tube was vacuumed below 6 Pa and then flushed with carrier gas until atmospheric pressure to prevent any possible oxidation pollution by evacuating the residue air. In the subsequent growing process, the pressure in the tube was kept at one atmosphere pressure, and Ar/H<sub>2</sub> was kept flowing at a rate of 60 sccm during the whole process. After the crystal growth, the furnaces were allowed to naturally cool down to room temperature.

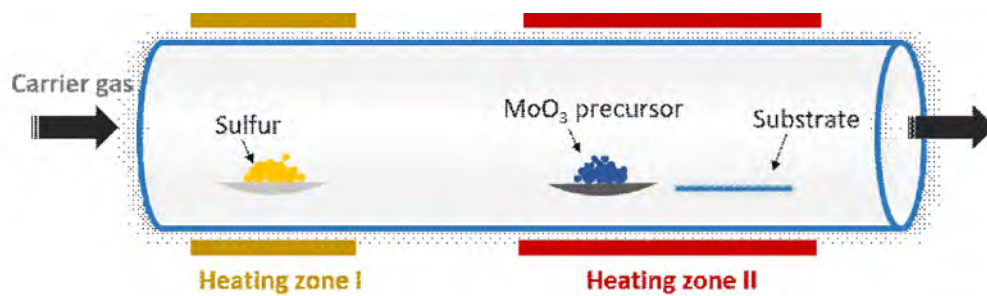


Figure 3.1 CVD setup for the growth of MoS<sub>2</sub> single crystal.

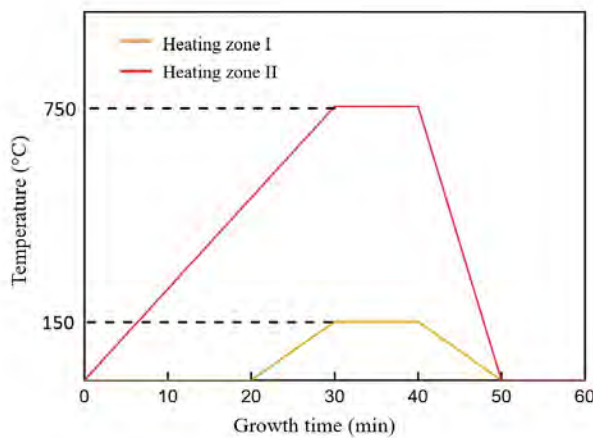


Figure 3.2 Growing temperature profile of the deposition process.

### 3.2.2 Key parameters

#### a. Temperature

By fine control and proper optimization of the growth parameters, such as the weight and distance of precursors, reaction temperature and growth duration, etc., highly crystalline MoS<sub>2</sub> nanosheets were obtained over a broad temperature range. Figure 3.3 exhibits optical images of the as-grown MoS<sub>2</sub> flakes obtained under different temperatures (650-800°C) with a growth duration of 10 min. Significant variations in lateral dimension of MoS<sub>2</sub> grains can be observed at different temperatures. At growth temperature of ~650°C, the sublimation rate of MoO<sub>3</sub> precursor is relatively low, which limits the production of active mobile species over the substrate. Therefore, the obtained MoS<sub>2</sub> grains exhibit small sizes of less than 10 μm and high domain density. As the growth temperature increases, the generation and diffusion of active species on grown substrate are promoted significantly, thereby resulting in larger grain sizes and lower nucleation density. As shown in Figure 3.3c, the largest MoS<sub>2</sub> grain (~150 μm) is observed at growth temperature of 750°C. When

the growth temperature is further increased to 800°C, however, the lateral dimensions of grains begin to shrink considerably (see Figure 3.3d). This may be contributed to less adsorption amount of sulfurized MoO<sub>3</sub> precursors on bare substrate and the decreased rate of grain growth under high temperature.

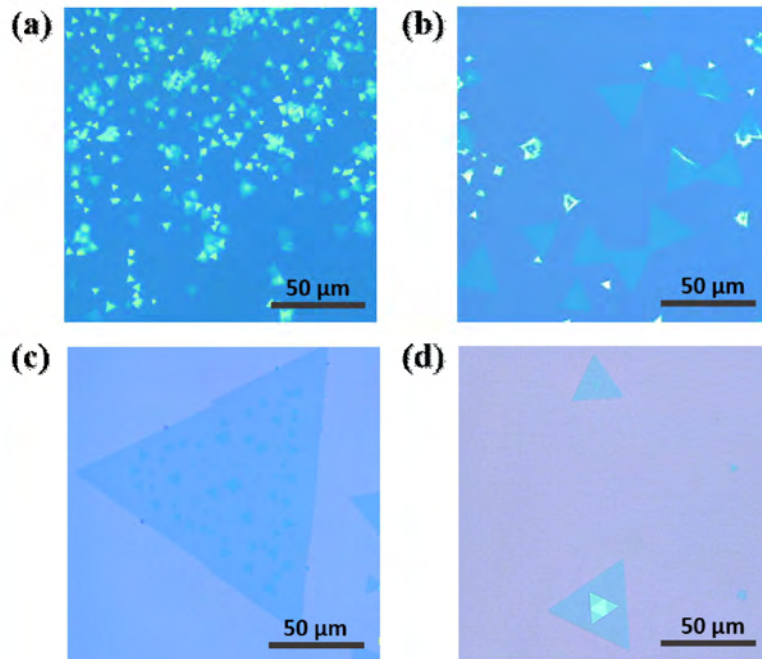


Figure 3.3 Optical image of MoS<sub>2</sub> flakes obtained under different reaction temperatures: a) 650°C, b) 700°C, c) 750°C, and d) 800°C. Scale bars, 50 μm.

#### b. Growth duration

To investigate the morphology evolution of MoS<sub>2</sub> grains with different growth duration, the growth temperature and MoO<sub>3</sub> precursor amount was kept constant at 750°C and 10 mg, respectively. As presented in Figure 3.4, when the growth time varies from 5 min to 10 min, the individual MoS<sub>2</sub> flakes are enlarged preferentially. As the growth duration further increase, single MoS<sub>2</sub> domains start to merge together and eventually form a continuous film.

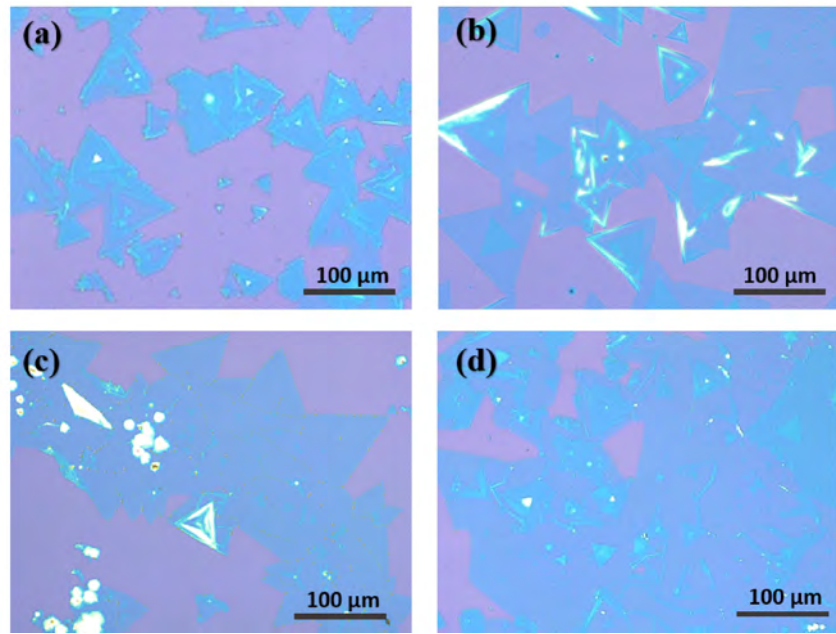


Figure 3.4 Optical image of MoS<sub>2</sub> samples prepared at 750°C under different growth times: a) 5 min, b) 10 min, c) 15 min, and d) 20 min. Scale bars, 100  $\mu\text{m}$ .

### c. MoO<sub>3</sub> precursor amount

Apart from growth temperature and duration, the S to MoO<sub>3</sub> ratio is another critical factor determining the morphology and quality of MoS<sub>2</sub> grains. To investigate the interaction between MoO<sub>3</sub> precursor and sulfur vapor, we varied the S to MoO<sub>3</sub> ratio by adjusting the MoO<sub>3</sub> precursor weight based on the assumption of a constant sulfur vapor concentration. Other parameters were kept constant at the optimized growth condition, with growth temperature of 750 °C and growth duration of 10 min. The optical images of obtained MoS<sub>2</sub> samples are exhibited in Figure 3.5. Under insufficient supply of MoO<sub>3</sub> precursor, which corresponds to high S to MoO<sub>3</sub> ratio, the MoS<sub>2</sub> flakes exhibit circular shape and atomic clusters are often observed at the grain center (see Figure 3.5a). In this condition, low mass flux of metal precursor and low growth rate promote the merge of small flakes into circular grains. As the MoO<sub>3</sub> weight

is increased from 2 mg to 10 mg, the morphology of MoS<sub>2</sub> grains are gradually varied from circular to triangular shape. Notably, when the MoO<sub>3</sub> weight is further increased to 20 mg, multi-layered flakes of star shape start to appear (see Figure 3.5d). The formation of MoS<sub>2</sub> multilayer suggests that higher mass flux of metal precursor contributes to the capture of more Mo source at the edge and center of the flakes.

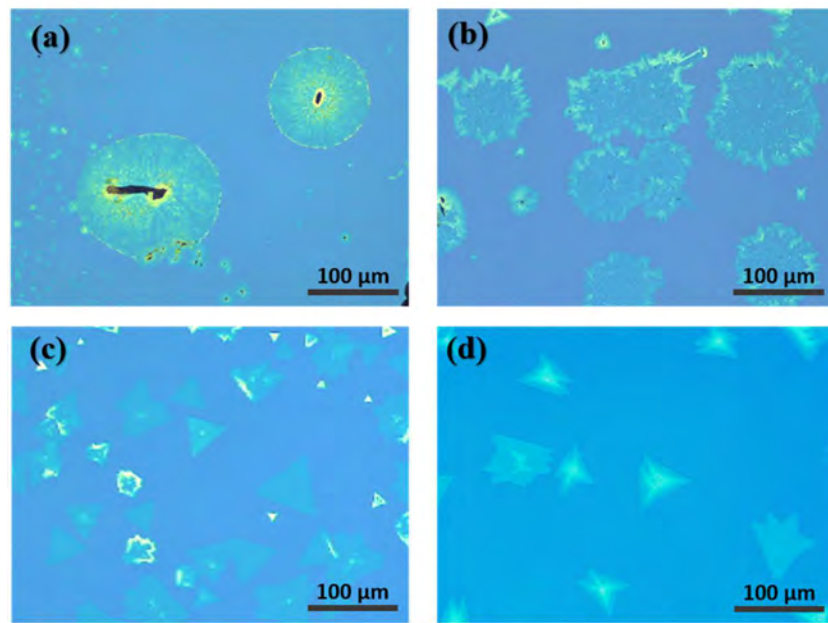
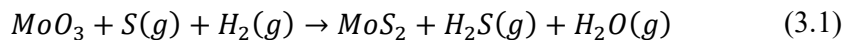


Figure 3.5 Optical image of the MoS<sub>2</sub> flakes obtained at 750°C with different MoO<sub>3</sub> precursor amount: a) 2 mg, b) 5 mg, c) 10 mg, and d) 20 mg. Scale bars, 100  $\mu\text{m}$ .

Based on the above discussions, the morphology evolution is an indication of the difference in S to MoO<sub>3</sub> ratio distributed over the grown substrate, which is in line with previous investigations. However, the overall growth environment is interrelated with each growth parameter, and the change of one experimental parameter may affect more than one factor. Other neglected factors, such as local pressure distribution over the grown substrate and dynamic gas flow, may also attribute to the shape evolution and nucleation density of the flakes.

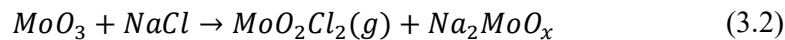
### 3.2.3 Reaction mechanism

To gain an in-depth understanding of the role of molten salt in the growing process, the thermal dynamics kinetics aspects in the reaction and growth of MoS<sub>2</sub> layers will be discussed in this subsection. The growth of MoS<sub>2</sub> relies on the reaction between the metal and chalcogen precursors, which are supplied by heating the precursor powders during the deposition process. From many previous works on synthesize of MoS<sub>2</sub> by regular CVD without the assistant of molten salt, the general reaction regime can be written as:<sup>116</sup>

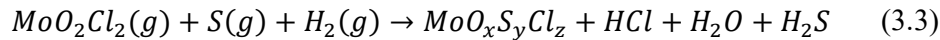


Although the chalcogen precursor can be supplied continually by heating the sulfur powder, the evaporation of metal precursor MoO<sub>3</sub> requires high temperature. Besides, the vapor pressure of the metal precursor is relatively low, which hinders the production of large size 2D MoS<sub>2</sub> layers.

The introduction of molten salt to the metal precursor remarkably promoted the size and growing rate of the prepared sample. Under high temperature conditions, the fusion of MoO<sub>3</sub> with NaCl produce a molten solution, where a volatile compound MoO<sub>2</sub>Cl<sub>2</sub> is formed:



In this case, the vapor pressure of the metal precursor is dramatically improved. Subsequently, the sublimed gas phase MoO<sub>2</sub>Cl<sub>2</sub> will react with the chalcogenide precursor to produce MoS<sub>2</sub> single crystal:



During the sulfurization process of  $\text{MoO}_2\text{Cl}_2$ , an intermediate product  $\text{MoO}_x\text{S}_y\text{Cl}_z$  molecular will form, including  $\text{Mo}_2\text{O}_4\text{SCl}_3$ ,  $\text{MoOSCl}_2$ ,  $\text{MoO}_2\text{SCl}$ ,  $\text{MoOS}_2\text{Cl}_2$ . The O atoms and Cl atoms will be substituted in several steps with the supply of chalcogen source in Ar/H<sub>2</sub> atmosphere. The reaction rate is significantly promoted compared to the reaction without salt-assistant, since the gas-gas phase reaction among  $\text{MoO}_x\text{S}_y\text{Cl}_z$ , H<sub>2</sub> and S is much faster than the solid-gas phase reaction among MoO<sub>3</sub>, H<sub>2</sub> and S.

### 3.2.4 Layer-dependent properties of MoS<sub>2</sub>

The optical images of typical MoS<sub>2</sub> flakes are shown in Figure 3.6, where the areas with different layer numbers are labeled. The production of MoS<sub>2</sub> with varying layer thickness renders the possibility to investigate the layer-dependent properties of MoS<sub>2</sub> nanosheet.

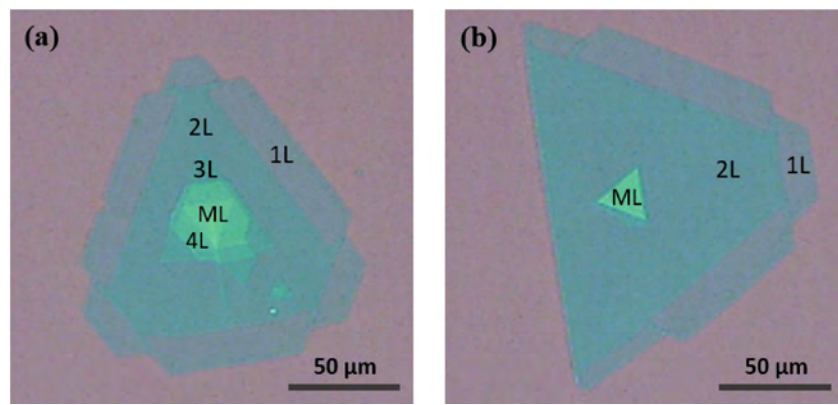


Figure 3.6 a) and b) Optical image of representative MoS<sub>2</sub> flakes with different layer numbers. Scale bars, 50  $\mu\text{m}$ .

Raman spectrum of the representative MoS<sub>2</sub> samples are performed with a confocal Raman spectroscopy under a 532 nm incident laser excitation (see Figure 3.7). All the spectra exhibit strong signals at two dominant peaks, corresponding to the first order E<sup>1</sup><sub>2g</sub> and A<sub>1g</sub> vibration modes. The E<sup>1</sup><sub>2g</sub> peak at around 387 nm implies the in-plane vibration of Mo and S atoms, while the A<sub>1g</sub> peak at 404 nm implies the out-of-plane vibration of S atoms. The frequency difference between the two peaks is strongly dependent on the thickness of MoS<sub>2</sub> samples. As the layer number of MoS<sub>2</sub> increase, the frequency of E<sup>1</sup><sub>2g</sub> mode decreases (red shifts) while the frequency of A<sub>1g</sub> mode increases (blue shift). This layer-dependent frequency shift is consistent with previous reported experimental works and theoretical calculations.<sup>12,63</sup> The blue shift of A<sub>1g</sub> mode can be simply explained by the classical coupled harmonic oscillator model. When the sample thickness is increased from monolayer to bulk MoS<sub>2</sub>, the frequency of A<sub>1g</sub> mode increases since the restoring force between the interlayer S-S bonds is enhanced. On the contrary, E<sup>1</sup><sub>2g</sub> mode exhibit an opposite trend of red shifting. This phenomena implies the dominant effect of enhanced dielectric screen of the long-range Coulomb interactions over the increased interlayer Van der Waals interaction. The dependence of frequency difference on number of MoS<sub>2</sub> layers, as shown in the blue curve of Figure 3.7b, can be used as an identification for the thickness of ultra-thin MoS<sub>2</sub> with less than five layers.

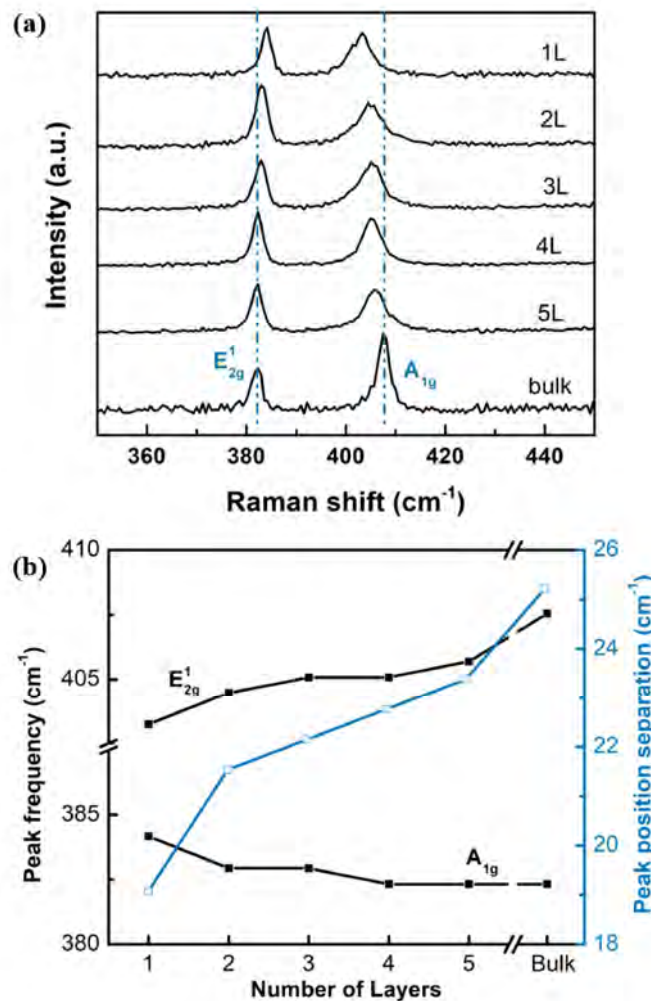


Figure 3.7 a) Raman spectrum of monolayer to a few layer MoS<sub>2</sub>. b) Peak frequency and peak position separation of MoS<sub>2</sub> with varying layer numbers.

The 2D MoS<sub>2</sub> exhibits distinct optical properties from bulk crystals when reduced to its physical limit owing to the strong excitonic effect of monolayer MoS<sub>2</sub>. The photoluminescence spectrum is acquired under the excitation of 532 nm laser with varying layer numbers as exhibited in Figure 3.8. Consistent with previous reports, two exciton emission peaks can be observed. The sharp exciton A peak of ground state exciton centers at a wavelength of 663 nm, corresponding to a bandgap energy of 1.87 eV. The weaker exciton B emission emerged at shorter wavelength originates from the

higher splitting state due to the spin orbit coupling effect. Intriguingly, the behavior of exciton A emission peak exhibits a strong dependence on the thickness of MoS<sub>2</sub>. The increase of PL intensity and blue shift of peak position for thinner sample implies the indirect-to-direct bandgap transitions of MoS<sub>2</sub> from bulk to monolayer.

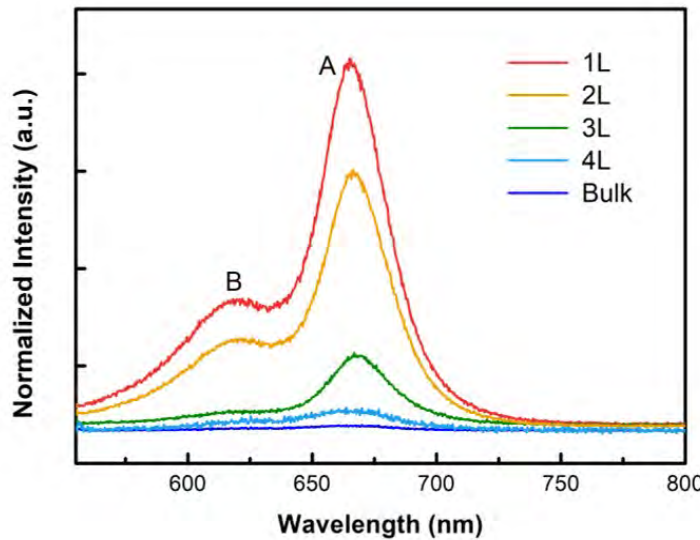


Figure 3.8 Layer dependent PL spectrum of prepared MoS<sub>2</sub> samples.

Moreover, the EDX spectrum performed on MoS<sub>2</sub> sample with composition profile is illustrated in Figure 3.9. Strong peaks of Si and O elements is detected due to the signal from of Si/SiO<sub>2</sub> substrate. Besides, no detectable signal for Na and Cl elements are observed on prepared MoS<sub>2</sub>, implying no residue of salt is caused by the growing process.

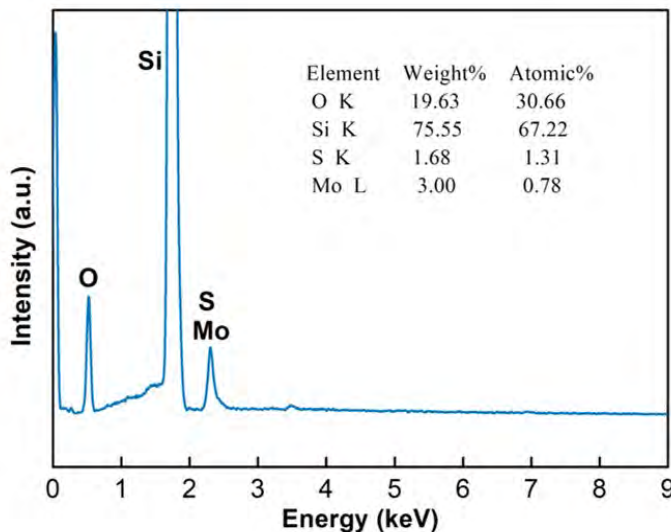


Figure 3.9 EDX spectrum of prepared MoS<sub>2</sub> samples.

### 3.3 Two-step metal-precursor-based deposition of MoS<sub>2</sub>

In this section, a two-step metal-precursor-based deposition method was demonstrated to produce MoS<sub>2</sub> nanosheet. This method employs a pre-deposition route to deliver the metal precursors, which avoided the complexity of the conventional CVD approach including the precursor stoichiometry control and interrelated growth parameters. This two-step CVD method holds great promise for growing 2D TMDs thin films on wafer scale and was also used in other investigations.

#### 3.3.1 Experimental details

Pristine MoS<sub>2</sub> nanosheet was synthesized by a two-step metal-precursor based deposition method carried out in a conventional CVD setup. The first step is presented in Figure 3.10, where the metal precursor was deposited on Si/SiO<sub>2</sub> substrate using magnetron sputtering approach. Specifically, a hard mask was covered on part of the substrate to create a reserved area for self-assembly of the pre-deposited metal film.

The sputtering was conducted for 60 seconds at a power of 100 watts applied on the Mo target.

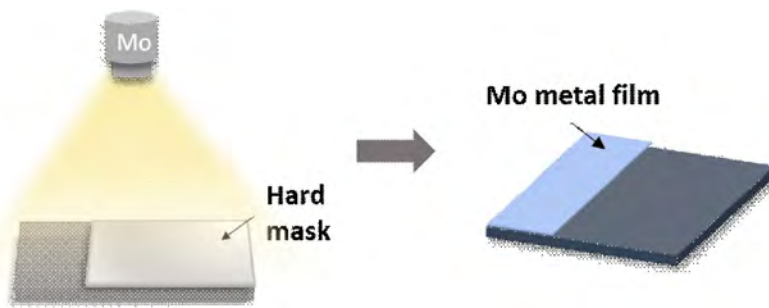


Figure 3.10 Preparation of Mo metal film precursor by magnetron sputtering.

The second step is a sulfurization process in a conventional CVD setup controlled by two heating zones (see Figure 3.11). A quartz boat containing sulfur powder was placed in the upstream of the tube furnace (heating zone I). In the center of quartz tube (heat zone II), the patterned metal film was oriented with metal-seeds-side of the substrate pointing upstream and the blank part of the substrate pointing the exhaust.

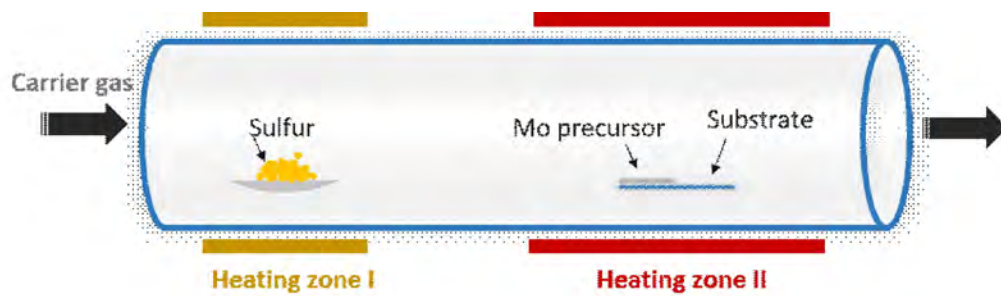


Figure 3.11 Setup for the sulfurization of pre-deposited metal film.

Prior to crystal growth, the quartz tube was vacuumed below 6 Pa and then flushed with Ar/H<sub>2</sub> gas until atmospheric pressure to prevent any possible oxidation pollution by evacuating the residue air. In the subsequent growing process, the pressure was kept at one atmosphere pressure, and the carrier gas was re-introduced

into the tube until both heating zones stabilize at the target temperature for more than one minute to provide sufficient sulfur vapor for crystal growth. The growing temperature and carrier gas profiles are presented in Figure 3.12. The temperature setting points are 180°C and 750°C for heating zone I and II, respectively. It is noted that the temperature in heating zone II is much higher than the melting point of sulfur powder to realize excessive supply of the chalcogen source. After a 10-minutes synthesis process, the furnaces were allowed to naturally cool down to room temperature.

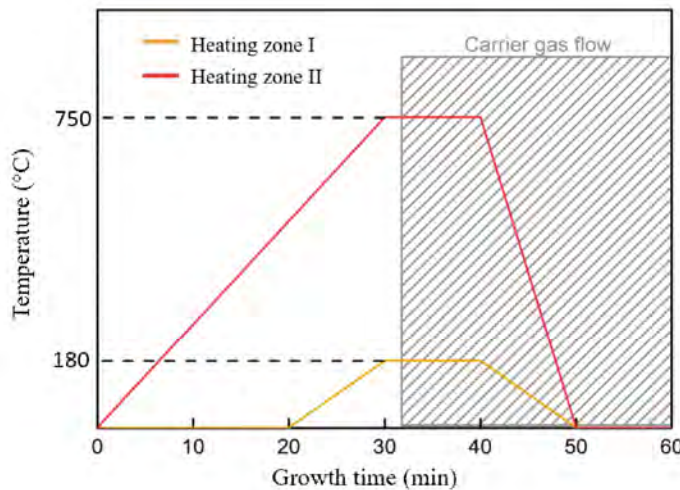


Figure 3.12 Growing temperature and gas flow profile of the deposition process.

During the sulfurization, it should be emphasized that the concentration of sulfur vapor governs the morphology of the grown sample. The two distinct growing schemes induced by the difference of sulfur content will be discussed in the following subsections: In-situ sulfurization and gas phase induced transfer.

### 3.3.2 In-situ sulfurization

Insufficient sulfur concentration can be induced by lower temperature in heating zone I or early stage of introducing the carrier gas. In this case, the

transformation of Mo film to  $\text{MoS}_2$  film occurs accompanied by an increase in thickness, which is similar to previously reported studies. Figure 3.13a shows a schematic diagram of the prepared samples before and after sulfurization, and Figure 3.13b shows the typical optical microscope image of the  $\text{MoS}_2$  film after the sulfurization process.

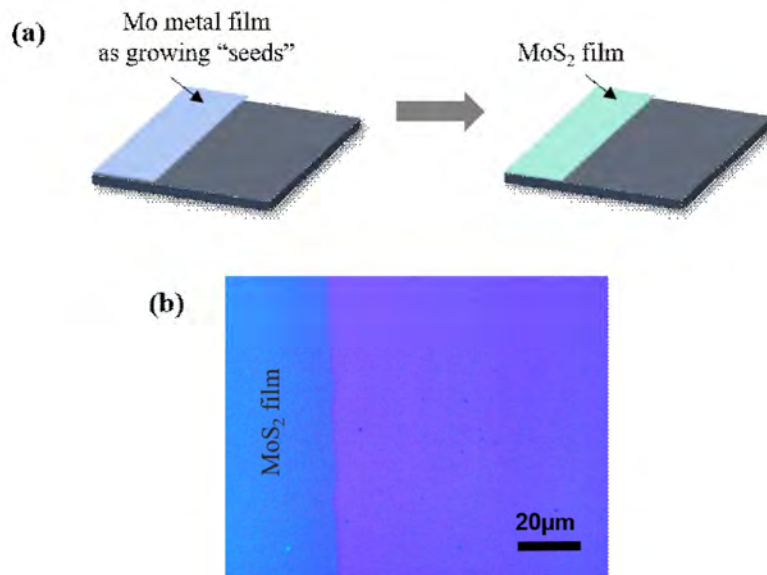


Figure 3.13 a) A schematic of In-situ sulfurization scheme. b) optical microscopy image of the  $\text{MoS}_2$  film after sulfurization. Scale bar, 20  $\mu\text{m}$ .

### 3.3.3 Gas phase induced transfer

By contrast, under sulfur-rich condition, the “seeds” exhibit a carrier gas induced transfer behavior during the sulfurization (see Figure 3.14). The evaporated Mo source from the growing “seeds” reacts with the injected high concentration sulfur vapor and was carried to self-assembly field to form discrete single crystals. The growth yields high crystallinity triangular domains with a typical lateral size of 5  $\mu\text{m}$  at downstream of the pre-deposited “seeds”.

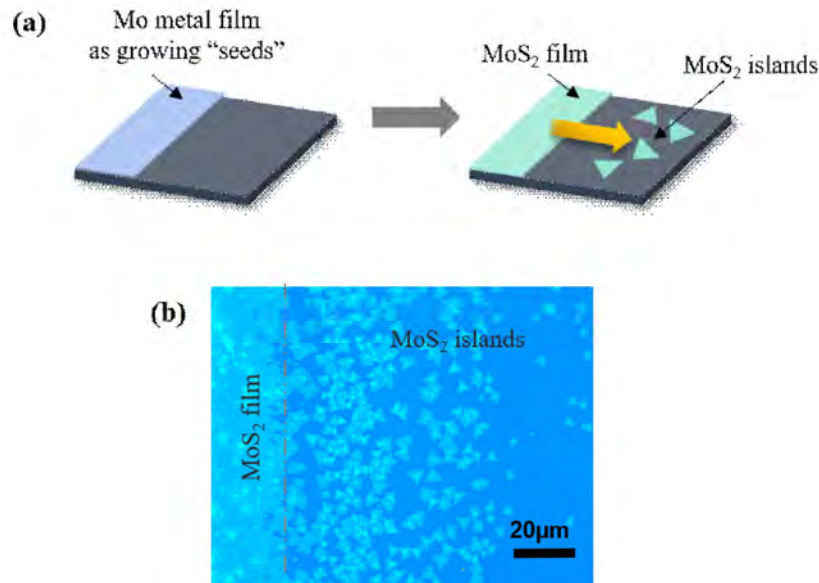


Figure 3.14 a) A schematic of the gas phase induced transfer scheme. b) Optical microscopy image of the resulting MoS<sub>2</sub> film and triangle domains. Scale bar, 20  $\mu\text{m}$ .

### 3.4 Summary

In summary, we investigated the growth of high quality MoS<sub>2</sub> single crystal domains via two kinds of vapor phase deposition methods, namely the molten-salt-assisted CVD method and the two-step metal-precursor-based deposition method. The first method take advantage of the NaCl to facilitate the evaporation of the metal oxide precursor. By formation of a volatile intermediate products under high temperature, the reacting temperature and vapor pressure of metal precursor is drastically improved. Compared with conventional CVD method, this modification renders the possibility to produce 2D TMDs at a relatively low reaction temperature with the steady supply of metal precursors. High quality MoS<sub>2</sub> triangle domains are produced with the thinnest sample down to monolayer thickness. The prepared samples with varying

thicknesses are characterized by Raman and PL spectrum and their layered dependent feature of vibrational mode and optical bandgap was demonstrated.

The second method is a two-step synthesize method involving a pre-deposition of metal precursor and the subsequent sulfurization process. During the sulfurization, the effect of concentration of chalcogen source on the reacting mechanism was investigated by controlling the furnace temperature and gas flow. Under a low sulfur vapor concentration environment, the metal precursors tend to be in-situ sulfurized producing a uniform thin film of MoS<sub>2</sub>. On the contrary, excessive supply of chalcogen source lead to the gas induced transfer of “seeds” to the downstream, forming single crystal MoS<sub>2</sub> domains. Characterized by Raman and PL spectroscopy, the production of monolayer MoS<sub>2</sub> was evidenced. This investigation on growing of 2D TMDs has provided a platform for functionalization and engineering of pristine 2D materials and potential device applications. On the basis of successful production of pristine MoS<sub>2</sub> monolayers, the modulation of MoS<sub>2</sub> photoluminescence by substitutional doping of lanthanide ions will be performed in the following chapters.

# Chapter 4

## Near Infrared Luminescence of Er-Doped MoS<sub>2</sub> Monolayer

### 4.1 Introduction

Lanthanide elements have long been used as dopants in conventional insulating and semiconducting hosts for their superior luminescence properties.<sup>39,76</sup> The abundant energy levels of lanthanide ions enable them to absorb and emit photons in a wide spectrum range from ultra-violet (UV) to infrared region. The lanthanide intra-configuration transitions emerge from the electronic transition between 4f energy states, which are shielded from the surrounding chemical environment by the outer 5d and 6s orbitals.<sup>54</sup> Therefore, this type of electronic transitions is almost independent of the choice of host materials and is commonly used mechanism in lanthanide-based luminescence materials.<sup>34</sup> In particular, the lanthanide emission in near-infrared (NIR) range is located at the “eye safe” spectral region and has promising aspects for in the field of optical communication and biomedical systems.<sup>4,61,78</sup> It should obviously have great attractions for fundamental research and device applications, especially the characteristic NIR emission of Er<sup>3+</sup> ions at 1.54 μm which is in good agreement with

the minimum attenuation of silica fibers commonly used for optical communication systems.<sup>75,80</sup>

Besides, as a typical confinement of TMD semiconducting materials by their bandgap, monolayer MoS<sub>2</sub> possesses a narrow-band emission spectral range from visible to the edge of NIR.<sup>69,92</sup> Modulating and tailoring the luminescence features of 2D MoS<sub>2</sub> is a striking for fundamental research and device applications.<sup>64</sup> Although our previous work has demonstrated the extended NIR emission by successful incorporation of Er into MoS<sub>2</sub> nanosheet, the optimization of crystal quality and sample morphology as well as in-depth understanding of luminescence features requires further investigations. In this chapter, we optimized the growing conditions of Er doped MoS<sub>2</sub> to yield monolayer domains with high crystallinity. Besides, the intriguing lanthanide luminescence features are further investigated such as the concentration quenching and stark splitting effects.

## 4.2 Experimental details

The Er-doped MoS<sub>2</sub> monolayer was prepared using the two-step metal-precursor-based deposition method mentioned in the previous chapter. The incorporation of lanthanide Er<sup>3+</sup> dopant was performed in the pre-deposition process. The Er-doped Mo film was prepared on Si/SiO<sub>2</sub> substrate as reacting precursor via the co-sputtering of individual Mo and Er metals. The concentration of Er dopants was controlled by the magnitude of sputtering power applied on the Er metal target. The mixed metal “seeds” were then sulfurized in a homemade CVD system with two-temperature-zone. The growth process under different sulfur vapor concentration is proposed in Figure 4.1. To guarantee a sufficient supply of chalcogen source, the furnace containing sulfur precursor was heated at a much higher temperature (180°C)

than the melting point of sulfur. Thereby, the deposition followed a gas-phase-induced transfer route, and highly crystalline Er-doped MoS<sub>2</sub> triangle domains were deposited on Si/SiO<sub>2</sub> substrate. In this process, the co-evaporation of Er and Mo alloy significantly decreases the temperature required to evaporate the lanthanide metal. The evaporated Mo and Er atoms react with the injected high concentration sulfur vapor and are carried downstream to the self-assembly region for dopant incorporation and MoS<sub>2</sub> growth.

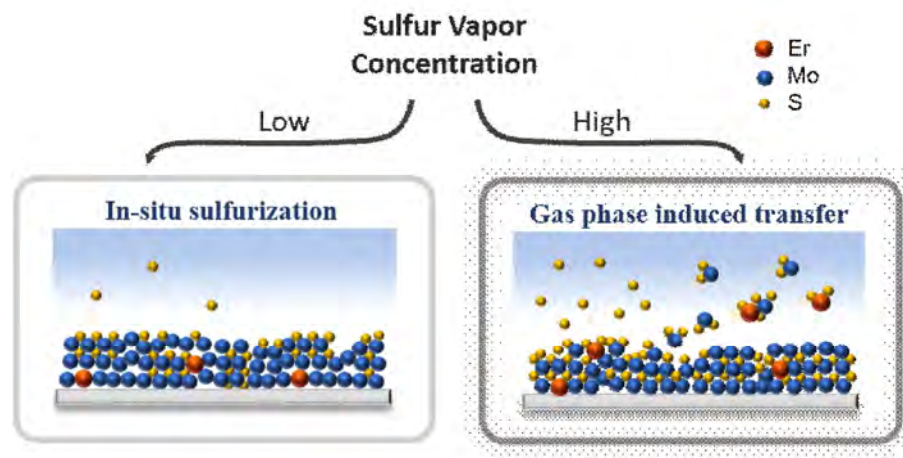


Figure 4.1 Flow chart of the growth process for Er-doped MoS<sub>2</sub> by the two-step alloy based synthesize method.

### 4.3 Comparison of Er-doped and pristine MoS<sub>2</sub> monolayer

#### 4.3.1 Structural property characterization

To investigate the effect of Er embedment on MoS<sub>2</sub> host lattice, a comparison of surface morphology and sample thickness was conducted on MoS<sub>2</sub> triangle islands with and without Er<sup>3+</sup> doping.

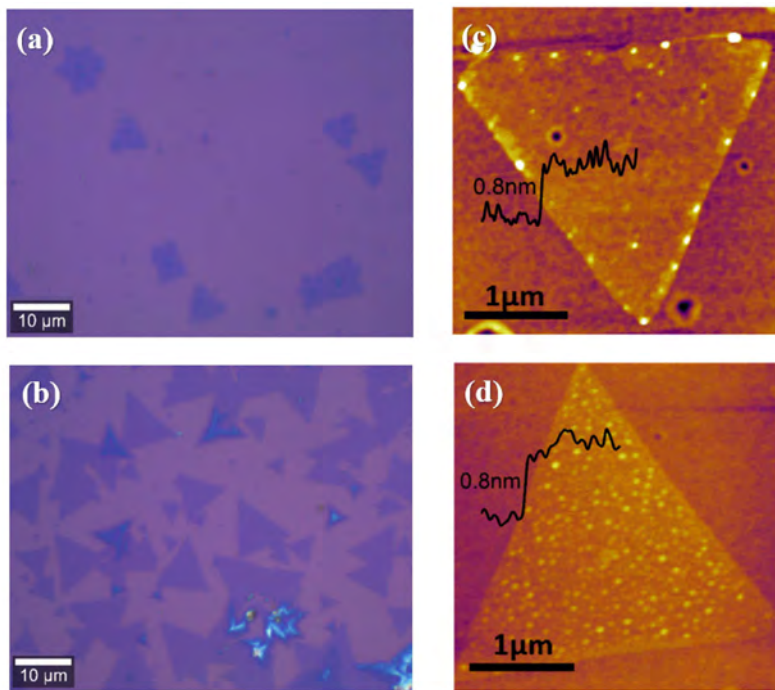


Figure 4.2 Optical images of a) Er-doped MoS<sub>2</sub> and b) pristine MoS<sub>2</sub> grown on Si/SiO<sub>2</sub> substrate. Scale bars, 10 μm. AFM images of c) Er doped MoS<sub>2</sub> and d) pristine MoS<sub>2</sub> single crystals. Scale bars, 1 μm.

Figure 4.2a and 4.2b exhibit the optical microscopy images of pristine and Er-doped MoS<sub>2</sub> flakes, respectively. The color contrast between the bare substrate and the 2D nanosheet renders a quick identification of the shape, location and thickness of prepared samples. The MoS<sub>2</sub> flakes form into clear triangular shapes with a lateral dimension of ~10 μm in both images, confirming the single crystalline nature of synthesized MoS<sub>2</sub> host as evidenced by previous report.<sup>116</sup> For doped triangle domains, the majority of the flake regions consists of monolayer MoS<sub>2</sub>, with small atomic clusters observed at the center of some triangles. Besides, the doped samples exhibit lower flakes density and smaller grain size compared with their pristine counterpart. It was reported that the growth and nucleation of 2D TMDs is highly sensitive to growth environment, such as temperature, precursors, substrates, pressure, and other CVD

parameters.<sup>90,93</sup> This geometry evolution can be attributed to a slight change in the growth environment induced by Er dopants. To perform a precise measurement of sample thicknesses and surface roughness, atomic force microscopy was employed. Figure 4.2c and 4.2d exhibit the surface morphology of a typical pristine and Er-doped MoS<sub>2</sub> monolayer, respectively. As is indicated by the height profiles, the thickness of a typical flake is ~0.8 nm, which is almost comparable to monolayer MoS<sub>2</sub> crystal.

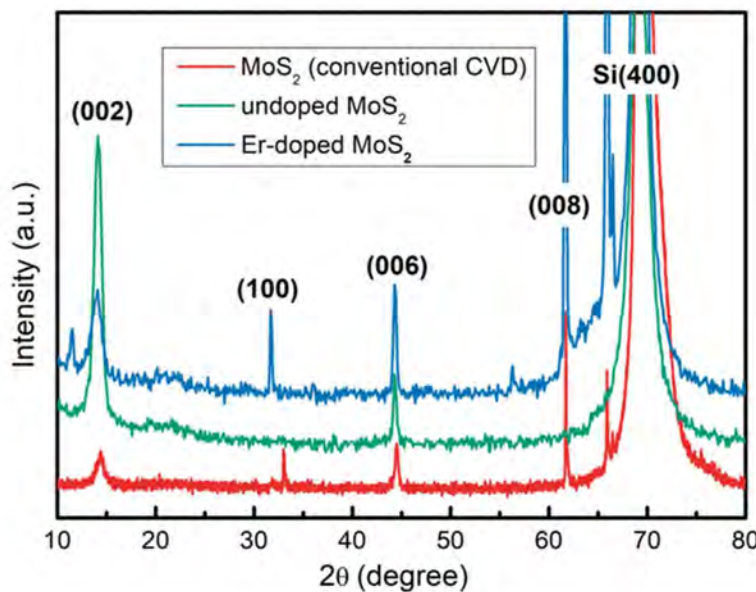


Figure 4.3 XRD patterns of undoped and Er-doped MoS<sub>2</sub>.

The crystal structures of undoped and Er-doped MoS<sub>2</sub> were analyzed by XRD technique, and the MoS<sub>2</sub> grown by conventional CVD method was employed as reference sample (see Figure 4.3). The strong signal at 70.0° is the characteristic peak of Si (400) from the substrate. For pristine MoS<sub>2</sub> samples, there are three dominant peaks located at 14.7°, 44.5°, and 61.8° corresponding to (002), (006), and (008) crystal planes of MoS<sub>2</sub>, respectively. In Er-doped and the reference MoS<sub>2</sub> sample, one more peak at 32.8° is observed, corresponding to (100) planes. No diffraction peaks from Er dopant is detected, indicating that the incorporation of Er ions does not change

the crystal structure of MoS<sub>2</sub> host. However, the XRD is essentially a technique designed for measurements of bulk crystal structure. As the material is reduced to ultrathin thickness, the diffraction peaks often suffer from broadening or absence. In order to further characterize the crystal structure of prepared samples, especially individual grains, other techniques (e.g. Raman spectroscopy) will be adopted in the following sections.

#### 4.3.2 Chemical composition characterization

The chemical composition of synthesized Er-doped MoS<sub>2</sub> was investigated by energy dispersive X-Ray spectroscopy (EDS) and X-ray photoelectron spectroscopy (XPS). The EDS result of the as-grown Er-doped MoS<sub>2</sub> on Si/SiO<sub>2</sub> substrate was exhibited in Figure 4.4, where the characteristic peaks for Mo, S, Er elements can be recognized. The composition profile displays a relatively strong intensity of Si element from the substrate, while the Er element exhibits relatively weak signal due to the detection limit of EDS.

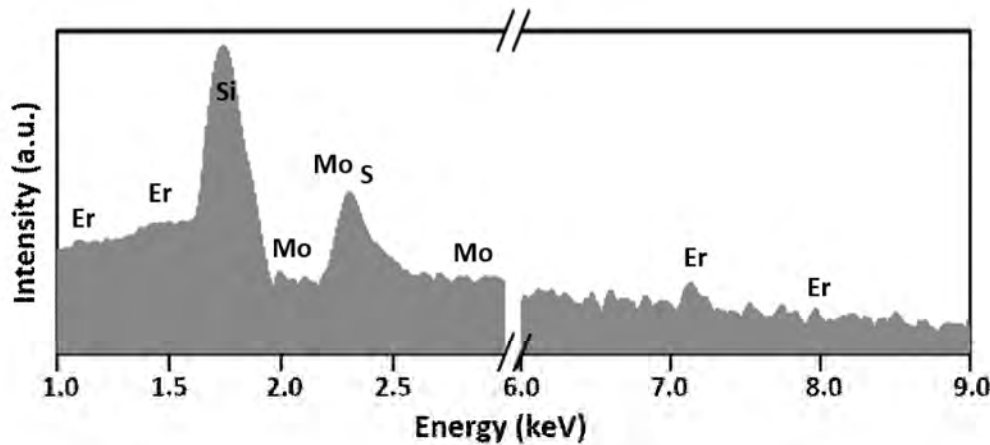


Figure 4.4 EDS results of Mo, S and Er elements on prepared Er doped MoS<sub>2</sub>.

In order to further evidence the successful incorporation of Er element and identify the oxidation state of the dopant Er, XPS measurements were conducted on Er-doped MoS<sub>2</sub> sample. As shown in Figure 4.5a, signals from the host Mo 3d and S 2s can be clearly identified. The XPS spectra in Figure 4.5b exhibits a broad peak of Er 4d core-level centered at 169 eV. The position and shape of this peak is consistent with the previous reported XPS feature of Er trivalent state.<sup>31</sup>

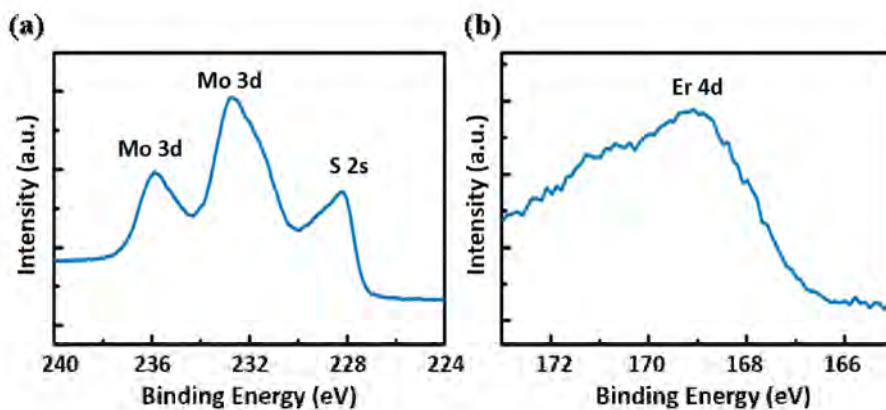


Figure 4.5 XPS results of Er-doped MoS<sub>2</sub> a) Mo 3d, S 2s, and b) Er 4d core levels.

#### 4.3.3 Raman characterization

The embedding of Er atoms into MoS<sub>2</sub> layer renders the possibility to investigate the optical characteristics of Er<sup>3+</sup> in 2D MoS<sub>2</sub> host matrix. Raman spectra on intrinsic and Er-doped MoS<sub>2</sub> monolayer was acquired under 532 nm laser excitation as depicted in Figure 4.6a, where the characteristic Raman peaks of 2H MoS<sub>2</sub> are observed at around 386 and 405 cm<sup>-1</sup>, corresponding to E<sup>1</sup><sub>2g</sub> and A<sub>1g</sub> vibration modes, respectively. The difference between the two characteristic peaks is 19.0 cm<sup>-1</sup>, further evidencing the monolayer structure presented by the above AFM measurements. Notably, the two Raman peaks of Er-embedded MoS<sub>2</sub> single crystal exhibit red-shift of 2 cm<sup>-1</sup> compared with intrinsic MoS<sub>2</sub>, which is consistent with the values in previous

report.<sup>8</sup> Such a Raman shift implies the incorporation of Er dopants into MoS<sub>2</sub> single crystal, which can induce strain near the impurity sites and lead to slight modification of lattice vibration. To further confirm the uniformity of Er embedding into MoS<sub>2</sub> lattice, Raman mapping on the intensity of E<sup>1</sup><sub>2g</sub> and A<sub>1g</sub> peak was performed and exhibited in Figure 4.6b and 4.6c. The triangle regions are of high uniformity in color contrast, highly indicative of crystal quality and smoothness of the synthesized single crystal.

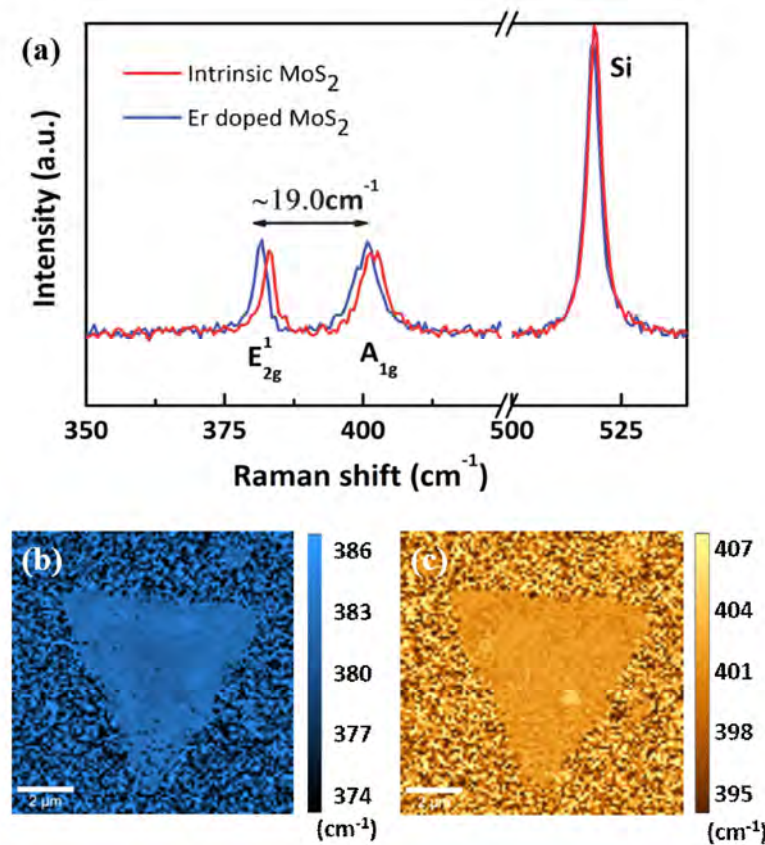


Figure 4.6 a) Raman spectrum of undoped and Er-doped MoS<sub>2</sub> monolayer. Raman mapping of the b)  $E^1_{2g}$  in-plane mode and c)  $A_{1g}$  out-of-plane mode on Er-doped MoS<sub>2</sub> monolayer. Scale bars, 2  $\mu\text{m}$ .

#### 4.3.4 Optical properties characterization

We also compared the optical features of undoped and Er-doped MoS<sub>2</sub> monolayer by acquiring the photoluminescence (PL) spectrum using the confocal Raman system equipped with 532 nm laser excitation. A typical PL emission related to the band-to-band transitions of MoS<sub>2</sub> monolayer is observed at around 1.84 eV in Figure 4.7a. The sharp excitonic A peak of Er doped monolayer MoS<sub>2</sub> is slightly shifted to lower energy compared to intrinsic MoS<sub>2</sub> monolayer. The red shift of emission peak implies the change of chemical environment, which will be explained by computational simulation in the following discussion. The PL mapping of the bandgap emission of Er-doped MoS<sub>2</sub> is shown in Figure 4.7b, which is highly indicative of the consistency and uniformity of the prepared sample.

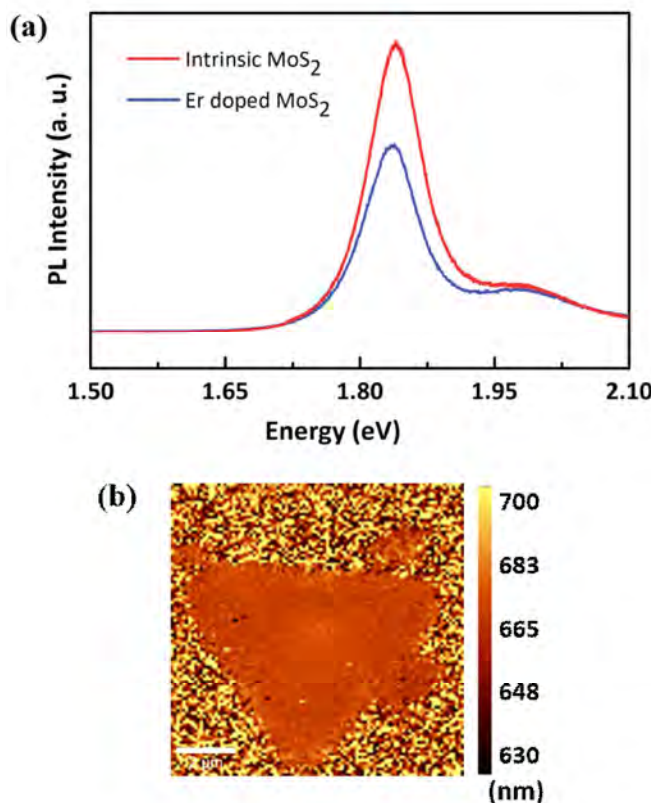


Figure 4.7 a) PL spectrum of undoped and Er-doped MoS<sub>2</sub> monolayer. b) PL mapping of bandgap emission of Er-doped MoS<sub>2</sub>. Scale bar, 2 μm.

## 4.4 Er<sup>3+</sup> NIR Photoluminescence properties analysis

### 4.4.1 NIR PL characterizations

Among the Er<sup>3+</sup> PL emissions, the NIR emission band at 1.53 μm is the most important one for NIR laser applications and broadband optical amplifier at the telecommunication window. For the evaluation of spectroscopic parameters of the 1.53 μm fluorescence in 2D MoS<sub>2</sub> host lattice, the emissions were recorded by exciting the prepared samples with 980 nm diode laser.

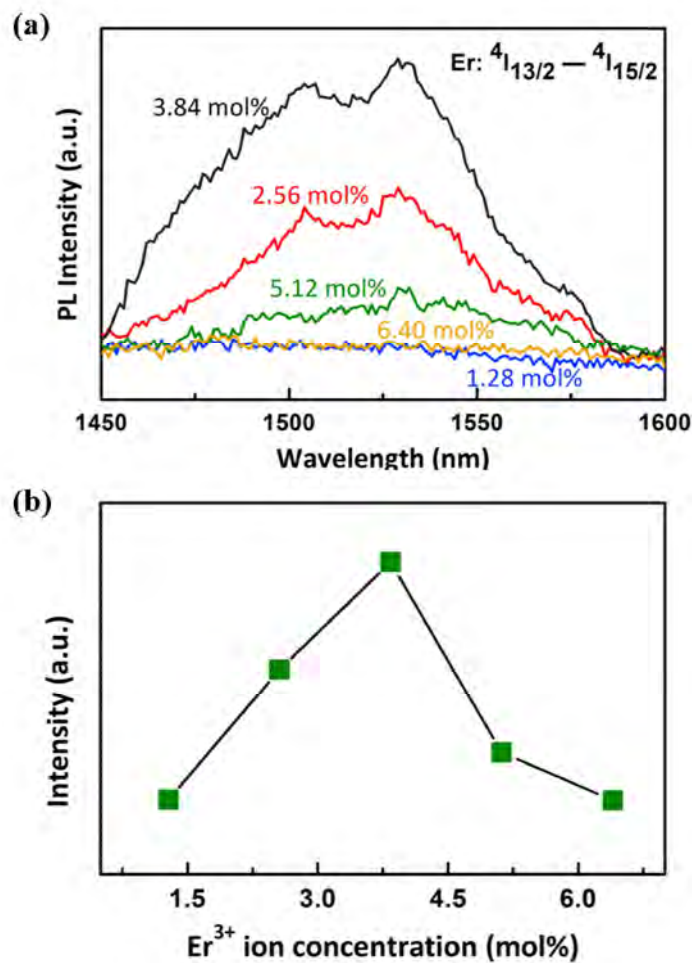


Figure 4.8 a) NIR down-shifting luminescence of Er-doped MoS<sub>2</sub> with different Er<sup>3+</sup> concentration pumped by 980 nm laser. b) Er<sup>3+</sup> concentration dependence on NIR luminescence intensity of Er-doped MoS<sub>2</sub>.

The normalized PL emission spectra measured on samples with different Er<sup>3+</sup> ion concentrations are presented in Figure 4.8a, and the Er content was confirmed by EDX characterization. The intense fluorescence emission peaked around 1530 nm can be clearly observed on curves with nominated Er content of 2.56 and 3.84 mol%. The broad emission band consists of the two peaks centered at 1529 and 1505 nm, which are originated from the stark splitting of Er<sup>3+</sup> 4f levels induced by surrounding crystal fields.<sup>82,91</sup> Figure 4.8b shows the intensity of 1.53 μm characteristic band emission as a function of the Er doping level extracted from the PL emission curves. The PL intensity drastically increases and reaches the maximum at around 4 mol% Er-content, and rapidly decreases with further increment of Er<sup>3+</sup> concentrations. This phenomenon is referred as concentration-quenching, which can be attributed to the increase of non-radiative decay process favored due to interaction between closely spaced impurities in heavily doped samples.

The pump power (P) dependence at 980 nm of the luminescence intensity (I) at 1530 nm was measured by varying the incident energy of the excitation laser. As shown in Figure 4.9, the slope is fitted to be 1.08 according to the dependence of emission intensity on the pump power. This indicated that the down-conversion emission mainly originates from one-photon process.<sup>8</sup>

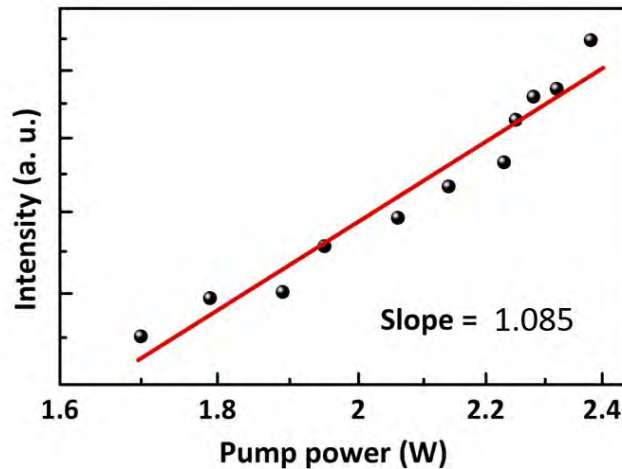


Figure 4.9 The pump power dependence of PL intensity at 1530 nm emission peak.

The mapping image of the NIR PL spectra in terms of position and intensity on Er-doped MoS<sub>2</sub> sample is shown in Figure 4.10, suggests a uniform coverage and luminescence profile of Er-doped MoS<sub>2</sub> on the substrate.

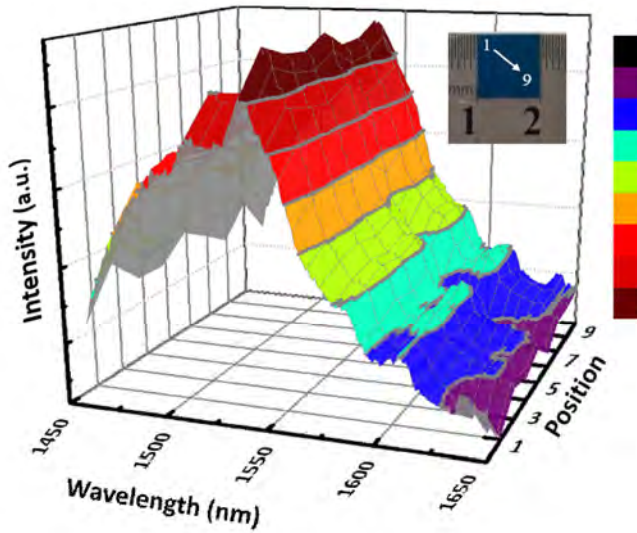


Figure 4.10 PL spectra mapping image of 1530 nm emission peak of nine spots in a line.

#### 4.4.2 Energy transfer mechanism

The NIR emission of Er-doped MoS<sub>2</sub> at 1530 nm can be attributed to the electronic transitions between the 4f energy levels of Er<sup>3+</sup> ions. The introduced of lanthanide dopants created a series of ladder like energy states into the bandgap of monolayer MoS<sub>2</sub>. These energy levels are capable of absorbing and emitting photons which fit well with the corresponding energy difference. Upon the 980 nm laser pumping, electrons are populated from the ground state  $^4I_{15/2}$  to the  $^4I_{11/2}$  manifold. The excited electrons then rapidly non-radiative relaxed to the  $^4I_{13/2}$  metastable level where the radiative transitions then take place. The splitting of the 1530 nm spectral line into several components observed in the emission spectra can be explained by the basic model of the stark manifold, as shown in Figure 4.11, where the two energy states related to the NIR emission is depicted.

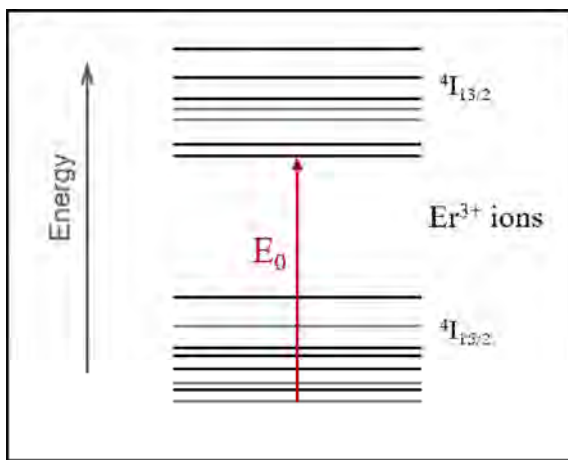


Figure 4.11 Diagram of stark manifold of partial 4f levels of Er<sup>3+</sup> ions.

Although the 4f orbitals are shielded from the chemical environment by 6s and 5p shells, the degeneracy of the spin-orbital states can be shifted and split. Similar to the model proposed in previous studies on Er activated glasses, the ground state  $^4I_{15/2}$  and the excited state  $^4I_{13/2}$  are manifolds of multiple sublevels in the presence of surrounding crystal fields.<sup>91</sup> Although the stark splitting varies with different hosts, the

crystal-field splitting is much less than the separation of spin-orbital states.<sup>82</sup> Therefore, the main luminescence features associated with lanthanide f-f transition remain unchanged in different host materials.

## 4.5 Summary

In summary, this chapter demonstrated the luminescence property of lanthanide Er<sup>3+</sup> ion incorporated into of 2D MoS<sub>2</sub> host. The Er-doped MoS<sub>2</sub> monolayer was synthesized by a two-step CVD method. A mixed metal film precursor is utilized to deliver the Er dopant via co-evaporation of Mo and Er metal. The pristine and doped MoS<sub>2</sub> triangle domains are compared in terms of structural properties and chemical composition. The Raman peak of doped MoS<sub>2</sub> monolayer exhibits a slightly shift to the lower wavenumber. The uniformity of doping is characterized by Raman mapping on representative triangle domains. The existence and concentration of Er doping is confirmed by EDS and XPS measurements. Most importantly, the luminescence emission of monolayer MoS<sub>2</sub> are effectively extended to the NIR spectral range. we further characterized the NIR photoluminescence features of Er<sup>3+</sup> ions by measuring the PL emission at different Er<sup>3+</sup> content. A concentration quenching effect with the optimal doping concentration of 4 mol% was observed. Besides, the spectral line at 1530 nm exhibits stark splitting into several components due to the presence of crystal field. The PL intensity dependence on pumping power was characterized, implying that the down-conversion emission contributes to one-photon process.

The synthesize approach used in this chapter can possibly be generalized to arbitrary desired substrates, since the pre-deposition of metal seeds might not be limited by the substrates used or melting points of the dopants. Besides, this method

possesses the advantage of low cost, environmentally stable, scale-up process, which has the potential to be expanded for synthesizing other 2D materials.

# Chapter 5

## Density Functional Theory Calculation of Er-doped MoS<sub>2</sub> Monolayer

### 5.1 Introduction

The functionalization and modulation of monolayer MoS<sub>2</sub> has been extensively investigated by composition engineering experiments such as alloying or doping, and their related devices have been fabricated to take advantage of the superior properties. Motivated by the advances in research on experimental techniques, theoretical calculations have been demonstrated to investigate the doping engineering of monolayer MoS<sub>2</sub>.<sup>41</sup> Various types of dopants, such as transition metal or non-metal atoms have been incorporated into MoS<sub>2</sub> lattice to understand and control the induced properties.<sup>59,67,68</sup> For example, the first principle calculations on p-type doping by Nb and n-type doping by Re have opened the possibility of enhancing the electrical conductivity of single layer MoS<sub>2</sub> by controlled doping process.<sup>22</sup> Feng et al. investigated the formation of impurity states close to the Fermi level in Fe-doped 2D MoS<sub>2</sub> and predicted their potential device applications.<sup>25</sup> Despite emerging studies on first principle modeling of substitutional doping of MoS<sub>2</sub>, literatures on simulations of lanthanide doping in MoS<sub>2</sub> is still scarce. The lanthanide elements, possessing

abundant 4f energy levels, are capable of implementing magnetic properties, inducing novel luminescent feature and modulating the electronic properties when incorporated into a variety of semiconductor hosts. A recent study on the magnetism in Gd-doped MoS<sub>2</sub> monolayers have demonstrated by density functional theory simulation.<sup>114</sup> The structural, electronic and magnetic properties of lanthanide (Sm, Eu, Gd, Tb, and Dy) doped MoS<sub>2</sub> monolayer have been reported.<sup>58</sup> This chapter analyzed the stabilization of Er doping on monolayer MoS<sub>2</sub> host by calculating the doping formation energy and crystal structural. The luminescence feature of Er<sup>3+</sup> dopant is evaluated based on the electronic structure with Dieke diagram.

## 5.2 Computational details

### 5.2.1 Density functional theory details

To investigate the growth mechanism and the possible effects of the incorporated lanthanide ions on MoS<sub>2</sub> monolayer host matrix, density functional theory (DFT) calculations were performed using the pseudopotentials implementation provided in Standard Solid-State Pseudopotential (SSSP) library version 1.0 within the plane-wave code Quantum Espresso (QE). For the exchange and correlation functional, generalized gradient approximation (GGA) with Perdew Burke-Ernzerhof parametrization (PBE) was used with DFT+U formulism based on Hubbard model. To be more specific, Vanderbilt ultrasoft pseudopotential for Mo and Er atoms, Projector-augmented wave (PAW) pseudopotential for S atoms were applied. Kinetic energy cutoff values for wavefunctions E<sub>cutwfc</sub> and potentials E<sub>cutrho</sub> in all calculations were set as 25 Ry and 200 Ry to meet the requirement of ultrasoft pseudopotentials (E<sub>cutrho</sub> >= 8 E<sub>cutwfc</sub>).

A vacuum layer with the thickness of 20 Å was used to minimize interactions between adjacent image cells in monolayer calculations. The k-points sampling with a Monkhorst-Pack mesh was set as 3 x 3 x 1 for monolayer structure so that spacing between energy adjacent k-points along each direction was roughly 0.2 Å<sup>-1</sup>. All geometric optimizations were computed using a Marzari-Vanderbilt cold smearing of 0.02 Ry. Convergence energy threshold for self-consistent calculations was 10<sup>-6</sup> Ry. All the atomic coordinates and lattice parameters were optimized with the Broyden-Fletcher-Goldfarb-Shanno (BFGS) quasi-Newton algorithm until the residue force on atoms below 10<sup>-6</sup> Ry/Å.

### 5.2.2 Doping procedure

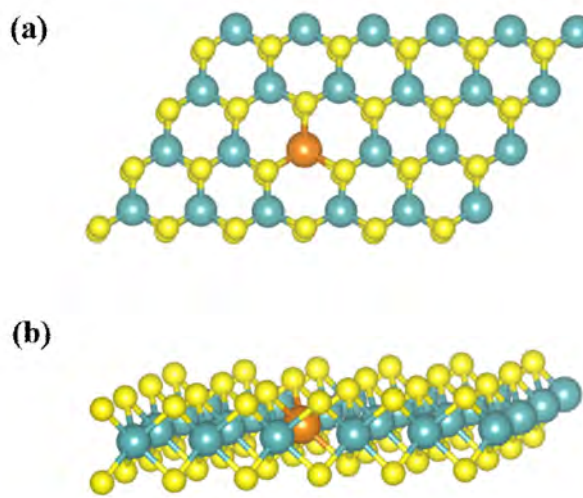


Figure 5.1 a) Top view and b) side view of Er doped supercell. Blue, yellow and orange balls represent Mo, S, Er atoms, respectively.

The lattice constants and ion positions of pristine MoS<sub>2</sub> monolayer was first relaxed. Doping of Er was performed by substituting one Mo atom by one Er atom. To achieve a doping concentration of around 4 at%, which is approximately the optimized

Er doping concentration measured in the previous experimental section. The approximated Er doping concentration optimized in the previous experimental section is around 4 at%. To achieve a similar level of Er content, a supercell of MoS<sub>2</sub> monolayer containing 72 atoms with replication of 4 x 6 along the in-plane direction was employed, yielding an Er doping concentration of 4.16 mol%. The top view and side view of Er doped supercells are shown in Figure 5.1a and 5.1b, respectively. The Blue, yellow, orange balls represent Mo, S, Er atoms, respectively.

### 5.2.3 Simulation analysis

The formation energy of doping  $E_{form}$  is calculated following the previously reported method:

$$E_{form} = E_{doped} - E_{pristine} - \mu_{Er} + \mu_{Mo} \quad (5.1)$$

$E_{doped}$  and  $E_{pristine}$  are the total energies of the well relaxed doped and pristine MoS<sub>2</sub> supercell, respectively.  $\mu$  denotes the chemical potential for different elements. The chemical potential of the Er dopant  $\mu_{Er}$  is obtained from energy of bulk metal with hexagonal structure. The chemical potential of Mo is typically considered between the two limits, i.e., Mo-rich (S-poor) condition and S-rich (Mo-poor) condition. Under Mo-rich condition, the chemical potential of Mo is set as the total energy of a Mo atom in ground state Mo bulk crystal. While in S-rich case, the chemical potential of Mo is obtained assuming the equilibrium of MoS<sub>2</sub> with the chalcogen source. Therefore,  $\mu_{Mo}$  can be defined as:

$$\mu_{Mo}^{S-poor} = \mu_{Mo}^0 \quad (5.2)$$

$$\mu_{Mo}^{S-rich} = E_{MoS_2} - 2\mu_S^0 \quad (5.3)$$

where  $\mu_{Mo}^0$  and  $\mu_S^0$  are the chemical potential taken in standard conditions, respectively.  $E_{MoS_2}$  is the energy of a perfect MoS<sub>2</sub> crystal per formula unit. All the chemical potentials are computed using DFT calculations.

## 5.3 Structure properties and energetics

### 5.3.1 Crystal structure of pristine and Er-doped MoS<sub>2</sub> monolayer

The parameters of the well relaxed structure for pristine and Er doped MoS<sub>2</sub> monolayer are listed in Table 5.1.

Table 5.1 Calculated lattice parameters of Er doped MoS<sub>2</sub> monolayer

	Atomic radius (Å)		Bond length (Å)		Angle (°)	
Pure MoS <sub>2</sub>	Mo	1.90	Mo-S	2.40	S-Mo-S	81.07
Er: MoS <sub>2</sub>	Er	2.26	Er-S	2.62	S-Er-S	84.82
Distortion	-	-	-	9.2%	-	4.6%

Comparing the parameters of doped and pristine monolayer structure, an outward distortion of S atoms around the Er dopant sites can be observed due to the atomic radius difference between Er and Mo atoms. The Er-S bond is elongated by roughly 9.2% compared with Mo-S bonds, compared with Mo-S bonds. The S-Er-S angle is increased by around 4.6% compared with S-Mo-S angles.

### 5.3.2 Doping energy calculation

The detailed results of doping energy calculation are listed in Table 5.2. As is shown, the calculated doping energies under S-rich and S-poor condition are 0.83 and 3.53 eV, respectively, which has the same trend with the reported first principle calculations of MoS<sub>2</sub> monolayer doped with other lanthanide species. Evidenced by the computed energies, the incorporation of Er is highly favored under S-rich conditions since the doped system will be more stable, which is consistent with our experimental results. Higher chemical potential of S originated from high vapor concentration facilitate the transfer of “seeds” and formation of doped single crystal.

Table 5.2 Computed energies of various compounds

	S-rich Condition	S-poor Condition
$E_{doped}$ (eV)		-50570.31
$E_{pristine}$ (eV)		-40387.65
$\mu_S$ (eV)	-327.84	-329.19
$\mu_{Mo}$ (eV)	-1868.45	-1865.75
$\mu_{Er}$ (eV)		-12051.93
$E_{form}$ (eV)	0.83	3.53

## 5.4 Electronic properties

### 5.4.1 Density of state calculation

The density of state (DOS) of doped MoS<sub>2</sub> monolayer with individual element contribution is shown in Figure 5.2. After Er<sup>3+</sup> doping, the majority of the DOS

structure remains unchanged since the electronic bands are mainly composed of host Mo and S states. The  $\text{Er}^{3+}$  impurity doping gives rise to the maximum of electron density distribution emerging at the edge of valence band, resulting in narrowing host bandgap. As demonstrated in the projected DOS of  $\text{Er}^{3+}$  contribution, these impurity states observed in  $\text{MoS}_2$  bandgap can be attributed to the unfilled 4f shell. The location of the  $\text{Er}^{3+}$  4f ground state in  $\text{MoS}_2$  host bandgap was estimated as 0.55 eV using reported methods,<sup>74</sup> by taking the energy difference between the maximum of  $\text{Er}^{3+}$  4f states and Mo states at -0.12 and -0.67 eV, respectively. This value will be used in the calculation of energy level diagram in next section, linking the 4f levels of  $\text{Er}^{3+}$  with bandgap of monolayer  $\text{MoS}_2$  host matrix.

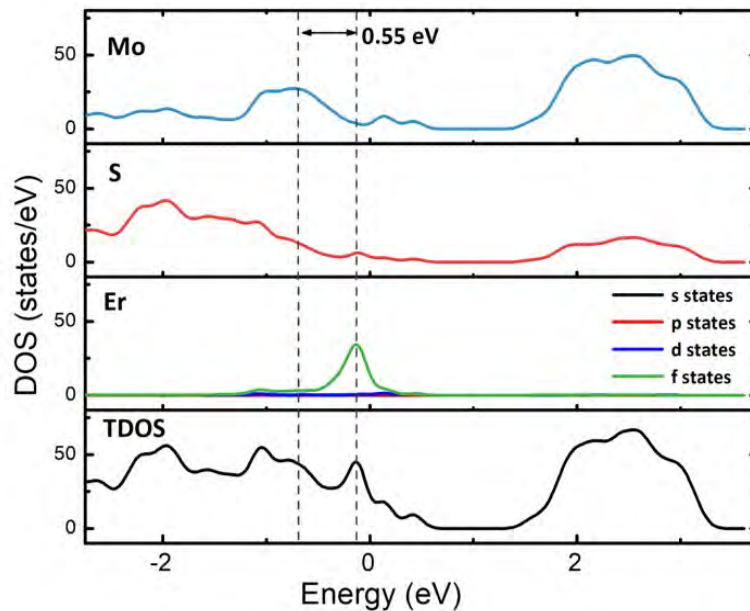


Figure 5.2 Calculated DOS of Er-doped  $\text{MoS}_2$  monolayer.

#### 5.4.2 Electronic band structure calculation

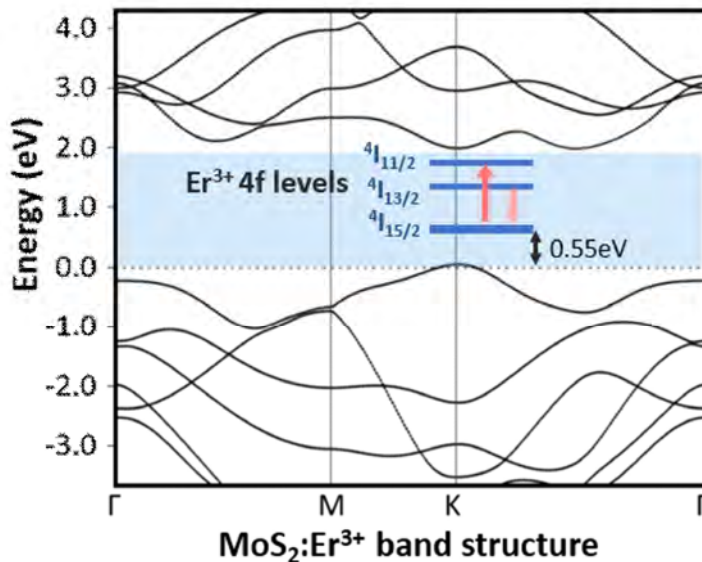


Figure 5.3 Schematic partial energy level diagram of Er<sup>3+</sup> ion doped in 2D MoS<sub>2</sub>.

The calculation of electronic band structure was performed involving the interaction between the Er impurity states and the host states. The schematic energy level diagram associated to the excitation and emission path of incorporated Er ions into 2D MoS<sub>2</sub> system is depicted in Figure 5.3. The incorporation of Er<sup>3+</sup> ions introduces extra energy states within MoS<sub>2</sub> bandgap, offering more possibilities of energy transitions leading to NIR emission. The lowest Er 4f state is located 0.55 eV above the top of MoS<sub>2</sub> valence band estimated by theoretical calculations in the previous subsection. Since the lanthanide 4f-4f transitions are typically independent of host matrix owing to the shielding of the outer orbitals, the location of other unfilled 4f states are deduced according to the Dieke diagram.<sup>54,74</sup> The alignment of these unfilled 4f levels depicted inside 2D MoS<sub>2</sub> bandgap enables the energy transitions at 980 and 1530 nm in host matrix. Upon 980 nm laser pumping, electrons are populated from the ground state  $^4I_{15/2}$  to the  $^4I_{11/2}$  manifold and rapidly non-radiative relaxed to  $^4I_{13/2}$  metastable level where the radiative transitions then take place. This proposed

model is in well accordance with our experiment and implies that 2D MoS<sub>2</sub> can be an appropriate host candidate to promote the NIR emission at 1.53 μm of the incorporated Er<sup>3+</sup> ions.

## 5.5 Summary

In this chapter, we demonstrated the density functional theory calculation of Er-doped MoS<sub>2</sub> monolayer. The formation of doping under different chalcogen source content is evaluated by comparing the doping energy. All the ground state energies and chemical potentials are calculated using the QE package. It was found that the formation of cation substitutional doping is more favored under sufficient sulfur supply. The stability of the doped system was investigated by modeling the lattice structure of MoS<sub>2</sub> host before and after the incorporation of Er dopants. The substitutional doping is realized by replacing one Mo atom by Er atom in a supercell containing 72 atoms, yielding an impurity concentration of 4.16 mol%. After the structure of Er doped MoS<sub>2</sub> monolayer is fully relaxed, the crystal lattice exhibits a slight distortion at S sites around the Er dopants. Besides, the electronic properties of Er-doped MoS<sub>2</sub> monolayer were simulated. From the projected density of state calculation of individual element contribution, we identified the position of the impurity states induced by dopants with respect to the host MoS<sub>2</sub> bandgap. The 4f energy levels of lanthanide Er<sup>3+</sup> are predicted by combining the first principle calculation results with Dieke diagram. The simulated energy level diagram is in well consistent with our experimental findings. This investigation provided an in-depth understanding of lanthanide doping in 2D MoS<sub>2</sub> monolayer, which is useful for designing of doping engineering in 2D semiconducting materials.

# Chapter 6

## Conclusion and Future Prospects

### 6.1 Conclusion

Activation of 2D semiconducting materials by chemical doping has drawn considerable attention for fundamental research and device fabrications. The tailoring of the intrinsic properties of 2D TMDs has been realized by careful control of dopant types, doping concentration and the synthesize process. In this thesis, the incorporation of Er dopant in MoS<sub>2</sub> monolayer is demonstrated experimentally and theoretically. The luminescence of 2D MoS<sub>2</sub> host has been extended to the NIR spectrum including the telecommunication range at 1530 nm. The details of this thesis are summarized below.

Firstly, by choosing the prototypical member MoS<sub>2</sub> in 2D TMDs family as the host material, we initiate the study with the synthesis of pristine MoS<sub>2</sub> monolayer. Two kinds of vapor deposition methods were demonstrated to prepare large-scale highly quality MoS<sub>2</sub> single crystals, namely molten-salt assisted CVD method and two-step metal-precursor-based deposition method. The first approach employed NaCl to assist the melting and evaporation of the metal reacting source. The incorporation of salt renders the possibility to conduct the reaction at a relatively low temperature in the atmosphere of higher precursor vapor pressure. This method yields MoS<sub>2</sub> triangle

domains with controllable thickness, which was evaluated by the layer number dependent characteristic of Raman peaks. The second approach took advantage of pure Mo metal as the reacting precursor prepared by sputtering process. By controlling the chalcogenide precursor at a high content during the sulfurization, MoS<sub>2</sub> single crystal domains with lateral size up to 10 μm is formed. The monolayer nature of prepared samples was confirmed by Raman spectrum and AFM measurement.

The investigation on synthesize of pristine MoS<sub>2</sub> monolayer opened the platform for further development of Er incorporation. By exploiting a two-step approach of metal precursor synthesis using pre-deposited metal film as “seeds”, we have fabricated Er embedded MoS<sub>2</sub> triangle islands along in-plane size up to around 10-μm, which is apparently formed into single crystal. Intriguingly, highly crystalline MoS<sub>2</sub>:Er flakes are formed on self-assembly region only under high sulfur vapor concentration. Comparisons on the structural property, chemical composition, and optical property of pristine and doped samples were demonstrated. Most importantly, the NIR emission from Er-doped MoS<sub>2</sub> was observed under 980 nm laser excitation, implying the successful modulation of the narrow band emission. Besides, some intriguing luminescence features such as concentration quenching effect and stark splitting was investigated.

Lastly, to understand the growing mechanism and doping effect from a theoretical aspect of view, first principle study on Er-doped MoS<sub>2</sub> monolayer was demonstrated. By calculation of doping formation energy, the Er dopant is found to be more stable in a sulfur rich environment. The crystal structural simulation indicates that the substitutional doping of Er on Mo site can be stable regarding the lattice distortion. Besides, from the DOS calculation of Er doped MoS<sub>2</sub>, we successfully

identified the position of the lowest  $\text{Er}^{3+}$  4f levels in  $\text{MoS}_2$  bandgap. By combining the Dieke diagram with the band structure of pristine  $\text{MoS}_2$ , we simulated the interaction of impurity states with the host bandgap, which is in well agreement with our experimental findings.

## 6.2 Future prospects

The incorporation of lanthanide Er dopant in 2D  $\text{MoS}_2$  matrix demonstrated in this work has opened the possibility for future investigation into lanthanide doping and alloying of 2D materials. The near-infrared (NIR) emission of  $\text{Er}^{3+}$  ions has significant promising owing their perfect match to the low loss window of silica optical fiber in optical communication industry. As a future work, the  $\text{Er}^{3+}$  activated electroluminescence devices can be constructed based on the prepared materials. Besides, the proposed synthesize method possesses the advantage of low cost, environmentally stable, scalable and universally versatile. It can possibly be generalized to synthesize of other 2D materials doped with various elements. Atomically thin TMDs doped with most types of lanthanide elements, which are tricky to be prepared using conventional CVD approach, may be synthesized using this method. For example, the  $\text{Nd}^{3+}$  ions exhibiting a sharp NIR luminescence peak at 1.08  $\mu\text{m}$  under the excitation wavelength of 808 nm is one of the promising candidates for TMDs hosts.

Moreover, the currently used 2D TMDs semiconducting materials typically have a narrow bandgap, which is fully transparent to low energy photons in the NIR spectral range and strongly absorb the visible light. Confining by the bandgap absorption feature, the incorporation of lanthanide ions with visible luminescence characteristic typically yields low emission intensity. With the rapid advance of material synthesis

technology and computational simulation power, the prediction and discovery of 2D materials are emerging rapidly. 2D semiconductor candidates with larger optical bandgap intrinsically possess a wider platform for the modulation of luminescence wavelength. Thus, they have prospective potentials as host materials for lanthanide ions and are more promising for development of novel optoelectronic devices.

## References

1. Ackland, G. J.; Warren, M. C. & Clark, S. J. Practical methods in ab initio lattice dynamics. *Journal of Physics: Condensed Matter*. **1997**, *9*, 7861.
2. Angel, R. J. Structure and Dynamics an Atomic View of Materials. *Mineralogical Magazine*. **2003**, *67*, 827.
3. Asokan, V.; Zhu, D.; Huang, W.; Wang, H.; Gao, W.; Zhang, Z. & Jin, C. Growth of ‘W’ doped molybdenum disulfide on graphene transferred molybdenum substrate. *Scientific Reports*. **2018**, *8*, 7396.
4. Ayvacıklı, M.; Khatab, A.; Ege, A.; Şabikoğlu, İ.; Henini, M. & Can, N. Absorption and photoluminescence spectroscopy of Er<sup>3+</sup>-doped SrAl<sub>2</sub>O<sub>4</sub> ceramic phosphors. *Philosophical Magazine Letters*. **2012**, *92*, 194.
5. Azcatl, A.; Qin, X.; Prakash, A.; Zhang, C.; Cheng, L.; Wang, Q.; Lu, N.; Kim, M. J.; Kim, J.; Cho, K.; Addou, R.; Hinkle, C. L.; Appenzeller, J. & Wallace, R. M. Covalent Nitrogen Doping and Compressive Strain in MoS<sub>2</sub> by Remote N<sub>2</sub> Plasma Exposure. *Nano Letters*. **2016**, *16*, 5437.
6. Bai, G.; Tsang, M.-K. & Hao, J. Luminescent Ions in Advanced Composite Materials for Multifunctional Applications. *Advanced Functional Materials*. **2016**, *26*, 6330.
7. Bai, G.; Yang, Z.; Lin, H.; Jie, W. & Hao, J. Lanthanide Yb/Er co-doped semiconductor layered WSe<sub>2</sub> nanosheets with near-infrared luminescence at telecommunication wavelengths. *Nanoscale*. **2018**, *10*, 9261.

8. Bai, G.; Yuan, S.; Zhao, Y.; Yang, Z.; Choi, S. Y.; Chai, Y.; Yu, S. F.; Lau, S. P. & Hao, J. 2D Layered Materials of Rare-Earth Er-Doped MoS<sub>2</sub> with NIR-to-NIR Down- and Up-Conversion Photoluminescence. *Adv Mater.* **2016**, *28*, 7472.
9. Behura, S. & Berry, V. Interfacial Nondegenerate Doping of MoS<sub>2</sub> and Other Two-Dimensional Semiconductors. *ACS Nano.* **2015**, *9*, 2227.
10. Bernasconi, M.; Chiarotti, G. L.; Focher, P.; Scandolo, S.; Tosatti, E. & Parrinello, M. First-principle-constant pressure molecular dynamics. *Journal of Physics and Chemistry of Solids.* **1995**, *56*, 501.
11. Bhimanapati, G. R.; Lin, Z.; Meunier, V.; Jung, Y.; Cha, J.; Das, S.; Xiao, D.; Son, Y.; Strano, M. S.; Cooper, V. R.; Liang, L.; Louie, S. G.; Ringe, E.; Zhou, W.; Kim, S. S.; Naik, R. R.; Sumpter, B. G.; Terrones, H.; Xia, F.; Wang, Y.; Zhu, J.; Akinwande, D.; Alem, N.; Schuller, J. A.; Schaak, R. E.; Terrones, M. & Robinson, J. A. Recent Advances in Two-Dimensional Materials beyond Graphene. *ACS Nano.* **2015**, *9*, 11509.
12. Bilgin, I.; Liu, F.; Vargas, A.; Winchester, A.; Man, M. K. L.; Upmanyu, M.; Dani, K. M.; Gupta, G.; Talapatra, S.; Mohite, A. D. & Kar, S. Chemical Vapor Deposition Synthesized Atomically Thin Molybdenum Disulfide with Optoelectronic-Grade Crystalline Quality. *ACS Nano.* **2015**, *9*, 8822.
13. Cai, Z.; Liu, B.; Zou, X. & Cheng, H. M. Chemical Vapor Deposition Growth and Applications of Two-Dimensional Materials and Their Heterostructures. *Chem Rev.* **2018**, *118*, 6091.
14. Chen, K.; Wan, X.; Xie, W.; Wen, J.; Kang, Z.; Zeng, X.; Chen, H. & Xu, J. Lateral Built-In Potential of Monolayer MoS<sub>2</sub>–WS<sub>2</sub> In-Plane Heterostructures by a Shortcut Growth Strategy. *Advanced Materials.* **2015**, *27*, 6431.

15. Chhowalla, M.; Shin, H. S.; Eda, G.; Li, L. J.; Loh, K. P. & Zhang, H. The chemistry of two-dimensional layered transition metal dichalcogenide nanosheets. *Nat Chem.* **2013**, *5*, 263.
16. Chuang, H.-J.; Chamlagain, B.; Koehler, M.; Perera, M. M.; Yan, J.; Mandrus, D.; Tománek, D. & Zhou, Z. Low-Resistance 2D/2D Ohmic Contacts: A Universal Approach to High-Performance WSe<sub>2</sub>, MoS<sub>2</sub>, and MoSe<sub>2</sub> Transistors. *Nano Letters.* **2016**, *16*, 1896.
17. Cong, C.; Shang, J.; Wu, X.; Cao, B.; Peimyoo, N.; Qiu, C.; Sun, L. & Yu, T. Synthesis and Optical Properties of Large-Area Single-Crystalline 2D Semiconductor WS<sub>2</sub> Monolayer from Chemical Vapor Deposition. *Advanced Optical Materials.* **2014**, *2*, 131.
18. Dai, S.; Yu, C.; Zhou, G.; Zhang, J.; Wang, G. & Hu, L. Concentration quenching in erbium-doped tellurite glasses. *Journal of Luminescence.* **2006**, *117*, 39.
19. David P Ziegler, A. L. J. Preparation and Properties of Luminescent Lanthanide Based Graphene Oxide. *Journal of Physical Chemistry & Biophysics.* **2013**, *03*.
20. Deák, P. Choosing Models for Solids. *Computer Simulation of Materials at Atomic Level,* **2000**, *9*.
21. Dejene, F. B. The effects of Eu ions and Eu:Dy ratio on the luminescence properties off blue-green BaAl<sub>x</sub>O<sub>y</sub>:Eu<sup>2+</sup>,Dy<sup>3+</sup> nano-phosphors. *Optical Materials.* **2013**, *35*, 1893.
22. Dolui, K.; Rungger, I.; Das Pemmaraju, C. & Sanvito, S. Possible doping strategies for MoS<sub>2</sub> monolayers: An ab initio study. *Physical Review B.* **2013**, *88*.

23. Dumcenco, D.; Ovchinnikov, D.; Marinov, K.; Lazić, P.; Gibertini, M.; Marzari, N.; Sanchez, O. L.; Kung, Y.-C.; Krasnozhon, D.; Chen, M.-W.; Bertolazzi, S.; Gillet, P.; Fontcuberta i Morral, A.; Radenovic, A. & Kis, A. Large-Area Epitaxial Monolayer MoS<sub>2</sub>. *ACS Nano*. **2015**, *9*, 4611.
24. Dutczak, D.; Jüstel, T.; Ronda, C. & Meijerink, A. Eu<sup>2+</sup> luminescence in strontium aluminates. *Physical Chemistry Chemical Physics*. **2015**, *17*, 15236.
25. Feng, N.; Mi, W.; Cheng, Y.; Guo, Z.; Schwingenschlögl, U. & Bai, H. First Principles Prediction of the Magnetic Properties of Fe-X6 (X = S, C, N, O, F) Doped Monolayer MoS<sub>2</sub>. *Scientific Reports*. **2014**, *4*, 3987.
26. Frauenheim, T., Seifert, G. , Elstner, M. , Hajnal, Z. , Jungnickel, G. , Porezag, D. , Suhai, S. and Scholz, R. A Self-Consistent Charge Density-Functional Based Tight-Binding Method for Predictive Materials Simulations in Physics, Chemistry and Biology. *Computer Simulation of Materials at Atomic Level*, **2005**, 41.
27. Ganguli, S.; Hazra, C.; Samanta, T. & Mahalingam, V. Photoluminescence and photocatalytic activity of monodispersed colloidal “ligand free Ln<sup>3+</sup>-doped PbMoO<sub>4</sub> nanocrystals”. *RSC Advances*. **2015**, *5*, 45611.
28. Gao, J.; Kim, Y. D.; Liang, L.; Idrobo, J. C.; Chow, P.; Tan, J.; Li, B.; Li, L.; Sumpter, B. G.; Lu, T.-M.; Meunier, V.; Hone, J. & Koratkar, N. Transition-Metal Substitution Doping in Synthetic Atomically Thin Semiconductors. *Advanced Materials*. **2016**, *28*, 9735.
29. Geim, A. K. & Grigorieva, I. V. Van der Waals heterostructures. *Nature*. **2013**, *499*, 419.
30. Goldstein, J. I.; Newbury, D. E.; Echlin, P.; Joy, D. C.; Lyman, C. E.; Lifshin, E.; Sawyer, L. & Michael, J. R. X-Ray Spectral Measurement: EDS and WDS.

- Scanning Electron Microscopy and X-ray Microanalysis: Third Edition, 2003, 297.
31. Guerfi, N.; Tan, T. A. N.; Veuillen, J. Y. & Lollman, D. B. Oxidation of thin ErSi<sub>1.7</sub> overlayers on Si(111). *Applied Surface Science*. **1992**, *56-58*, 501.
  32. Habib, M.; Muhammad, Z.; Khan, R.; Wu, C.; ur Rehman, Z.; Zhou, Y.; Liu, H. & Song, L. Ferromagnetism in CVT grown tungsten diselenide single crystals with nickel doping. *Nanotechnology*. **2018**, *29*, 115701.
  33. Han, G. H.; Kybert, N. J.; Naylor, C. H.; Lee, B. S.; Ping, J.; Park, J. H.; Kang, J.; Lee, S. Y.; Lee, Y. H.; Agarwal, R. & Johnson, A. T. Seeded growth of highly crystalline molybdenum disulphide monolayers at controlled locations. *Nat Commun*. **2015**, *6*, 6128.
  34. Han, S.; Deng, R.; Xie, X. & Liu, X. Enhancing luminescence in lanthanide-doped upconversion nanoparticles. *Angew Chem Int Ed Engl*. **2014**, *53*, 11702.
  35. Hu, Y.; Yao, Z. & Hu, J. 3-D FEM simulation of laser shock processing. *Surface and Coatings Technology*. **2006**, *201*, 1426.
  36. Hui, Y. Y.; Liu, X.; Jie, W.; Chan, N. Y.; Hao, J.; Hsu, Y.-T.; Li, L.-J.; Guo, W. & Lau, S. P. Exceptional Tunability of Band Energy in a Compressively Strained Trilayer MoS<sub>2</sub> Sheet. *ACS Nano*. **2013**, *7*, 7126.
  37. Ishii, K. High-rate low kinetic energy gas-flow-sputtering system. *Journal of Vacuum Science & Technology A*. **1989**, *7*, 256.
  38. Kabsch, W. Evaluation of single-crystal X-ray diffraction data from a position-sensitive detector. *Journal of Applied Crystallography*. **1988**, *21*, 916.
  39. Kido, J. & Okamoto, Y. Organo Lanthanide Metal Complexes for Electroluminescent Materials. *Chemical Reviews*. **2002**, *102*, 2357.

40. Kim, E.; Ko, C.; Kim, K.; Chen, Y.; Suh, J.; Ryu, S.-G.; Wu, K.; Meng, X.; Suslu, A.; Tongay, S.; Wu, J. & Grigoropoulos, C. P. Site Selective Doping of Ultrathin Metal Dichalcogenides by Laser-Assisted Reaction. *Advanced Materials*. **2016**, *28*, 341.
41. Komsa, H.-P. & Krasheninnikov, A. V. Native defects in bulk and monolayer MoS<sub>2</sub> from first principles. *Physical Review B*. **2015**, *91*.
42. Kresse, G. & Hafner, J. Ab initio molecular-dynamics simulation of the liquid-metal--amorphous-semiconductor transition in germanium. *Physical Review B*. **1994**, *49*, 14251.
43. Kresse, G. & Furthmüller, J. Efficient iterative schemes for ab initio total-energy calculations using a plane-wave basis set. *Physical Review B*. **1996**, *54*, 11169.
44. Lang, K. M.; Hite, D. A.; Simmonds, R. W.; McDermott, R.; Pappas, D. P. & Martinis, J. M. Conducting atomic force microscopy for nanoscale tunnel barrier characterization. *Review of Scientific Instruments*. **2004**, *75*, 2726.
45. Laskar, M. R.; Nath, D. N.; Ma, L.; Lee, E. W.; Lee, C. H.; Kent, T.; Yang, Z.; Mishra, R.; Roldan, M. A.; Idrobo, J.-C.; Pantelides, S. T.; Pennycook, S. J.; Myers, R. C.; Wu, Y. & Rajan, S. p-type doping of MoS<sub>2</sub> thin films using Nb. *Applied Physics Letters*. **2014**, *104*.
46. Lee, Y.-H.; Zhang, X.-Q.; Zhang, W.; Chang, M.-T.; Lin, C.-T.; Chang, K.-D.; Yu, Y.-C.; Wang, J. T.-W.; Chang, C.-S.; Li, L.-J. & Lin, T.-W. Synthesis of Large-Area MoS<sub>2</sub> Atomic Layers with Chemical Vapor Deposition. *Advanced Materials*. **2012**, *24*, 2320.
47. Lee, Y. H.; Zhang, X. Q.; Zhang, W.; Chang, M. T.; Lin, C. T.; Chang, K. D.; Yu, Y. C.; Wang, J. T.; Chang, C. S.; Li, L. J. & Lin, T. W. Synthesis of large-

- area MoS<sub>2</sub> atomic layers with chemical vapor deposition. *Adv Mater.* **2012**, *24*, 2320.
48. Lin, H.; Zhu, Q.; Shu, D.; Lin, D.; Xu, J.; Huang, X.; Shi, W.; Xi, X.; Wang, J. & Gao, L. Growth of environmentally stable transition metal selenide films. *Nat Mater.* **2019**.
49. Lin, X. & Ni, J. Charge and magnetic states of Mn-, Fe-, and Co-doped monolayer MoS<sub>2</sub>. *Journal of Applied Physics.* **2014**, *116*, 044311.
50. Lin, Y. C.; Dumcenco, D. O.; Komsa, H. P.; Niimi, Y.; Krasheninnikov, A. V.; Huang, Y. S. & Suenaga, K. Properties of individual dopant atoms in single-layer MoS<sub>2</sub>: atomic structure, migration, and enhanced reactivity. *Adv Mater.* **2014**, *26*, 2857.
51. Liu, K. K.; Zhang, W.; Lee, Y. H.; Lin, Y. C.; Chang, M. T.; Su, C. Y.; Chang, C. S.; Li, H.; Shi, Y.; Zhang, H.; Lai, C. S. & Li, L. J. Growth of large-area and highly crystalline MoS<sub>2</sub> thin layers on insulating substrates. *Nano Lett.* **2012**, *12*, 1538.
52. Liu, Y.; Ghosh, R.; Wu, D.; Ismach, A.; Ruoff, R. & Lai, K. Mesoscale imperfections in MoS<sub>2</sub> atomic layers grown by a vapor transport technique. *Nano Lett.* **2014**, *14*, 4682.
53. Lu, A.-Y.; Zhu, H.; Xiao, J.; Chuu, C.-P.; Han, Y.; Chiu, M.-H.; Cheng, C.-C.; Yang, C.-W.; Wei, K.-H.; Yang, Y.; Wang, Y.; Sokaras, D.; Nordlund, D.; Yang, P.; Muller, D. A.; Chou, M.-Y.; Zhang, X. & Li, L.-J. Janus monolayers of transition metal dichalcogenides. *Nature Nanotechnology.* **2017**, *12*, 744.
54. Lucas, J.; Lucas, P.; Le Mercier, T.; Rollat, A. & Davenport, W. Introduction to Rare Earth Luminescent Materials. *Rare Earths*, **2015**, 251.

55. Lucas, J.; Lucas, P.; Le Mercier, T.; Rollat, A. & Davenport, W. Rare Earth Electronic Structures and Trends in Properties. *Rare Earths*. **2015**, 123.
56. Luo, P.; Zhuge, F.; Zhang, Q.; Chen, Y.; Lv, L.; Huang, Y.; Li, H. & Zhai, T. Doping engineering and functionalization of two-dimensional metal chalcogenides. *Nanoscale Horizons*. **2018**.
57. Luo, Z.; Ouyang, Y.; Zhang, H.; Xiao, M.; Ge, J.; Jiang, Z.; Wang, J.; Tang, D.; Cao, X.; Liu, C. & Xing, W. Chemically activating MoS<sub>2</sub> via spontaneous atomic palladium interfacial doping towards efficient hydrogen evolution. *Nature Communications*. **2018**, 9, 2120.
58. Majid, A.; Imtiaz, A. & Yoshiya, M. A density functional theory study of electronic and magnetic properties of rare earth doped monolayered molybdenum disulphide. *Journal of Applied Physics*. **2016**, 120, 142124.
59. Majid, A.; Imtiaz, A. & Yoshiya, M. A density functional theory study of electronic and magnetic properties of rare earth doped monolayered molybdenum disulphide. *Journal of Applied Physics*. **2016**, 120.
60. McCreery, R. L. Collection and Detection of Raman Scattering. *Raman Spectroscopy for Chemical Analysis*, **2005**, 35.
61. Miniscalco, W. J. Erbium-doped glasses for fiber amplifiers at 1500 nm. *Journal of Lightwave Technology*. **1991**, 9, 234.
62. Molner, S. P. The Art of Molecular Dynamics Simulation (Rapaport, D. C.). *Journal of Chemical Education*. **1999**, 76, 171.
63. Mounet, N.; Gibertini, M.; Schwaller, P.; Campi, D.; Merkys, A.; Marrazzo, A.; Sohier, T.; Castelli, I. E.; Cepellotti, A.; Pizzi, G. & Marzari, N. Two-dimensional materials from high-throughput computational exfoliation of experimentally known compounds. *Nat Nanotechnol*. **2018**, 13, 246.

64. Mouri, S.; Miyauchi, Y. & Matsuda, K. Tunable photoluminescence of monolayer MoS<sub>2</sub> via chemical doping. *Nano Lett.* **2013**, *13*, 5944.
65. Niesłony, P.; Grzesik, W.; Chudy, R. & Habrat, W. Meshing strategies in FEM simulation of the machining process. *Archives of Civil and Mechanical Engineering.* **2015**, *15*, 62.
66. Odegard, G. M.; Gates, T. S.; Nicholson, L. M. & Wise, K. E. Equivalent-continuum modeling of nano-structured materials. *Composites Science and Technology.* **2002**, *62*, 1869.
67. Onofrio, N.; Guzman, D. & Strachan, A. Novel doping alternatives for single-layer transition metal dichalcogenides. *Journal of Applied Physics.* **2017**, *122*.
68. Ouma, C. N. M.; Singh, S.; Obodo, K. O.; Amolo, G. O. & Romero, A. H. Controlling the magnetic and optical responses of a MoS<sub>2</sub> monolayer by lanthanide substitutional doping: a first-principles study. *Phys Chem Chem Phys.* **2017**, *19*, 25555.
69. Özden, A.; Ay, F.; Sevik, C. & Perkgöz, N. K. CVD growth of monolayer MoS<sub>2</sub>: Role of growth zone configuration and precursors ratio. *Japanese Journal of Applied Physics.* **2017**, *56*.
70. Pan, Z.; Morgan, S. H.; Ueda, A.; Aga, R.; Steigerwald, A.; Hmelo, A. B. & Mu, R. Er-doped ZnO films grown by pulsed e-beam deposition. *Journal of Physics: Condensed Matter.* **2007**, *19*.
71. Parr, R. G., presented at the Horizons of Quantum Chemistry, Dordrecht, 1980 (unpublished).
72. Peijzel, P. S.; Meijerink, A.; Wegh, R. T.; Reid, M. F. & Burdick, G. W. A complete energy level diagram for all trivalent lanthanide ions. *Journal of Solid State Chemistry.* **2005**, *178*, 448.

73. Pham, V. P. & Yeom, G. Y. Recent Advances in Doping of Molybdenum Disulfide: Industrial Applications and Future Prospects. *Adv Mater.* **2016**, *28*, 9024.
74. Pokhrel, M.; Kumar, G. A.; Ma, C. G.; Brik, M. G.; Langloss, B. W.; Stanton, I. N.; Therien, M. J.; Sardar, D. K. & Mao, Y. Electronic and optical properties of Er-doped Y<sub>2</sub>O<sub>2</sub>S phosphors. *Journal of Materials Chemistry C.* **2015**, *3*, 11486.
75. Polman, A. & van Veggel, F. C. J. M. Broadband sensitizers for erbium-doped planar optical amplifiers: review. *J. Opt. Soc. Am. B.* **2004**, *21*, 871.
76. Qin, X.; Liu, X.; Huang, W.; Bettinelli, M. & Liu, X. Lanthanide-Activated Phosphors Based on 4f-5d Optical Transitions: Theoretical and Experimental Aspects. *Chem Rev.* **2017**, *117*, 4488.
77. Rastogi, P.; Kumar, S.; Bhowmick, S.; Agarwal, A. & Chauhan, Y. S. Doping Strategies for Monolayer MoS<sub>2</sub> via Surface Adsorption: A Systematic Study. *The Journal of Physical Chemistry C.* **2014**, *118*, 30309.
78. Reddy, A. A.; Babu, S. S.; Pradeesh, K.; Otton, C. J. & Vijaya Prakash, G. Optical properties of highly Er<sup>3+</sup>-doped sodium–aluminium–phosphate glasses for broadband 1.5μm emission. *Journal of Alloys and Compounds.* **2011**, *509*, 4047.
79. Ross, J. S.; Klement, P.; Jones, A. M.; Ghimire, N. J.; Yan, J.; Mandrus, D. G.; Taniguchi, T.; Watanabe, K.; Kitamura, K.; Yao, W.; Cobden, D. H. & Xu, X. Electrically tunable excitonic light-emitting diodes based on monolayer WSe<sub>2</sub> p-n junctions. *Nat Nanotechnol.* **2014**, *9*, 268.
80. Sahu, I. P.; Bisen, D. P.; Tamrakar, R. K.; Murthy, K. V. R. & Mohapatra, M. Luminescence studies on the europium doped strontium metasilicate phosphor

- prepared by solid state reaction method. *Journal of Science: Advanced Materials and Devices*. **2017**, *2*, 59.
81. Shi, Y.; Li, H. & Li, L. J. Recent advances in controlled synthesis of two-dimensional transition metal dichalcogenides via vapour deposition techniques. *Chem Soc Rev*. **2015**, *44*, 2744.
82. Shinde, K. N.; Dhoble, S. J.; Swart, H. C. & Park, K. Basic Mechanisms of Photoluminescence. *Phosphate Phosphors for Solid-State Lighting*, **2012**, *41*.
83. Shu, H.; Luo, P.; Liang, P.; Cao, D. & Chen, X. Layer-Dependent Dopant Stability and Magnetic Exchange Coupling of Iron-Doped MoS<sub>2</sub> Nanosheets. *ACS Applied Materials & Interfaces*. **2015**, *7*, 7534.
84. Šimůnek, A. & Vackář, J. Hardness of Covalent and Ionic Crystals: First-Principle Calculations. *Physical Review Letters*. **2006**, *96*, 085501.
85. Splendiani, A.; Sun, L.; Zhang, Y.; Li, T.; Kim, J.; Chim, C. Y.; Galli, G. & Wang, F. Emerging photoluminescence in monolayer MoS<sub>2</sub>. *Nano Lett*. **2010**, *10*, 1271.
86. Suh, J.; Park, T.-E.; Lin, D.-Y.; Fu, D.; Park, J.; Jung, H. J.; Chen, Y.; Ko, C.; Jang, C.; Sun, Y.; Sinclair, R.; Chang, J.; Tongay, S. & Wu, J. Doping against the Native Propensity of MoS<sub>2</sub>: Degenerate Hole Doping by Cation Substitution. *Nano Letters*. **2014**, *14*, 6976.
87. Suh, J.; Tan, T. L.; Zhao, W.; Park, J.; Lin, D. Y.; Park, T. E.; Kim, J.; Jin, C.; Saigal, N.; Ghosh, S.; Wong, Z. M.; Chen, Y.; Wang, F.; Walukiewicz, W.; Eda, G. & Wu, J. Reconfiguring crystal and electronic structures of MoS<sub>2</sub> by substitutional doping. *Nat Commun*. **2018**, *9*, 199.
88. Tan, H.; Hu, W.; Wang, C.; Ma, C.; Duan, H.; Yan, W.; Cai, L.; Guo, P.; Sun, Z.; Liu, Q.; Zheng, X.; Hu, F. & Wei, S. Intrinsic Ferromagnetism in Mn-

- Substituted MoS<sub>2</sub> Nanosheets Achieved by Supercritical Hydrothermal Reaction. *Small.* **2017**, *13*, 1701389.
89. Tedstone, A. A.; Lewis, D. J. & O'Brien, P. Synthesis, Properties, and Applications of Transition Metal-Doped Layered Transition Metal Dichalcogenides. *Chemistry of Materials.* **2016**, *28*, 1965.
90. Thangaraja, A.; Shinde, S. M.; Kalita, G. & Tanemura, M. An effective approach to synthesize monolayer tungsten disulphide crystals using tungsten halide precursor. *Applied Physics Letters.* **2016**, *108*.
91. Tian, Y.; Xu, R.; Hu, L. & Zhang, J. Effect of chloride ion introduction on structural and 1.5 μm emission properties in Er<sup>3+</sup>-doped fluorophosphate glass. *J. Opt. Soc. Am. B.* **2011**, *28*, 1638.
92. Tonndorf, P.; Schmidt, R.; Böttger, P.; Zhang, X.; Börner, J.; Liebig, A.; Albrecht, M.; Kloc, C.; Gordan, O.; Zahn, D. R. T.; Michaelis de Vasconcellos, S. & Bratschitsch, R. Photoluminescence emission and Raman response of monolayer MoS<sub>2</sub>, MoSe<sub>2</sub>, and WSe<sub>2</sub>. *Opt. Express.* **2013**, *21*, 4908.
93. van der Zande, A. M.; Huang, P. Y.; Chenet, D. A.; Berkelbach, T. C.; You, Y.; Lee, G.-H.; Heinz, T. F.; Reichman, D. R.; Muller, D. A. & Hone, J. C. Grains and grain boundaries in highly crystalline monolayer molybdenum disulphide. *Nature Materials.* **2013**, *12*, 554.
94. Vandenabeele, P. Theoretical Aspects. *Practical Raman Spectroscopy – An Introduction*, **2013**, 1.
95. Wang, H.; Tsai, C.; Kong, D.; Chan, K.; Abild-Pedersen, F.; Nørskov, J. K. & Cui, Y. Transition-metal doped edge sites in vertically aligned MoS<sub>2</sub> catalysts for enhanced hydrogen evolution. *Nano Research.* **2015**, *8*, 566.

96. Wang, S.; Rong, Y.; Fan, Y.; Pachios, M.; Bhaskaran, H.; He, K. & Warner, J. H. Shape Evolution of Monolayer MoS<sub>2</sub> Crystals Grown by Chemical Vapor Deposition. *Chemistry of Materials*. **2014**, *26*, 6371.
97. Wang, S. Y.; Ko, T. S.; Huang, C. C.; Lin, D. Y. & Huang, Y. S. Optical and electrical properties of MoS<sub>2</sub> and Fe-doped MoS<sub>2</sub>. *Japanese Journal of Applied Physics*. **2014**, *53*.
98. Wang, X.; Feng, H.; Wu, Y. & Jiao, L. Controlled synthesis of highly crystalline MoS<sub>2</sub> flakes by chemical vapor deposition. *J Am Chem Soc*. **2013**, *135*, 5304.
99. Wang, X. L.; Gong, Y. J.; Shi, G.; Chow, W. L.; Keyshar, K.; Ye, G. L.; Vajtai, R.; Lou, J.; Liu, Z.; Ringe, E.; Tay, B. K. & Ajayan, P. M. Chemical Vapor Deposition Growth of Crystalline Mono layer MoSe<sub>2</sub>. *Acs Nano*. **2014**, *8*, 5125.
100. Weiss, N. O.; Zhou, H.; Liao, L.; Liu, Y.; Jiang, S.; Huang, Y. & Duan, X. Graphene: An Emerging Electronic Material. *Advanced Materials*. **2012**, *24*, 5782.
101. Withers, F.; Del Pozo-Zamudio, O.; Mishchenko, A.; Rooney, A. P.; Gholinia, A.; Watanabe, K.; Taniguchi, T.; Haigh, S. J.; Geim, A. K.; Tartakovskii, A. I. & Novoselov, K. S. Light-emitting diodes by band-structure engineering in van der Waals heterostructures. *Nat Mater*. **2015**, *14*, 301.
102. Wu, S. & Butt, H. J. Near-Infrared-Sensitive Materials Based on Upconverting Nanoparticles. *Adv Mater*. **2016**, *28*, 1208.
103. Xu, S.; Gao, X.; Hu, M.; Wang, D.; Jiang, D.; Sun, J.; Zhou, F.; Weng, L. & Liu, W. Microstructure Evolution and Enhanced Tribological Properties of Cu-Doped WS<sub>2</sub> Films. *Tribology Letters*. **2014**, *55*, 1.

104. Yadgarov, L.; Stroppa, D. G.; Rosentsveig, R.; Ron, R.; Enyashin, A. N.; Houben, L. & Tenne, R. Investigation of Rhenium-Doped MoS<sub>2</sub> Nanoparticles with Fullerene-Like Structure. *Zeitschrift für anorganische und allgemeine Chemie.* **2012**, *638*, 2610.
105. Yadgarov, L.; Rosentsveig, R.; Leitus, G.; Albu-Yaron, A.; Moshkovich, A.; Perfiliev, V.; Vasic, R.; Frenkel, A. I.; Enyashin, A. N.; Seifert, G.; Rapoport, L. & Tenne, R. Controlled doping of MS<sub>2</sub> (M=W, Mo) nanotubes and fullerene-like nanoparticles. *Angew Chem Int Ed Engl.* **2012**, *51*, 1148.
106. Yang, Y.; Pu, H.; Di, J.; Zang, Y.; Zhang, S. & Chen, C. Synthesis and characterization of monolayer Er-doped MoS<sub>2</sub> films by chemical vapor deposition. *Scripta Materialia.* **2018**, *152*, 64.
107. Yu, Y.; Li, C.; Liu, Y.; Su, L.; Zhang, Y. & Cao, L. Controlled scalable synthesis of uniform, high-quality monolayer and few-layer MoS<sub>2</sub> films. *Sci Rep.* **2013**, *3*, 1866.
108. Yue, Q.; Chang, S.; Qin, S. & Li, J. Functionalization of monolayer MoS<sub>2</sub> by substitutional doping: A first-principles study. *Physics Letters A.* **2013**, *377*, 1362.
109. Zhan, Y.; Liu, Z.; Najmaei, S.; Ajayan, P. M. & Lou, J. Large-area vapor-phase growth and characterization of MoS<sub>2</sub> atomic layers on a SiO<sub>2</sub> substrate. *Small.* **2012**, *8*, 966.
110. Zhang, J.; He, H. & Pan, B. Fe/Co doped molybdenum diselenide: a promising two-dimensional intermediate-band photovoltaic material. *Nanotechnology.* **2015**, *26*, 195401.
111. Zhang, K.; Bersch, B. M.; Joshi, J.; Addou, R.; Cormier, C. R.; Zhang, C.; Xu, K.; Briggs, N. C.; Wang, K.; Subramanian, S.; Cho, K.; Fullerton-Shirey, S.;

- Wallace, R. M.; Vora, P. M. & Robinson, J. A. Tuning the Electronic and Photonic Properties of Monolayer MoS<sub>2</sub> via In Situ Rhenium Substitutional Doping. *Advanced Functional Materials.* **2018**, *28*, 1706950.
112. Zhang, K.; Feng, S.; Wang, J.; Azcatl, A.; Lu, N.; Addou, R.; Wang, N.; Zhou, C.; Lerach, J.; Bojan, V.; Kim, M. J.; Chen, L. Q.; Wallace, R. M.; Terrones, M.; Zhu, J. & Robinson, J. A. Manganese Doping of Monolayer MoS<sub>2</sub>: The Substrate Is Critical. *Nano Lett.* **2015**, *15*, 6586.
113. Zhang, X.; Tang, H.; Xue, M. & Li, C. Facile synthesis and characterization of ultrathin MoS<sub>2</sub> nanosheets. *Materials Letters.* **2014**, *130*, 83.
114. Zhang, X. J.; Wang, X. C. & Mi, W. B. Density functional theory prediction on magnetism in Gd-doped monolayer MoS<sub>2</sub>. *Solid State Communications.* **2015**, *212*, 35.
115. Zhou, B.; Tao, L.; Chai, Y.; Lau, S. P.; Zhang, Q. & Tsang, Y. H. Constructing Interfacial Energy Transfer for Photon Up- and Down-Conversion from Lanthanides in a Core-Shell Nanostructure. *Angew Chem Int Ed Engl.* **2016**, *55*, 12356.
116. Zhou, J.; Lin, J.; Huang, X.; Zhou, Y.; Chen, Y.; Xia, J.; Wang, H.; Xie, Y.; Yu, H.; Lei, J.; Wu, D.; Liu, F.; Fu, Q.; Zeng, Q.; Hsu, C. H.; Yang, C.; Lu, L.; Yu, T.; Shen, Z.; Lin, H.; Yakobson, B. I.; Liu, Q.; Suenaga, K.; Liu, G. & Liu, Z. A library of atomically thin metal chalcogenides. *Nature.* **2018**, *556*, 355.